NTNU

Norwegian University of
Science and Technology

Feasibility of Using Phototherapy with Sunlight for Treatment of Neonatal Jaundice in Low-Income Countries

Sigrid Rønneberg

Master of Science in Physics and Mathematics
Submission date: June 2016
Supervisor: Pål Erik Goa, IFY
Co-supervisor: Lise Lyngsnes Randeberg, IET
Lill Tove Norvang Nilsen, Statens Strålevern
Ellen Bruzell, Nordisk Institutt for Odontologiske Materialer

Norwegian University of Science and Technology
Department of Physics

”Sunlight is the best disinfectant.”

- William O. Douglas

Main supervisors:
Associate Professor Dr. Pål Erik Goa, Department of Physics, NTNU
Professor Dr. Lise Lyngsnes Randeberg, Department of Electronics and Telecommunications, NTNU
Dr. Lill Tove Norvang Nilsen, Norwegian Radiation Protection Authority

Co-supervisors:
Dr. Ellen Bruzell, Nordic Institute of Dental Materials
Dr. Terje Christensen, Norwegian Radiation Protection Authority
Bjørn Johnsen, Norwegian Radiation Protection Authority

Preface

This Master's thesis was realised at the Department of Physics and the Department of Electronics and Telecommunication at the Norwegian University of Science and Technology (NTNU) in cooperation with the Norwegian Radiation Protection Authority (NRPA). The thesis was conducted during the spring semester of 2016.

I want to thank my whole team of supervisors: Lise Lyngsnes Randeberg, for helping me to set ambitious goals and to seeing them through; Lill Tove Norvang Nilsen for answering emails in a flash, organizing the resources at NRPA and giving me a place to sit in Oslo; Ellen Bruzell and Terje Christensen for helping me with the biological aspects and for invaluable help with the measurement protocols at St. Olavs Hospital as well as proof-reading; Bjørn Johnsen for a large amount of help with the atmospheric simulations and for helping with the calibration of the radiometer; and, last but not least, Pål Erik Goa for help with the physics and the formalities of the thesis.

This thesis is based on previous work and effort from several instances. The simulation of newborn skin was performed with models developed by Lise Lyngsnes Randeberg and Asgeir Bjørgan at NTNU, and run by Asgeir Bjørgan. The experimental irradiance measurements were performed with equipment from both NTNU and NRPA, and the irradiance results were converted with help from NRPA and especially Bjørn Johnsen. He was also instrumental in the calibration of the radiometer, and the methods for both converting the irradiance measurements to bilirubin weighted irradiance from the blue weighted probe (section 3.2.1) and converting the spectrum to units of irradiance (section 3.1.6). The *libRadtran* software package was installed with help from Dag Robøle at the IT department of NRPA. All the atmospheric simulations are directly based on programs by Bjørn Johnsen, and he gave me both the location of the overpass data, the most important information found there and examples on how to extract the information. The measurement data from Østerås used to assess and validate the results of the atmospheric simulations (section 3.2.1) were also prepared by Bjørn Johnsen, and given to me in a very convenient .mat-file. Thank you!

I would also like to thank fellow master student Adrian Sjøholt for cooperation on the measurements at St. Olavs Hospital, paediatrician Anders Aune for helping us set up the meetings at St. Olavs Hospital and for answering questions about the medical aspect of phototherapy treatment, the NRPA for lending us the radiometer used to measure the irradiance, Beate Herfjord at the neonatal ward at St. Olavs Hospital for graciously answering our questions on short notice, and Håvard Sagvik Børseth at the Medical Technical Department at St. Olavs Hospital for information about the phototherapy units in use at St. Olavs Hospital. I also want to send a last thank you to Asgeir Bjørgan, for running the simulations of radiative transfer in skin.

The greatest reward during this work has been the surprising results. When I first started working on this thesis, I assumed that the necessary solar exposure time would be measured in minutes, and certainly less than an hour. The fact that the exposure time ended up being several days astonished me, and is to me evidence that intuition gets us nowhere. It seems fitting to end my Master's degree in Applied Physics with this lesson.

Trondheim, 10.06.2016

Sigrid Rønneberg

Abstract

This thesis aimed to investigate the feasibility of using sunlight exposure as treatment for neonatal jaundice in low-income countries. The investigation answered four questions:

1. Is it feasible to treat infants with neonatal jaundice with sunlight?
2. Are the existing treatment guidelines sufficient for all skin types?
3. Is sunlight treatment adequately efficient compared to conventional treatment?
4. Is sunlight treatment of neonatal jaundice feasible in the investigated locations?

More than $114\,000$ infants die annually due to untreated neonatal jaundice worldwide, and a large percentage of these deaths occur in sub-Saharan Africa or South-East Asia. These areas are locations with abundant sunlight.

The methods used in this thesis included irradiance measurements of conventional phototherapy equipment and an assessment of treatment conditions at a representative hospital in Norway. In addition, atmospheric simulations with *libRadtran* were performed with satellite overpass data from 2015 for Dar es Salaam, Kathmandu and Østerås, with the latter as a reference location. Further, simulations of fluence in skin of melanin pigmentation corresponding to skin types II, IV, V and VI were performed by using a Monte Carlo method for multi-layered tissue. Skin type II was chosen for reference, and the higher skin types were included due to the relevance in sub-Saharan Africa and South-East Asia.

The average bilirubin weighted total irradiance of the conventional phototherapy units at St. Olavs Hospital was $10.3\,\mathrm{W/m^2}$, which was just within the scientific recommendations of at least $10\,\mathrm{W/m^2}$ of irradiance for maximal effect of the phototherapy. The solar irradiance was of the same magnitude for all the chosen locations, and the maximal value at noon ranged with the seasons and atmospheric conditions from $0.8 - 7.3\,\mathrm{W/m^2}$ for Dar es Salaam, $0.7 - 6.7\,\mathrm{W/m^2}$ for Kathmandu and $0.1 - 5.4\,\mathrm{W/m^2}$ for Østerås. The simulated fluence at a skin depth of $295\,\mu\mathrm{m}$ was reduced to 43% of the fluence for skin type II in skin type VI, which showed a great impact of pigmentation on the fluence in the skin.

The bilirubin weighted radiant exposure achieved through conventional phototherapy in Norway was $7.42 \cdot 10^5\,\mathrm{J/m^2}$. To achieve the same effective radiant exposure through exposure to sunlight, the exposure times for average summer days with sunlight exposure from sunrise to sunset was 4.3 days in Dar es Salaam, 4.2 days for Kathmandu and 5.4 days for Østerås. In winter, these exposure times increased with 35%, 88% and 234% for the three locations, respectively. For skin type VI, the summer exposure time became 10.2 days, 10.0 days and 13.0 days, respectively. The amount of adverse effects from erythema was severe for each day of sunlight exposure, both in painful sunburn and increased risk of skin cancer. All calculations were only indicative, as they were based on certain assumptions and uncertainties, which include uncertainties in satellite overpass data, uncertainties in both skin types and infant skin, and assumptions on the scaling of required exposure time for different skin types.

The thesis concluded that it is feasible to treat neonatal jaundice with sunlight, with reservations. These reservations are connected to the calculated exposure times, which might give substantial adverse effects of sunburn. None of the existing treatment guidelines are sufficient concerning skin types of different pigmentation. If sunlight treatment is used optimally and the guidelines for conventional phototherapy are optimised, the sunlight treatment might be as efficient as conventional treatment in treating neonatal jaundice. This relatively new treatment option might be life-saving for infants in low-income countries.

Sammendrag

Denne oppgaven undersøkte muligheten for å benytte sollys til lysbehandling av nyfødte med gulsott i lavinntektsland. Undersøkelsen svarte på fire spørsmål:

1. Er det gjennomførbart å behandle nyfødte med gulsott med sollys?
2. Er de eksisterende retningslinjene for behandling gode nok for alle hudtyper?
3. Er behandling med sollys tilstrekkelig effektivt sammenlignet med konvensjonell lysbehandling?
4. Er behandling med sollys gjennomførbart i de undersøkte geografiske stedene?

Mer enn $114\,000$ nyfødte dør hvert år på grunn av ubehandlet gulsott, og en stor andel av disse dødsfallene forekommer sør for Sahara i Afrika og i sør-øst Asia. Dette er områder der det finnes rikelig med sollys.

Metodene som ble brukt i denne oppgaven inkluderte eksperimentelle målinger av irradians ved konvensjonell lysbehandling og undersøker av behandlingsforhold ved et representativt sykehus i Norge. I tillegg ble det brukt atmosfæriske simuleringer med *libRadtran* og meteorologiske satellittdata fra 2015 for Dar es Salaam, Kathmandu og Østerås, med sistnevnte som referanse. Videre ble simuleringer av fluens i hud med pigmentering tilsvarende hudtype II, IV, V og VI gjennomført ved å bruke en Monte Carlo modell for flerlags biologisk media. Hudtype II ble brukt som referanse, og de mørkere hudtypene ble inkludert på grunn av relevans i Afrika sør for Sahara og i sør-øst Asia.

Gjennomsnittlig bilirubin vektet total irradians ved lysbehandling på St. Olavs sykehus var $10.3\,\mathrm{W/m^2}$, som lå akkurat innenfor de vitenskaplige anbefalingene om en irradians på minst $10\,\mathrm{W/m^2}$ for maksimal effekt av lysbehandlingen. Irradiansen fra sola er av samme størrelsesorden for alle de valgte stedene, og den maksimale verdien midt på dagen varierte med årstid og atmosfæriske forhold mellom $0.8 - 7.3\,\mathrm{W/m^2}$ i Dar es Salaam, $0.7 - 6.7\,\mathrm{W/m^2}$ i Kathmandu og $0.1 - 5.4\,\mathrm{W/m^2}$ ved Østerås. Den simulerte fluensen ved en huddybde på $295\,\mu\mathrm{m}$ ble redusert til 43% av fluensen til hudtype II for hudtype VI, som viser en stor effekt av pigmentering på fluens i huden.

Den bilirubin-vektede strålingsdosen oppnådd ved konvensjonell lysbehanding i Norge var $7.42 \cdot 10^5\,\mathrm{J/m^2}$. For å oppnå samme strålingsdose gjennom eksponering fra sollys måtte eksponeringstiden ved gjennomsnittlige sommerdager med eksponering fra soloppgang til solnedgang vært 4.3 dager i Dar es Salaam, 4.2 dager i Kathmandu, og 5.4 dager ved Østerås. Om vinteren økte disse tidene med henholdsvis 35%, 88% og 234% for de ulike stedene. For hudtype VI måtte eksponeringen sommerstid vært henholdsvis 10.2 dager, 10.0 dager og 13.0 dager for de tre stedene. Skadelige effekter fra erytem var alvorlige for hver dag med soleksponering, både med smertefull solbrenthet og en økt risiko for hudkreft. Alle utregninger var kun veiledende, da de ble basert på flere antagelser og usikkerheter som blant annet usikkerheter i satellittdata, usikkerheter i både hudtype og hud hos nyfødte, og antagelser om skalering av nødvendig eksoneringstid for ulike hudtyper.

Oppgaven konkluderer med at det er gjennomførbart å behandle nyfødte med gulsott med sollys, med reservasjoner. Disse reservasjonene er knyttet til de beregnede eksponeringstidene, som kan gi betydelige skader i form av solbrenthet. Ingen av de eksisterende retningslinjene for behandling er tilstrekkelige for ulike hudtyper og pigmentering. Dersom behandling med sollys brukes optimalt og retningslinjene for konvensjonell lysbehandling blir optimerte, vil eksponering av sollys kunne være tilstrekkelig effektivt sammenlignet med konvensjonell behandling for å behandle nyfødte med gulsott. Dette relativt nye alternativet for behandling vil kunne virke livreddende for nyfødte i lavinntektsland.

Contents

Chapter 1

Introduction

Neonatal jaundice, or hyperbilirubinemia, is a relatively common condition that occurs in about two out of three newborns [121]. The condition is characterized by a yellow tint to the skin, eyes and inside of mouth. Neonatal jaundice is often transient, but may also cause death and damage to the nervous system if untreated [109]. Over $114\,000$ infants die annually, and $65\,000$ infants grow up every year with permanent brain damage due to untreated neonatal jaundice worldwide [13]. A large percentage of these deaths and injuries occur in South-East Asia and in sub-Saharan Africa, in areas which include several low-income countries.

The most frequently used treatment of neonatal jaundice is with irradiation of visible light. This form of phototherapy was first discovered in 1954 by Cremer et al [26] in England. Conventional phototherapy uses electricity-driven units which irradiate the jaundiced infant with visible light, often blue, over as large skin area as possible. However, *in vitro* studies have shown that sunlight might be a possible alternative to traditional phototherapy treatment [109]. As the geographical areas where the mortality due to neonatal jaundice is high are close to the equator, and therefore characterized by abundant sunlight, treatment by solar exposure may be feasible. A safe and sufficiently effective treatment plan for neonatal jaundice by using sunlight alone may save a large percentage of the infants impacted by the lack of treatment of neonatal jaundice in low-income countries.

A number of research projects have been performed on the subject of infant exposure to sunlight, and to assess whether controlled sunlight exposure may be an alternative to phototherapy as a treatment of neonatal jaundice. However, the optimised irradiance, exposure time and relative efficacy as a function of peak wavelength for conventional phototherapy are still disagreed on. This lack of agreement creates difficulties in comparing a sunlight treatment plan to the conventional treatment of neonatal jaundice. In 2008, Devine et al called for clinical evidence-based guidelines for treatment of neonatal jaundice [27]. However, the impact of different skin types and skin pigmentations of infants on the effect of phototherapy treatment is not mentioned in any investigated treatment guidelines.

When it comes to the exposure of infants to sunlight in connection to neonatal jaundice, there are several recommendations found in the literature. Harrison et al states both that

> "Given that the repercussions of excessive sun exposure in early childhood and the effect that sunning a child for jaundice has on the beliefs and presumable behaviour of postparturient women, it is inappropriate to use sunlight in sunny climates to treat neonatal jaundice" [44]

and that

> "It is inappropriate to recommend exposing infants to sunlight to treat neonatal jaundice, except perhaps in exceptional circumstances (e.g. areas with no access to conventional phototherapy units)" [43]

This last quote applies to the conditions of this thesis, which aims to help infants where the conventional treatment is unavailable. The two quotes, from largely the same authors 3 years apart in publication time, illustrate the amount of uncertainty in this area of medical guidelines. Both of these quotes are from a series of four studies [27, 43–45] originating from Townsend, Australia, which investigated the practice of Caucasian mothers exposing their infants to sunlight for infants.

Another series of studies was conducted in Nigeria and researched the incidence and treatment of neonatal jaundice parallel to a course of study using filtered-sunlight phototherapy. The first line of study found, among other results, that home care, traditions and late recognition of the condition were important delay-mechanisms for seeking professional help to cure neonatal jaundice [93]. It was also found that more than half of the investigated mothers who claimed awareness of neonatal jaundice stated sun-exposure as preferred treatment of their jaundiced infants [29, 31].

The second line of study in Nigeria dealt with the use of window-tinting films for filtration of ultraviolet (UV) radiation from the sun and accessing the filtered sunlight for phototherapy of infants. This range of studies included a classification of several window-tinting films for UV-filtration [135], an evaluation of the safety and efficacy of the exposure of infants to the filtered sunlight [115], a randomized trial where the filtered sunlight phototherapy was compared to conventional phototherapy [113, 114], and a study of the maternal satisfaction when their children were treated with the filtered sunlight approach [91]. This study of filtered sunlight phototherapy will be discussed more thoroughly later in the thesis.

This thesis continues the work from a specialization project with the title *Phototherapy with Sunlight for Treatment of Neonatal Jaundice in Low-Income Countries* [107]. This project aimed to investigate theoretically by atmospheric simulations whether phototherapeutic exposure to sunlight could be included in the treatment methods of neonatal jaundice in low-income countries. The aim was achieved by simulating theoretical atmospheric conditions with *libRadtran* for separately varying different atmospheric parameters. Results of the project included the changing atmospheric solar irradiation as a function of the atmospheric variables when negating the effects of coupling between them. The actual conditions of investigated locations were also negated. Another limitation of the specialization project was that only the atmospheric conditions and irradiation were investigated, and the conventional phototherapy treatment and the effects of the irradiation on the skin was not included. The project concluded with eight general recommendations for the treatment of neonatal jaundice with sunlight. For these recommendations, the reader is referred to the specialization project itself.

1.1 Scope and aim of thesis

The aim of this thesis is to investigate the feasibility of using sunlight exposure as treatment for neonatal jaundice in low-income countries. The investigation aims to answer the following four questions:

1. Is it feasible to treat infants with neonatal jaundice with sunlight?
2. Are the existing treatment guidelines sufficient for all skin types?
3. Is sunlight treatment adequately efficient compared to conventional treatment?
4. Is sunlight treatment of neonatal jaundice feasible in the investigated locations?

Countries are classified as low-income or high-income according to the Human Development Index developed by the United Nations [56].

The investigation is performed by first assessing the current treatment of phototherapy in high-income countries as basis for comparing with sunlight therapy. This assessment includes investigating different guidelines for treatment of neonatal jaundice, and determining the treatment conditions as performed at St. Olavs Hospital in Trondheim, Norway. The treatment in Trondheim is defined as the optimal treatment in this thesis, and is determined by irradiance measurements on typical phototherapy units. The conventional phototherapy performed in Trondheim is the reference for comparisons of sunlight treatment. It is also discussed whether this treatment is optimal.

To assess the possibility of using sunlight in different parts of the world, a study of surface solar irradiation with three chosen geographical locations is performed. The locations are Dar es Salaam in Tanzania, Kathmandu in Nepal, and Østerås, close to Oslo in Norway. The two first locations have been chosen because they are situated in areas relevant for the potential use of phototherapeutic sunlight, while Østerås has been included for reasons of comparison and calibration. For each of the locations, the solar irradiance throughout 2015 is simulated for local and variable atmospheric conditions. This amount of solar irradiance is compared to the Norwegian treatment of neonatal jaundice.

The effect of different skin types and skin pigmentation is investigated by simulating the propagation of radiation in infant skin of gestation maturity 40 weeks with differing optical parameters. The optical parameters associated with each skin type, including the pigmentation, are defined specifically for this thesis.

By investigating the differences of the conventional phototherapy treatment and the surface solar irradiance, the feasibility and necessary exposure time of sunlight phototherapy is determined. The calculation is expanded by including the differences of skin types and the simulated differences in fluence.

To determine the scope of the thesis, it is important to determine the wavelength ranges of the electromagnetic spectrum relevant for sunlight. The solar irradiation contains all wavelengths in the electromagnetic spectrum. This thesis focuses on the radiation in the visible and UV wavelength ranges, which are defined in table 1.1. Infrared (IR) radiation is also defined in this table.

Throughout the thesis, different skin types are compared with respect to solar exposure and the effect. These skin types are defined in section 2.6. Ordinary skin types only account for skin response of previously unexposed skin. However, the skin types as defined in this thesis include optical parameters such as pigmentation. This simplification makes comparisons easier, although it is not necessarily correct according to other publications or reality.

Most comparisons in this thesis are given in SI units of W/m^2 and J/m^2. However, for the irradiance measurements of the conventional phototherapy units, the irradiances are given in mW/cm^2. This change of units is due to the biological standard, which uses a unit area of cm^2. The irradiance measurements themselves were measured in μW/cm^2 for visible light, and this unit is therefore also used sporadically. However, when comparing the different measurements and simulations, all units are converted to SI units.

Type of classification		Wavelength range [nm]
Ultraviolet radiation	UVC	$100 - 280$
	UVB	$280 - 315$
	UVA	$315 - 400$
Visible light	violet	$400 - 455$
	blue	$455 - 492$
	green	$492 - 577$
	yellow	$577 - 597$
	orange	$597 - 622$
	red	$622 - 780$
Infrared radiation	IR-A	$780 - 1\,400$
	IR-B	$1\,400 - 3\,000$
	IR-C	$3\,000 - 1\,000\,000$

Table 1.1: Overview of the relevant types of electromagnetic radiation for this thesis, with the classification and wavelength ranges. UV radiation from [126], visible light from [18] and IR radiation from [128].

The scope of the thesis is also defined by the limitations. In this thesis, neither shielding of infants during sunlight exposure, a tilting towards the sun during exposure, thermal effects on the infant of the direct solar exposure or other environmental and general effects of the exposure are included in the discussion. These aspects are briefly considered in section 5.7. However, the human aspect of treatment of neonatal jaundice with phototherapeutic sunlight is discussed where deemed relevant.

As fractional treatment of neonatal jaundice is not practised today to current knowledge, the potential of fractional treatment is not discussed in this thesis. However, fractional treatment may have a beneficial effect of the efficacy of phototherapy treatment, due to lesser radiant exposures and less increased pigmentation. Fractional treatment will be further discussed among future research and development in section 5.6.

1.2 Neonatal jaundice

Neonatal jaundice is a physiological condition caused by elevated bilirubin concentration in the blood serum of newborn infants [18]. Bilirubin is a yellow by-product of the breakdown of the red blood cells, and neonatal jaundice cases yellow skin, eyes and inside of mouth. Bilirubin may be either conjugated or unconjugated. The bilirubin molecule becomes conjugated when bound to sugar molecules in the liver, and such conjugation is required for the excretion of bilirubin from the body [5]. The unconjugated bilirubin has a neurotoxic potential because of its ability to cross the blood-brain barrier [16]. After the first three to five days of life, the excretion mechanisms of bilirubin becomes sufficient in most cases [1], and neonatal jaundice often peaks after three to four days of life [90]. An illustration of simulated skin colour of neonatal jaundice is shown in figure 1.1. Neonatal jaundice is treated either with phototherapy or with exchange blood transfusion (ET). The treatment of neonatal jaundice will be dealt with more thoroughly in section 2.8.

Neonatal jaundice occurs when the liver of the infant has to take over the handling of bilirubin from the placenta, which deals with bilirubin prenatally [77]. As the liver

Figure 1.1: Images illustrating the development of neonatal jaundice using the BioSpec model for skin spectral simulation. Image copied with permission from [62].

is not fully matured, some of the bilirubin is transported out to the blood circulation. When the skin has bound sufficient amounts of bilirubin to albumin molecules, a yellow discolouration is evident in the skin. This yellowing indicates the onset of neonatal jaundice [77]. Mechanisms behind the development of neonatal jaundice are, among others, that the transport mechanisms for bilirubin in the skin systems may not have been fully developed, the liver enzymes might be immature and therefore work at a diminished capacity, and that bilirubin might be reabsorbed from the intestine and recirculated in the blood stream [18].

When bilirubin is free and unbound to albumin in the skin or blood vessels, most often as unconjugated bilirubin, the molecules have a neurotoxic effect [18]. The unconjugated bilirubin may cause symptoms of varying degrees of severity [92]. Neonatal jaundice might be both significant, which necessitates treatment with phototherapy, or severe, which may require treatment with ET. At the onset of bilirubin encephalopathy, the infant displays abnormal neurological signs and symptoms caused by bilirubin toxicity to the brain [92]. Such toxicity is found when the unconjugated bilirubin binds to the central brain functions [77] and gives the brain a yellow colour [103]. The permanent or chronic neurological damage caused by high concentrations of unconjugated bilirubin is known as kernicterus [92]. In addition to irreparable neural damage, high values of unconjugated bilirubin in the blood circulation may lead to death [116]. However, kernicterus might also lead to only mild neurological symptoms.

The kinetics of the bilirubin transport is still discussed on the molecular level. This uncertainty is due to the fact that the bilirubin is not in a fixed molecular combination, and that the bilirubin synthesis, breakdown in liver and diffusion to skin happens simultaneously [143]. In the presence of treatment with phototherapy, a significant amount of the bilirubin situated in the skin is also eliminated due to photo-oxidation processes. A model of the skin-bilirubin model in the presence of phototherapy is shown in figure 1.2. This model shows the movement of the bilirubin pool formed in the body of the infant to the blood stream by a constant rate, and the bidirectional diffusion between the skin and the blood circulation. The elimination of bilirubin is also shown, both for elimination due to natural means and phototherapy. However, neither the re-transformation of unconjugated bilirubin from the photoisomers created from phototherapy nor the re-absorption of bilirubin from the intestines were included in this model [143].

The transport of bilirubin from the blood plasma to the skin is due to two mechanisms [61]. The first is the leakage of bilirubin-albumin complexes into the extra-vascular spaces, and the second is the precipitation of bilirubin acid in phospholipid membranes. The binding of unconjugated bilirubin to skin is present in both epidermis and dermis, and this binding may be augmented by application of vernix caseosa, which is the substance

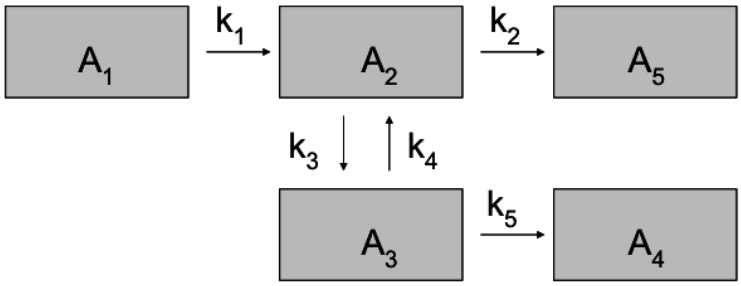

Figure 1.2: Box model of the kinetics of bilirubin in a jaundiced infant in the presence of phototherapy. A_1 is the bilirubin pool, A_2 is the bilirubin in the intra-vascular compartment, A_3 is the bilirubin compartment in the skin, A_4 is the bilirubin compartment eliminated by phototherapy and A_5 is the bilirubin compartment eliminated naturally. The change rates are denoted by k, and k_1 is the rate of bilirubin formation, k_2 is the rate of naturally eliminated bilirubin, k_3 is the rate of bilirubin moving from blood circulation to skin, k_4 is the rate of bilirubin moving from skin to blood circulation, and k_5 is the constant rate of phototherapy. Figure adapted from [143].

coating the skin of newborn infants [77]. It has been found that the intensity of the yellow colour of the jaundiced skin is positively correlated with the plasma bilirubin concentration, the squared hydrogen ion concentration, and the reciprocal of the reserve albumin concentration [61]. This result is substantiated by the observation that the binding of bilirubin takes place within a pH-range of $6 - 9$, and that the binding capacity of human serum increased for an elevation in pH since bilirubin is weakly acidic [60]. Kapoor and Krishna Murti [60] found also unequivocal evidence that epidermal segments may pick up bilirubin in free or bound form *in vitro*, and that the major part of the uptake is as unconjugated bilirubin.

The effect of phototherapy treatment comes from the photoisomerisation of unconjugated bilirubin. Unconjugated bilirubin is highly lipophilic, which means that it binds to fat with high affinity and which facilitates transport through tissue membranes [18]. The interactions of photons with bilirubin bound to albumin molecules in the skin create photochemical reactions, and the unconjugated bilirubin changes to other configurations, or isomers, in reversible processes. The principal excretion of bilirubin is found through the structural isomer of lumirubin, which is more water soluble than other configurational isomers [18]. Lumirubin is rapidly excreted into the bile, the photo-reaction back to the neurotoxic photoisomer is slow, and the serum concentration of lumirubin increases with increased irradiance of phototherapy.

Both levels of lumirubin and other reversible photoisomers depend on the spectrum of the phototherapy [1]. The maximum wavelength for absorption in bilirubin changes according to the form of the molecule. For bilirubin *in vitro*, the absorption maximum occurs at around 460 nm, while for bilirubin bound to albumin in the skin, *in vivo*, the absorption maximum is between $480 - 500$ nm [1, 18].

The risk factors of developing neonatal jaundice for infants are among others prematurity, an African or Asian ethnicity, or infants where the mother has a different blood type than the fetus [85, 90, 121]. Another risk factor is glucose-6-phosphate dehydrogenase

(G6PD) deficiency. G6PD deficiency is the most prevalent enzyme deficiency in the world, and primarily affects populations of African and Mediterranean descent [87]. In Nigeria, it is reported by Ezeaka et al [31] that 5.5% of all newborns have clinically significant neonatal jaundice which requires treatment. This rate is possibly the highest worldwide, which might be due to the incidence of G6PD-deficiency. The need for a G6PD screening is also addressed specifically by Slusher et al [116] in the discussion regarding means of reduction of the the mortality and long term effects of severe neonatal jaundice.

Neonatal jaundice and the resulting brain damage is a problem of global proportions [116]. However, the condition is highly treatable and reversible. The treatment of neonatal jaundice requires only the use of existing technology in low-income countries. The global problem of kernicterus can thus be prevented [116]. Creating a treatment plan for treatment of neonatal jaundice with the use of controlled sunlight exposure may be a good alternative where conventional phototherapy is unavailable.

Chapter 2

Theory

In this chapter, all relevant theory concerning the thesis is presented. The chapter is defined as general as possible, starting with the basic properties and physical definitions of radiative transfer and continuing with the special considerations. The most relevant types of irradiation in this thesis are sunlight and phototherapeutic irradiation, while the most relevant materials for radiative transfer are atmospheric air and biological tissue. The most relevant radiation is optic radiation of wavelengths in the UV, visible and IR wavelength ranges, as defined in table 1.1.

2.1 Radiometric quantities

Several different and related quantities are used in the description and measurement of radiation. There are many different ways to define these quantities, and they are often defined differently for atmospheric and biological situations. All quantities used in this thesis are defined in this section, with both the unit and the method of calculation.

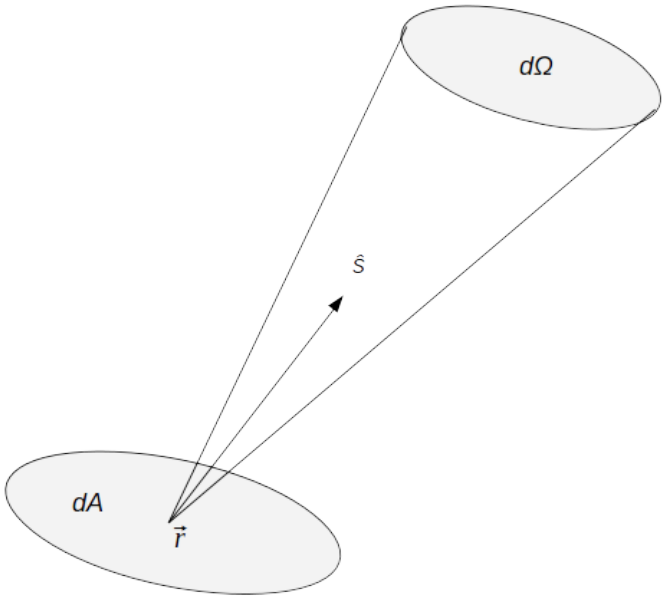

Figure 2.1: Illustrating the definition of spectral radiance L_ν.

Radiant power P

Def: Radiant power is the power emitted, transferred or received as radiation.

Unit: $[P] = \text{W}$

Spectral radiance L_ν

Def: Spectral radiance is the power per unit area, per unit solid angle, per unit frequency interval in the neighbourhood of the frequency ν, at a point $\vec{r}$ in the direction $\hat{s}$ [4, p.57]. The spectral radiance is illustrated in figure 2.1.

Unit: $[L_\nu] = \text{W/(m}^2 \text{ sr Hz)}$

Radiance L

Def: Radiance is the integral of L_ν over all frequencies ν, given by [4, p.58]

$$L(\vec{r}, \hat{s}) = \int_0^\infty L_\nu(\vec{r}, \hat{s})\, d\nu.$$

The radiance is power per unit area, per unit solid angle at a point $\vec{r}$ in the direction of the unit vector $\hat{s}$.

Unit: $[L] = \text{W/(m}^2 \text{ sr)}$

Spectral irradiance E_ν

Def: Spectral irradiance is the power per unit area, per unit frequency interval, at a point $\vec{r}$ through a surface of normal $\hat{n}$. Spectral irradiance is obtained from the spectral radiance by integration over a half sphere on one side of the surface, that is [4, p.58]

$$E_\nu(\vec{r}, \hat{n}) = \int_{2\pi} L_\nu(\vec{r}, \hat{s}) \hat{n} \cdot \hat{s}\, d\Omega,$$

where $d\Omega$ is the element of the solid angle in the direction $\hat{s}$. The scalar product $\hat{n} \cdot \hat{s}$ arises from the projection of the unit area perpendicular to $\hat{s}$ in the direction $\hat{n}$ of the normal. The irradiance thus has a specific direction associated with it. Spectral irradiance is also called monochromatic irradiance.

Unit: $[E_\nu] = \text{W/(m}^2 \text{ Hz)}$

Irradiance E

Def: Irradiance is the power per unit area at a point $\vec{r}$ through a surface of normal $\hat{n}$. Irradiance can either be described as the integral of E_ν over all frequencies ν or as the integral of L over a hemisphere, such that [4, p.58]

$$E(\vec{r}, \hat{n}) = \int_0^\infty E_\nu(\vec{r}, \hat{n})\, d\nu = \int_{2\pi} L(\vec{r}, \hat{s}) \hat{n} \cdot \hat{s}\, d\Omega.$$

Irradiance is also called flux density.

Unit: $[E] = \text{W/(m}^2\text{)}$

Radiant exposure D

Def: Radiant exposure is defined as the irradiance E multiplied with the exposure time t, such that [21]

$$D(\vec{r}, \hat{n}, t) = E(\vec{r}, \hat{n}) \cdot t.$$

This equals the received radiant energy over a specified time. In this thesis, radiant exposure might also be called dose, although dose is most often defined per unit mass of material [65, p.185].

Unit: $[D] = \text{J/(m}^2\text{)}$

Fluence rate Φ

Def: Fluence rate is defined as the energy flow per unit area, regardless of the flow direction. Fluence rate is expressed as the radiance integrated over the entire solid angle, such that [139, p.84]

$$\Phi(\vec{r}, t) = \int_{4\pi} L(\vec{r}, \hat{s}, t)\, d\Omega.$$

Fluence rate is the non-directional counterpart of the irradiance E.

Unit: $[\Phi] = \text{W/(m}^2\text{)}$

Fluence F

Def: Fluence F is defined as the time-integrated fluence rate, which gives [139, p.84]

$$F(\vec{r}) = \int_{-\infty}^{+\infty} \Phi(\vec{r}, t)\, dt.$$

The fluence is the equivalent to radiant exposure for the fluence rate Φ.

Unit: $[F] = \text{J/(m}^2\text{)}$

2.2 Interaction of radiation and matter

There are several ways radiation may interact with matter. The matter may be either molecules in air or biological tissue. The basic physical properties will be discussed in this section. The specific interactions of radiation with air and biological tissue will be detailed in later sections.

The two most important interactions between radiation and surrounding matter are absorption and scattering. The effect of incident molecules on the incoming radiation is dependent on the properties of the molecules. Both the absorption coefficient μ_a and the scattering coefficient μ_s depend on if the radiation interacts with the molecule in question. The probability for such interaction is described by the particle cross section.

The cross section, denoted by σ, is a measure of the incident area of a molecule where the radiation will encounter interaction. This cross section can be calculated by the use of

Maxwell's equations [15], as shown by Spott in his dissertation [120]. Cross sections are related to the geometric cross-sectional area σ_g through the probable interaction efficiency. The absorption cross section is given by [139, p.5]

$$\sigma_a = Q_a \sigma_g, \tag{2.1}$$

where Q_a is the absorption efficiency. The scattering cross section is described analogously, which gives [139, p.8]

$$\sigma_s = Q_s \sigma_g. \tag{2.2}$$

Here, Q_s is the scattering efficiency.

For an ensemble of particles, Maxwell's equations might show that the cross sections of the particles are additive, as summarised by Spott [15, 120]. The total cross section for an ensemble of k particles then becomes

$$\sigma_{tot} = \sum_k \sigma_k, \tag{2.3}$$

where σ_{tot} is the total cross section and σ_k is the individual cross sections of the particles. This additive behaviour is only valid when the situation is restricted to incoherent scattering. For incoherent scattering, the fields scattered from the single particles must not influence each other and the separations between particles must be uncorrelated during any measurement time [15, 120].

2.2.1 Absorption, scattering coefficients and mean free path

The absorption coefficient μ_a is defined as the probability of photon absorption per unit path length [139, p.5]. The absorption coefficient is the total cross sectional area for absorption per unit volume, which gives

$$\mu_a = N_a \sigma_a, \tag{2.4}$$

where N_a is the absorber number density.

For radiation travelling through a medium with thickness dx in the propagation direction, the light will be attenuated as

$$dP = -P_0 \mu_a dx \tag{2.5}$$

according to the definition of the absorption coefficient, where P_0 is the power incident on the medium. Equation (2.5) can be transformed into

$$P(x) = P_0 e^{-\mu_a x}, \tag{2.6}$$

which is known as Beer's law [139, p.5].

The scattering coefficient μ_s is defined as the probability of a photon scattering in a medium per unit path length. This definition is analogous to the definition of the absorption coefficient in equation (2.4). The scattering coefficient becomes

$$\mu_s = N_s \sigma_s, \tag{2.7}$$

where N_s is the scattering number density. Provided that the scattering contribution is small ($\mu_s x \ll 1$), scattering processes may also be described by Beer's law from equation (2.6) with μ_s replacing μ_a [9, 15, 120]. Scattering processes obey Beer's law more specifically if only single scattering occurs and if the scattering cross section is defined [9]. These conditions apply for, among others, dilute suspensions and molecular beam scattering in gaseous media [9], which includes the atmosphere.

For materials that are both absorbing and scattering, the extinction coefficient μ_t is used. This extinction coefficient, or total attenuation coefficient, is defined by

$$\mu_t = \mu_a + \mu_s. \tag{2.8}$$

The unit of the extinction coefficient is $[\mu_t] = m^{-1}$, which is the unit of both the absorption and scattering coefficients as well.

The mean free path l_t is the average distance between interaction events [139, p.8], which might be scattering or absorption. The mean free path is the reciprocal of the extinction coefficient, so that

$$l_t = \mu_t^{-1}. \tag{2.9}$$

The mean free path has unit $[l_t] = m$. The absorption free mean path l_a and the scattering mean free path l_s are defined analogously,

$$\begin{aligned} l_a &= \mu_a^{-1}, \\ l_s &= \mu_s^{-1}. \end{aligned} \tag{2.10}$$

All mean free paths have the same unit.

2.2.2 The reduced scattering coefficient

In most matter, a photon will encounter more than one scattering event. The case of multiple scattering events gives an angular distribution, which changes the propagation distance in the medium. This effect leads to the reduced scattering coefficient μ_s', which is defined as the distance from the surface of a medium where a scattering photon has lost all information about its original direction of motion [63, 120].

Immediately after a photon starts propagating through a medium, it travels a distance of l_s before scattering. The scattering leaves the photon deflected by an angle θ, and the photon travels a distance l_s in the new direction before scattering again. The new distance from the surface is given by $l_s \cos\theta$. The photon continues in the same manner until it is absorbed or scattered back out of the medium.

The average cosine of the polar scattering angle θ is now defined as

$$g = \langle \cos\theta \rangle, \tag{2.11}$$

where g is the scattering anisotropy. The distance between two scattering events is now given by $l_s g$. This process is illustrated in figure 2.2, where the first two scattering events from a photon entering a material can be seen. The photon is scattered with angles θ_1 and θ_2, respectively, and the distance between the photon and the surface of the material in the original direction of propagation becomes l_s after just entering the material, then $l_s g$ after the first scattering event and $l_s g^2$ after the second. When following this reasoning,

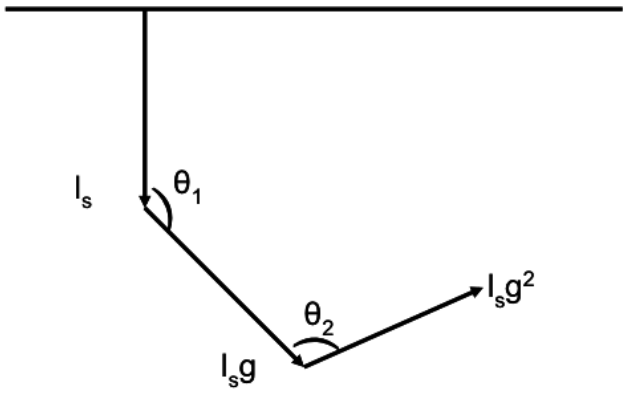

Figure 2.2: Illustration of a photon for two scattering processes after entering a material. The scattering angles are θ_1 and θ_2, and the mean distance between each scattering event is l_s while g is the scattering anisotropy. The distance from the surface is l_s, $l_s g$ and $l_s g^2$ after entering the material and the two scatterings, respectively.

the propagation in the original direction of propagation is given by $l_s g^n$ for n multiple scattering events.

Because $g < 1$, the projection of the mean free path length in the original direction of motion will eventually become zero. When this development has occurred, the photons are as likely to travel in any direction of motion. This event is the definition of the reduced scattering mean free path, which is given by

$$l'_s = l_s \sum_k g^k = \frac{l_s}{1-g}. \tag{2.12}$$

The reduced scattering mean free path defines the reduced scattering coefficient, which becomes

$$\mu'_s = l'^{-1}_s = \mu_s(1-g). \tag{2.13}$$

The reduced scattering mean free path from equation (2.13) together with the absorption coefficient from equation (2.4) define the transport coefficient as

$$\mu_{tr} = \mu_a + \mu'_s = \mu_a + \mu_s(1-g). \tag{2.14}$$

The transport coefficient is analogous to the extinction coefficient μ_t from equation (2.8).

2.2.3 Phase function

The phase function $P(\hat{s}', \hat{s})$ expresses the probability distribution for the deflection of a photon from direction $\hat{s}'$ into a direction $\hat{s}$ in a scattering event [120]. This phase function is required to describe the angle that a photon is deflected upon scattering. The phase function is named after the original astronomical usage, where the term *phase* refers to the variation of planetary brightness versus the angle between the vectors from the Earth to the planet and the sun to the planet, respectively [130, p.83]. This angle is called the *phase angle*, and must not be confused with the phase of an electromagnetic wave.

As a probability density function, the phase function is expressed as [139, p.87]

$$\int_{4\pi} P(\hat{s}', \hat{s})\, d\Omega = 1. \tag{2.15}$$

This equation describes the normalization of the scattering pattern, and is viable even for non-spherical scatterers [120]. Often, the phase function only depends on the angle between the scattered and incident directions [139, p.87]. This approximation gives that

$$P(\hat{s}', \hat{s}) = P(\hat{s}' \cdot \hat{s}), \tag{2.16}$$

where $\hat{s}' \cdot \hat{s}$ equals the cosine between the two directions so that $(\hat{s}' \cdot \hat{s}) = \cos\theta$.

There are several different phase functions. The most popular [66] is the Henyey-Greenstein phase function given by [47]

$$P_{HG}(\cos\theta) = \frac{1}{4\pi} \frac{1 - g^2}{2(1 + g^2 - 2g\cos\theta)^{3/2}}, \tag{2.17}$$

where g is the scattering anisotropy. This phase function was originally proposed for galactic scattering [139, p.46]. However, the Henyey-Greenstein phase function has no physical basis and should be considered as a one-parameter analytic fit to an actual phase function [130, p.189]. It is only the many satisfactory results that justifies the common application of this phase function, together with the convenient fact that only g is needed to define $P_{HG}(\cos\theta)$ [120]. The Henyey-Greenstein phase function also has a desirable feature in that it yields complete forward scattering for $g = 1$, isotropic scattering for $g = 0$ and complete backward scattering for $g = -1$ [130, p.190].

2.2.4 Rayleigh scattering and Mie scattering

When a plane monochromatic optical wave is scattered by a single particle with radius a, there are several ways to model the resulting scattering. The two most important models are Mie scattering and Rayleigh scattering. The summaries of these two scattering models are presented here. For the full derivation, the reader is referred to Wang and Wu [139, p.23-34]. Mie and Rayleigh scattering determine the scattering of particles in both tissue and air.

The effective scattering cross section differs from the geometric cross section for most particles, independent of the size of the particle compared to the optical wavelength [139, p.17]. The scattering cross section is given in equation (2.2), and depends on the scattering efficiency Q_s. Both the scattering efficiency and the scattering anisotropy g from equation (2.11) is determined by the scattering models.

In figure 2.3, the directional distribution of both Rayleigh scattering and Mie scattering can be seen, in addition to scattering of larger particles when $a \gg \lambda$. This scattering from larger particles is often called geometric or optical scattering [30], and will not be covered in this thesis. Both Rayleigh scatter theory and Mie scatter theory assume spherical scatter particles.

Rayleigh scattering

Rayleigh scattering models the scattering of radiation by particles that are much smaller than the optical wavelength so that $a \ll \lambda$. The particles see the incident radiation as a

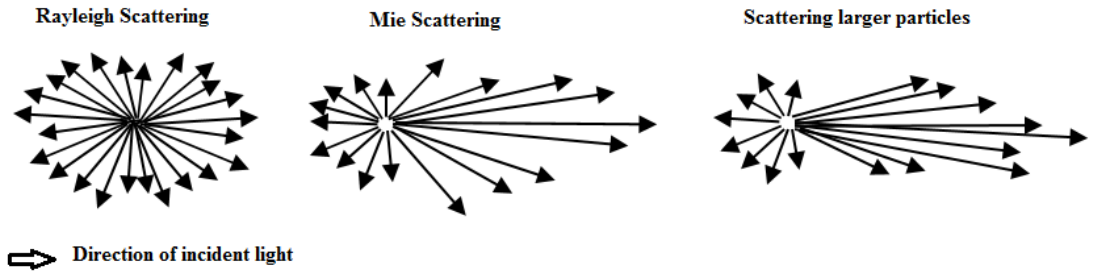

Figure 2.3: Illustration of the directional distribution of radiation from Rayleigh scattering and Mie scattering for particles of different sizes. Figure taken from [2].

plane electromagnetic wave, and the electrons in the particle oscillate in the $\vec{E}$-field of the radiation [30]. This oscillation causes a re-radiation of the light in all directions, with a slight partiality to the direction parallel to and opposite of the incident light [30]. This behaviour can be seen in figure 2.3.

The propagation constant k in the background medium where the radiation propagates in the z-direction of a spherical coordinate system, is given by

$$k = \frac{2\pi n_b}{\lambda}, \tag{2.18}$$

where n_b is the refractive index of the background medium and λ is the wavelength in vacuum [139, p.18]. When this value of the propagation constant k is used, it can be shown that the Rayleigh scattering cross section is proportional to $\propto 1/\lambda^4$ [130, p.73]. This wavelength-dependence favours short wavelengths.

The scattering cross section is given by [139, p.18]

$$\sigma_s = \frac{8\pi k^4 |\alpha|^2}{3}, \tag{2.19}$$

where α is the polarization of a sphere with radius a and is given by

$$\alpha = \frac{n_{\text{rel}}^2 - 1}{n_{\text{rel}}^2 + 2} a^3. \tag{2.20}$$

Here n_{rel} is the relative refractive index of the particle such that $n_{\text{rel}} = n_s/n_b$, where n_s is the refractive index of the sphere.

Substituting equation (2.20) into equation (2.19) and setting the size parameter $x = ka$, gives the scattering cross section

$$\sigma_s = \frac{8\pi a^2 x^4}{3} \left| \frac{n_{\text{rel}}^2 - 1}{n_{\text{rel}}^2 + 2} \right|^2. \tag{2.21}$$

By further substituting the size parameter $x = ka$ and equation (2.18) into equation (2.21), the scattering efficiency can be determined to [139, p.19]

$$Q_s = \frac{8x^4}{3} \left| \frac{n_{\text{rel}}^2 - 1}{n_{\text{rel}}^2 + 2} \right|^2, \tag{2.22}$$

which can be reduced to

$$Q_s = \frac{32x^4}{27}|n_{\text{rel}}^2 - 1|^2 \tag{2.23}$$

when n_{rel} is close to unity. This scattering efficiency is only dependent on the refractive indices of the background medium and the particle, the wavelength of the incident radiation and the radius of the spherical particle.

The scattering anisotropy g is set equal to zero for Rayleigh scattering, as the scattering has an approximately isotropic distribution.

Mie scattering

Mie scattering models the scattering from a spherical particle with any radius a. For small particles, the theory reduces to Rayleigh scattering. In Mie scattering, the particles see a curved wavefront, which induces diffraction effects around the particle. For Mie scattering, the cross section is larger than the geometric cross section by approximately a factor of 2 [30]. Mie scattering scatters mostly in the forward direction as be seen in figure 2.3.

Application of Mie theory is largely straightforward, and only requires application of the equations that define the scattering efficiency Q_s and the scattering anisotropy g, as defined in equation (2.11). However, the derivation of the equations that describe Mie theory are not straightforward. This derivation may be found in [139, p.26-34]. The results are stated without further explanation in the following equations, where the size parameter is again defined as $x = ka$ with k from equation (2.18). The scattering efficiency becomes [139, p.20]

$$Q_s = \frac{2}{x^2}\sum_{l=1}^{\infty}(2l+1)(|a_l|^2 + |b_l|^2), \tag{2.24}$$

and the scattering anisotropy becomes

$$g = \frac{4}{Q_s x^2}\sum_{l=1}^{\infty}\left[\frac{l(l+1)}{l+1}\Re(a_l a_{l+1}^* + b_l b_{l+1}^*) + \frac{2l+1}{l(l+1)}\Re(a_l b_l^*)\right], \tag{2.25}$$

where $*$ denotes the complex conjugate and $\Re$ denotes the real component of a complex variable. The coefficients a_l and b_l are given by

$$\begin{aligned} a_l &= \frac{\Psi_l'(y)\Psi_l(x) - n_{\text{rel}}\Psi_l(y)\Psi_l'(x)}{\Psi_l'(y)\zeta_(x) - n_{\text{rel}}\Psi_l(y)\zeta_l'(x)}, \\ b_l &= \frac{n_{\text{rel}}\Psi_l'(y)\Psi_l(x) - \Psi_l(y)\Psi_l'(x)}{n_{\text{rel}}\Psi_l'(y)\zeta_(x) - \Psi_l(y)\zeta_l'(x)}, \end{aligned} \tag{2.26}$$

where Ψ_l' denotes the first-order differentiation of Ψ_l, the size parameter y is defined by

$$y = n_{\text{rel}}x = \frac{2\pi n_s a}{\lambda},$$

and Ψ_l and ζ_l are two of the Riccati-Bessel functions [139, p.21].

2.3 Radiative transfer

All radiation interacts with the environment in several ways. The incoming radiation is both absorbed, re-emitted and scattered by the surroundings. These effects create a radiation field, which is described by the radiation transport equation (RTE) [20, p.1], given by

$$\frac{\partial L(\vec{r},\hat{s},t)/c}{\partial t} = -\hat{s}\cdot\nabla L(\vec{r},\hat{s},t) - \mu_t L(\vec{r},\hat{s},t) + \mu_s \int_{4\pi} L(\vec{r},\hat{s},t)P(\hat{s}'\cdot\hat{s})\,d\Omega' + S(\vec{r},\hat{s},t). \tag{2.27}$$

This equation describes the way in which radiative power is affected by the extinction and emission of radiation [4, p.61]. The term on the left side of the equation is the total change of energy, and the terms on the right side of the equation are, left to right, the divergence of radiation, the extinction, or energy loss, of the radiation, the scattering of the radiation, and a source term.

There are several ways to derive the general radiative transport equation, and all make use of certain approximations. In appendix B, the general equation is first derived by using conservation of energy according to the method from Wang and Wu [139]. The special cases of atmospheric radiation and radiation transport in biological tissue are detailed in the following sections.

2.4 Radiative transfer in the atmosphere

For the atmosphere, the radiative transfer function can often be simplified. If the atmosphere is in local thermodynamic equilibrium for instance, the source function of the radiative transport equation may be simplified to the Planck function [20, p.8]. The Planck function is given by [4, p.54]

$$B_\lambda(T) = \frac{2hc^2}{\lambda^5}\frac{1}{e^{hc/(\lambda k_B T)}-1}, \tag{2.28}$$

where λ is the wavelength, T is the temperature in Kelvin, h is the Planck constant, k_B is the Boltzmann constant and c is the speed of light in vacuum. The Planck function describes black body radiation when integrated over all wavelengths λ [4, p.55], which the radiation from the sun might be approximated to [48]. Local thermodynamic equilibrium occurs when the temperature T is uniform in a portion of the atmosphere, due to the molecular collisions causing a sufficiently high pressure [4, p.57]. When dealing with visible light interaction in the atmosphere, the source term may be neglected as the temperature of the Earth causes the emitted radiation to have wavelengths mostly in the IR region.

The radiative absorption of the atmosphere is highly dependent on the gases present. The solar spectral irradiance in the atmosphere is shown in figure 2.4, and it can be seen that the spectrum is markedly different at the top of the atmosphere compared to at the surface. This difference comes from absorption and scattering in the atmosphere. Due to the different molecular compositions, different gases absorb radiation with different wavelengths. The most prominent absorption bands are indicated in figure 2.4 with the atmospheric gas responsible.

The scattering in the atmosphere is dependent on the size of the scattering particles. Molecules in the atmosphere have a radius of $a \approx 0.1\,\text{nm}$, which is smaller than the incident radiation by a factor of more than 10^3. Molecular scattering will therefore follow

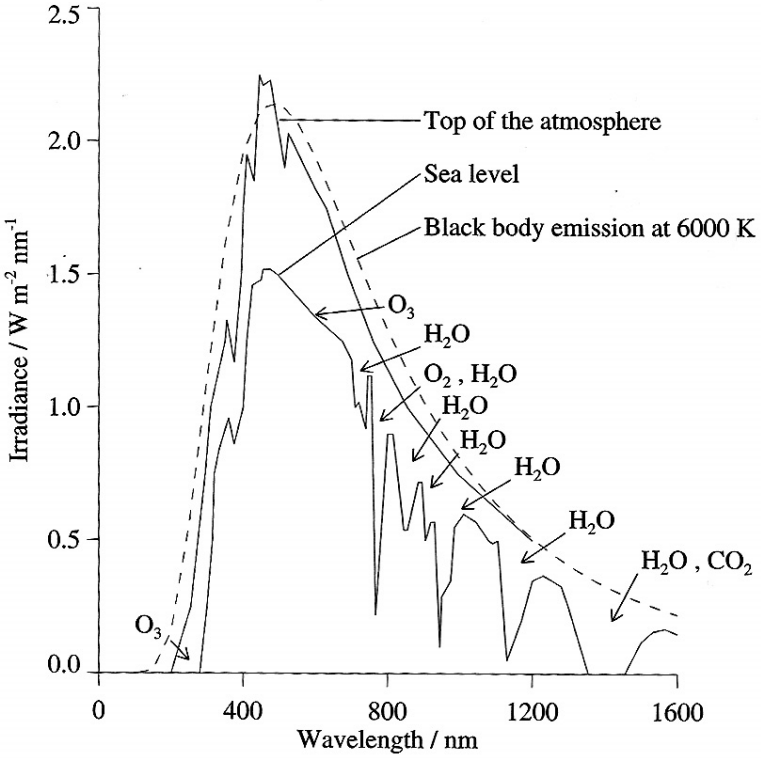

Figure 2.4: Irradiance spectrum of solar radiation at the top of the atmosphere and at sea level, compared with the black body radiation from the sun. Gases responsible for the most prominent absorption features are indicated. Figure copied from [48], similar figure found in [4, p.71].

Rayleigh theory. Larger particles, for instance dust, cloud particles or pollution, will on the other hand follow Mie scattering.

The colour of the sky is highly dependent on the type of scattering in the atmosphere. When Rayleigh scattering dominates, the sky appears blue to an observer on the surface due to strong scattering of short wavelengths. This proportionality means that red light is scattered less than blue light during Rayleigh scattering, and will seem to propagate more straight forward. The colour of the sky at different times is illustrated in figure 2.5. In this figure, it can be seen how the blue radiation is scattered more towards the surface for midday radiation, while the blue light is scattered before reaching the observer at sunset.

Rayleigh scattering of short wavelengths applies to shorter wavelengths than blue visible light as well. For instance UV radiation is scattered more when the atmospheric path of the incident photons is longer. Due to this increased scattering, the ratio of visible light to UV radiation is higher for larger solar zenith angles [107]. As a result, there is less UV radiation at surface level when the sun is low in the sky.

Mie scattering dominates when the atmosphere is less transparent, for instance when the aerosol content of the atmosphere is large or when the cloud level is thicker. In these cases, the molecules that encounter the incoming radiation are larger. Mie scattering does not favour blue visible radiation in the same matter as Rayleigh scattering, which means that the sky appears white or grey. However, short wavelengths are still scattered to a great extent. As a result of several atmospheric simulations for different atmospheric

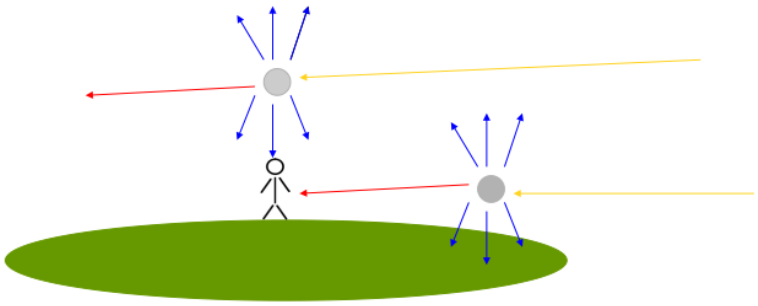

Figure 2.5: Illustration of the colour of the atmosphere, as appearing to an observer on the ground. The molecules in the atmosphere scatter mostly according to Rayleigh theory, which favours the blue visible radiation compared to the red according to a wavelength dependence of $\propto 1/\lambda^4$. The blue light is scattered perpendicular to the light propagation, and is observed at the surface during mid-day. During afternoon, the blue light is scattered before reaching the observer, while the red visible light is scattered less and is therefore visible to the observer. Figure inspired by [30].

conditions, it was found that the ratio of visible radiation to UV radiation increased for decreasing transparency of the atmosphere [107]. This increasing ratio indicates that for shorter wavelengths, the incoming radiation encounters more scattering and absorption in the atmosphere than for longer wavelengths. This effect is especially clear for less transparent atmospheres, or for long atmospheric paths when the solar zenith angle is large.

2.4.1 Atmospheric parameters and their impact on incident irradiation

There are several atmospheric parameters that impact the incident irradiation greatly. The most important are, in decreasing order, the solar zenith angle and geographical location, the cloud optical depth, the thickness of the ozone layer, the albedo and the aerosol visibility [107]. These parameters will be described in this section.

Another parameter that may impact the incoming irradiation is the solar distance, which is the distance from the Earth to the sun. This distance changes yearly because of the elliptical orbit of the Earth. However, this parameter only impacts the total extraterrestrial irradiation, and thus is not connected to the transmittance of the atmosphere. When investigated, as was done in [107], it can also be seen that the variance as a function of day of year is very small, with a slight decrease of the extraterrestrial irradiation in the middle of the year. This decrease has been neglected in this thesis.

Solar zenith angle

Solar zenith angle is the most important parameter influencing the incoming solar irradiance through the atmosphere. This angle is defined as the angle between the noon zenith and the position of the sun, as seen in figure 2.6. The irradiance at the surface is proportional to the cosine of the solar zenith angle [49], which means that at $\theta = 0$, the irradiance at the surface is equal to the transmitted solar irradiance.

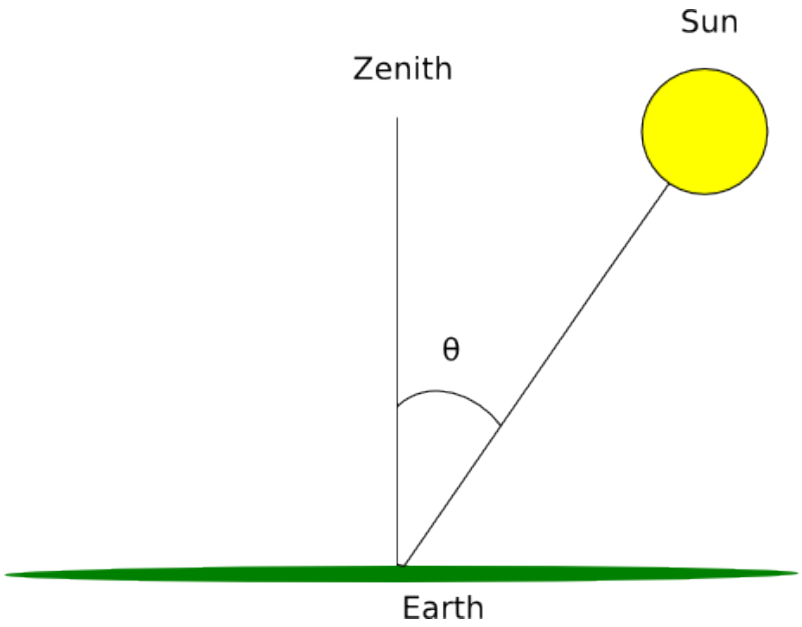

Figure 2.6: Illustration of the solar zenith angle θ.

The solar zenith angle may be computed according to the algorithm described by Iqbal [53, p.15], which gives

$$\cos(\theta) = \sin(\delta) \cdot \sin(\phi) + \cos(\delta) \cdot \cos(\phi) \cdot \cos(\omega). \tag{2.29}$$

Here, θ is the solar zenith angle, δ is the solar declination, ϕ is the geographic latitude and ω is the hour angle [53, p.15][72]. The solar hour angle ω is the angle measured at the celestial pole between the observer's degree of longitude, or meridian, and the solar degree of longitude [53, p.15]. The celestial pole is either the South pole or the North pole, depending on which hemisphere the solar zenith angle is measured for [53, p.6]. The hour angle is zero at noon and positive for morning hours [53, p.15]. The geographic latitude ϕ is measured in degrees, with north positive [53, p.15]. The solar declination δ is the angular position of the sun at solar noon with respect to the plane of the equator measured in degrees, with positive values to the north [53, p.15].

The solar zenith angle throughout each day changes as a function of both latitude, time of day and day of year. It is therefore highly connected to geographical location. At equator, the solar zenith angle at local noon is close to zero during the entire year, while at the polar circles the sun does not rise in midwinter and does not set during midsummer [81]. If the day of year and geographical coordinates are known, the solar zenith angle may be computed for any given time of day by using equation (2.29).

Cloud optical depth

The cloud optical depth is denoted τ, and is a measure of the amount of clouds in the atmosphere. This amount is an approximation of the effect of weather on the incoming irradiation. Cloud optical depth is a measure of how far a single photon travels downwards in the atmosphere [4, p.62]. For optically thick atmospheres, the photons are more likely to be absorbed and scattered than for optically thin atmospheres.

Weather and cloud layer are important atmospheric parameters, as a cloudy day gives much less incident irradiation. A clear day might give losses of 25% due to atmospheric scattering, while a light cloud cover may give losses of 50% and a dark thundery sky may give losses of above 90% [19]. For instance, Gelsor et al [35] found that the average loss of yearly radiant exposure due to cloud cover on the Tibetan plateau was 23% compared to a hypothetical all year clear sky. This amount of reduction corresponds to a very light cloud cover, which is substantiated by available weather statistics for Lhasa, Tibet, which show no precipitation from November until March, and an average of 56 days of precipitation during an entire year [129].

Ozone layer

The ozone layer is situated in the stratosphere, which is of an altitude between 20 km and 40 km in the atmosphere [4, p.8]. The ozone layer has a great impact on the atmospheric transmittance of short wavelength radiation, and absorbs most of the UV radiation and all of the UVC radiation. All radiation with wavelengths below approximately 290 nm is absorbed in the atmosphere by the ozone layer and other air molecules.

The thickness of the ozone layer varies greatly, and this variability may be as large as 20% on any given day [106]. The variability is larger in winter and spring. Annual cycles of ozone show a worldwide thicker layer of ozone in March and April, with the lowest values in October and November. There are also spatial variations, and the largest values of ozone are found above Northern Europe, Canada and Siberia [106].

Albedo

The albedo is the amount of reflected irradiation from the surface, and is defined as the ratio of the up-welling irradiance reflected from the surface to the down-welling solar irradiance. According to Iqbal [53, p.281], the term albedo often refers to the reflectance when dealing with solar irradiance. The albedo ranges from 0 to 1, and is dependent on the type of surface, the wavelength and the solar zenith angle [42]. However, to first approximation the albedo is reasonably constant as a function of solar zenith angle up to $\theta = 40^\circ$. For wavelength dependence, the albedo is higher for visible light than for shorter wavelengths with the exception of snow [53, p.285]. As a whole, the albedo of the Earth is assumed to be 0.3, or 30%.

Aerosols

Aerosols are macroscopic particles in the atmosphere, which interfere with sunlight by processes of Mie scattering and absorption. Aerosols may scatter radiation directly back to space, change the cloud properties of the atmosphere, or react chemically with gases present in the atmosphere. Aerosols may be observed as a haze, or in the reddening of sunsets and sunrises [3].

There are several types of aerosols, and to derive the optical properties of the scattering and absorption effects, the mean particle size and refractive index must be known [130, p.341]. The most important types of aerosols for atmospheric effects originates in volcanic eruptions, desert storms and human-made aerosols [3]. Above 2 km in the atmosphere, background aerosols such as volcanic ash is dominant.

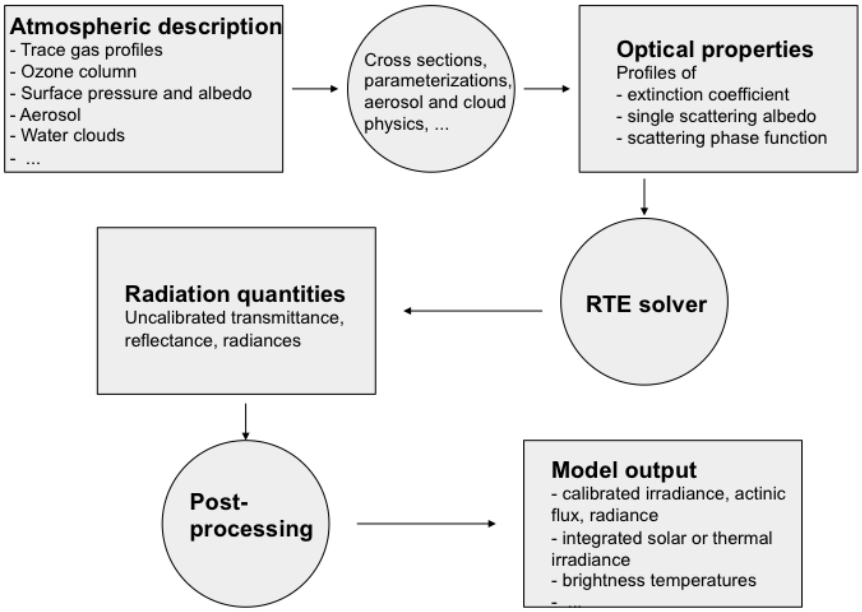

Figure 2.7: Structure of the uvspec model in libRadtran*, based on [73].*

2.4.2 *libRadtran*

To calculate the incoming irradiance through the atmosphere, the radiative transfer equation from equation (2.27) must be solved with respect to the description of the optical parameters of the relevant atmosphere. There are several ways to calculate this solution, one of which is the software package *libRadtran*. The *libRadtran* program keeps account of the amount of incident radiation from the sun and the directional resulting radiation throughout the atmosphere [74]. This algorithm makes it possible to calculate the incident irradiation at all levels in the atmosphere, and for varying atmospheric parameters.

In *libRadtran*, there are many different tools that may be used to address various problems related to atmospheric radiation, such as calculating solar zenith angles or the optical properties of specific water clouds. The main tool is the uvspec radiative transfer model [73], and this tool includes several RTE-solvers. The structure of the uvspec model can be seen in figure 2.7. The solvers included in the uvspec model are the DISORT and MYSTIC among others, where the first is a discrete ordinate solver and the latter is a Monte Carlo solver that follows each individual photon [73, 74]. However, the MYSTIC solver is not available with all versions, and thus the DISORT solver is often the most relevant.

In this thesis, the DISORT solver was used to calculate spectral irradiance at the surface for radiation of wavelengths between $200 - 500$ nm. The wavelengths between $500 - 800$ nm were calculated by using molecular absorption, which was parametrized with the LOWTRAN band model [95] as adopted from the SBDART code [100].

2.5 Radiative transfer in biological tissue

Most biological tissues are characterized by strong optical scattering, and are often referred to as turbid media [139, p.2]. The optical absorption however, is weak in the wavelength range of $600 - 1200$ nm for biological tissue. Photon propagation in biological tissue often follows a diffusion-like behaviour, depending on the depth of tissue, wavelength and type of tissue. The photon propagation may be modelled in two ways, both based on the radiative transport equation from equation (2.27). These two ways are by the diffusion approximation, and by Monte Carlo modelling. All modelling requires knowledge of several optical parameters. These parameters will be described in the following sections.

2.5.1 Absorption in skin

Optical absorption in biological tissue originates primarily from hemoglobin, melanin and water. As water has low absorption at wavelengths below 1000 nm [139, p.7], the absorption of water will not be included in this thesis. The absorption coefficients of hemoglobin can be seen in figure 2.8, and the absorption coefficient for melanin can be seen in figure 2.9.

Hemoglobin has two forms, oxygenated hemoglobin denoted HbO_2 and deoxygenated hemoglobin denoted Hb. The ratio of the two types of hemoglobin is dependent on the oxygenation of the blood. Absorption effects dominates scattering effects in hemoglobin [139, p.6].

Melanin absorbs short wavelengths stronger than long wavelengths, as can be seen in figure 2.9. The absorption coefficient of melanin in skin might be modelled as an exponential function of the form [54]

$$\mu_a^m = 1.70 \cdot 10^{12} \cdot \lambda^{-3.48}, \tag{2.30}$$

where λ is the wavelength given in nm. The amount of melanin and pigmentation present in the skin is assumed dependent on the skin type, which will be covered in section 2.6.

For infants suffering from neonatal jaundice, the presence of bilirubin will also affect the scattering and absorption of the skin. The bilirubin absorption coefficients in skin concerning different chemical and physical properties are however not uniquely determined yet. In this thesis, bilirubin is described with an action spectrum, which will be detailed in section 2.7.1. This action spectrum may be used to express the efficacy of isomerising bilirubin for different wavelengths of radiation.

2.5.2 Penetration depth

The penetration depth is an important parameter for radiative transfer in biological tissue. The penetration depth δ is defined as the depth where the fluence has been reduced to $1/e$ when far away from the source [139, p.344]. The penetration depth is derived from the diffusion coefficient D, which is given by [139, p.97]

$$D = \frac{1}{3(\mu_a + \mu_s')}, \tag{2.31}$$

where μ_a is the absorption coefficient and μ_s' is the reduced scattering coefficient. The diffusion coefficient is a proportionality constant which describes the amount of diffusion in

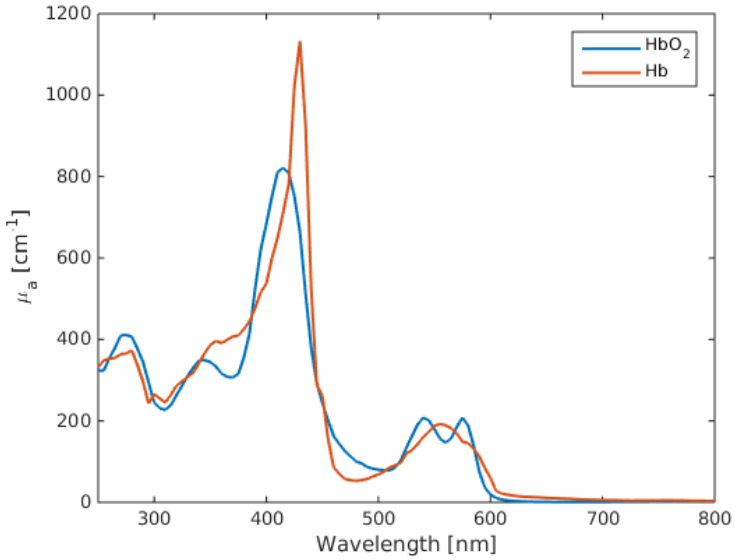

Figure 2.8: Absorption coefficients of hemoglobin, both oxygenated HbO_2 and deoxygenated Hb as a function of wavelength. Figure based on data from [34].

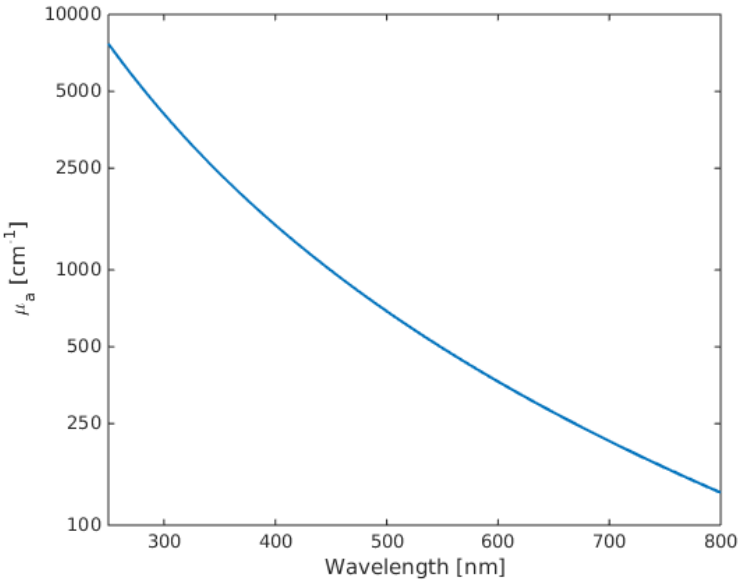

Figure 2.9: Absorption coefficient of melanin in skin as a function of wavelength, with the expression of coefficient given by equation (2.30) *from [54]. Note the logarithmic scale of the yaxis. The wavelength range is limited to the UV and visible wavelength range.*

a medium, given by Fick's law. The effective attenuation coefficient μ_{eff} is the exponential decay rate of fluence far away from the source, and it is given by [139, p.98]

$$\mu_{\text{eff}} = \sqrt{\frac{\mu_a}{D}} = \sqrt{3\mu_a(\mu_a + \mu_s')}. \tag{2.32}$$

The penetration depth is defined as the inverse of the effective attenuation coefficient, which gives

$$\delta = \frac{1}{\mu_{\text{eff}}} = \frac{1}{\sqrt{3\mu_a(\mu_a + \mu_s(1-g))}}. \tag{2.33}$$

The penetration depth is often given in units of cm, and is a measure of how far in the skin the radiation penetrates.

2.5.3 Modelling of radiative transfer in biological tissue

As mentioned, two of the different ways to model photon transport in biological tissue are by the diffusion approximation and by Monte Carlo modelling. The diffusion approximation uses the analytical expression of the radiative transport equation and approximates it by assuming that the radiance in a high-albedo scattering medium is nearly isotropic after sufficient scattering [139, p.88]. A high-albedo medium means that the absorption coefficient is much smaller than the scattering coefficient. The Monte Carlo method is numeric, and models each photon as it propagates through the tissue by random walk [139, p.37]. The results are then based on statistics for a large amount of photons. The method of the diffusion approximation is much more computationally efficient than the numerical Monte Carlo method, but might also less accurate [139, p.83].

For any application of radiative transfer theory on biological tissue, the boundary conditions have to be considered. Without correction of the tissue boundaries in diffusion theory, the errors may exceed 50% [46]. To achieve a correct physical interpretation of boundaries with different refractive indices, the Fresnel reflection coefficient needs to be accounted for [139, p.103]. One such boundary is the boundary between air and skin. The Fresnel reflection coefficient is given by [96]

$$R(\theta_i) = \frac{1}{2}\left[\frac{\sin^2(\theta_i - \theta_t)}{\sin^2(\theta_i + \theta_t)} + \frac{\tan^2(\theta_i - \theta_t)}{\tan^2(\theta_i - \theta_t)}\right], \tag{2.34}$$

where θ_i is the angle of incidence on the boundary and θ_t is the angle of transmission, given by Snell's law as

$$n_i \sin\theta_i = n_t \sin\theta_t. \tag{2.35}$$

Here, n_i is the refractive index of the medium from which the photon is incident and n_t is the refractive index where the photon is transmitted. A type of boundary condition which accounts for equation (2.34) is described by Haskell et al [46], and is a combination of the extrapolated boundary condition and the partial-current boundary condition.

In this thesis, the Monte Carlo method has been chosen for simulation of infant skin. This method will therefore be described further. For information on the diffusion approximation, the reader is referred to chapter 5 of Wang and Wu [139] or to the article by Haskell et al [46].

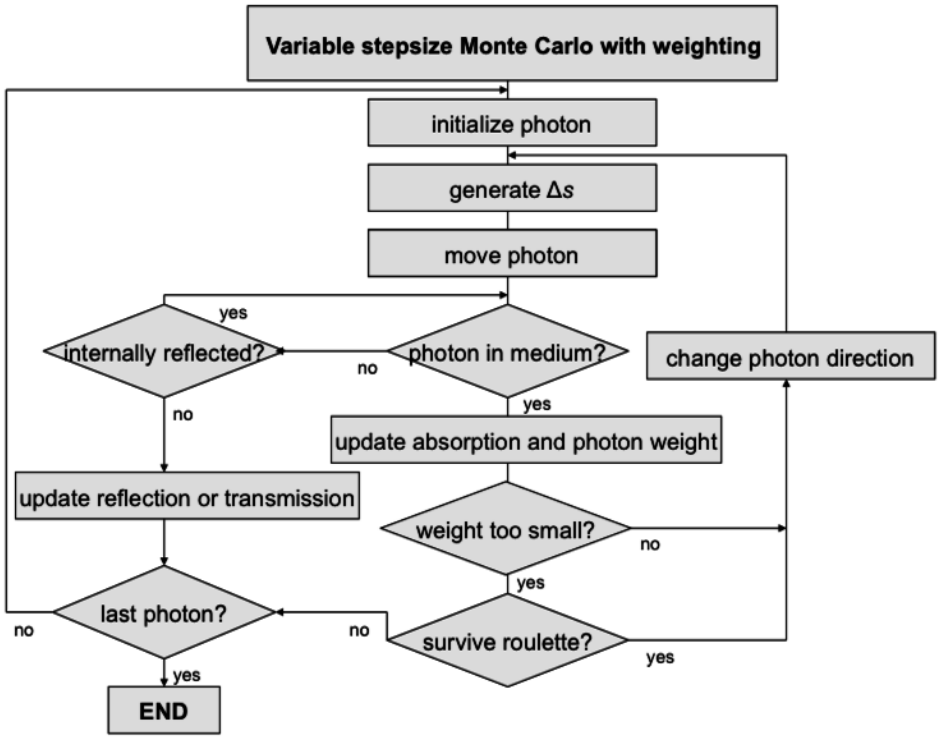

Figure 2.10: Flowchart for the variable step size Monte Carlo technique, based on [96].

2.5.4 Monte Carlo Model of Light Propagation in Tissue

The Monte Carlo method simulates light propagation in tissue by recording photons histories as they are scattered and absorbed [96]. The simulation is based on the random walks that photons make as they travel through tissue, and these random walks are chosen by statistically sampling the probability distributions for step size and angular deflection per scattering event [136]. After recording a large number of propagating photons, the net distribution of all photon paths yields a depiction of reality.

There are several ways to implement Monte Carlo simulations of light transport. One of the most developed and documented ones is the Monte Carlo for Multi-Layered media (MCML). MCML is a steady-state Monte Carlo simulation program for turbid media with an infinitely narrow photon beam as the light source [136]. Each layer of the simulation has its own optical properties of absorption, scattering, anisotropy and refractive index. The program may be easily modified, and is available for download from [136].

The MCML method and the variable stepsize Monte Carlo technique is illustrated by the flow chart of figure 2.10. This flowchart describes the progress of a given photon, which is moved a distance Δs for each iteration. When moved, the photon may be scattered, absorbed, propagated undisturbed, internally reflected or transmitted out of the tissue. The photon is repeatedly moved until it either escapes from, or is absorbed by, the tissue. The different options are briefly described in appendix C.

The process of the MCML program is detailed in chapter 3 of Wang and Wu [139] and further explained by Wang et al in [137] and [138], where the two latter detail the latest summary of the current MCML implementation method. The approach outlined in appendix C taken from Prahl et al [96], which detail the propagation model.

Phototype	Sunburn and tanning history	Immediate pigment darkening	Delayed tanning	Unexposed buttock skin	UVA MED (J/cm^2)	UVB MED (mJ/cm^2)
I	Burns easily, never tans	None	None	Ivory white	$20-35$	$15-30$
II	Burns easily, tans minimally	Weak	Minimal/ weak	White	$30-45$	$25-40$
III	Burns moderately, tans moderately	Definite	Low	White	$40-55$	$30-50$
IV	Burns minimally, tans moderately	Moderate	Moderate	Beige- olive	$50-80$	$40-60$
V	Rarely burns, tans profusely	Intense (brown)	Strong	Moderate brown	$70-100$	$60-90$
VI	Never burns, tans profusely	Intense (dark brown)	Strong	Dark brown/ black	100	$90-150$

Table 2.1: Overview of Fitzpatrick skin phototypes [32], table from [7, 33]. MED denotes the minimal erythema dose. The weighting of the UV radiation has not been specified by the source, and it is therefore assumed an additive weighting for UVA and a weighting with the erythema action spectrum for UVB. This weighting will be dealt with in section 2.7.1. The units are as given by the sources, and not in SI units.

2.6 Skin types

When assessing the biological effect of radiation on skin, the skin type is of great importance. Skin type was first introduced by Fitzpatrick in 1975 [32]. The different skin phototypes are based on listening to the patient's own report of skin responses after a previously defined significant sun exposure. The six different skin phototypes can be seen in table 2.1.

Different skin phototypes are related to different behaviour in response to exposure to sunlight. As can be seen in table 2.1, the different phototypes correspond to different skin colour. Another difference is found in the UV radiant exposure needed to produce erythema in the skin. Erythema is the reddening of the skin associated with sunburn [55]. The UV radiant exposure needed to produce erythema is defined as the minimal erythemal dose (MED) [127]. The MED is a limit for the occurrence of damaging sunburn, and is the radiant exposure that will produce a just-perceptible erythema reaction $8-12$ hours after the exposure [127] of previously untanned skin. The MED for UVA radiation is about 1000 times larger than the MED for UVB radiation [112], which is evident in table 2.1. From this table it may also be seen that the MED is highly variable within different skin types. There has been shown statistical significant variations in the MED as a function of age, gender and hair colour in addition to skin type [33]. The MED is not directly comparable for different skin types or ethnicities, and cannot be used for general public

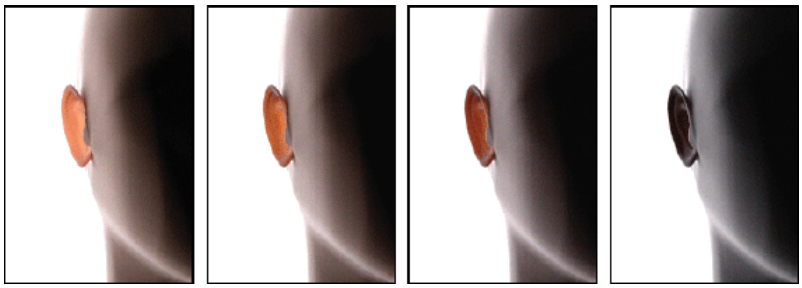

Figure 2.11: Images illustrating different amounts of epidermal melanin using the BioSpec model for skin spectral simulation. Image copied with permission from [62].

advice in diverse populations.

The standard erythema dose (SED) is a quantification of the ability of a radiation source to produce erythema. The SED is equivalent to an erythemally effective radiant exposure of $100\,\mathrm{J/m^2}$ [25, 127]. The SED might be used to compare different cases of radiant exposure from UV radiation. The MED for the skin types I to IV is expected to lie between 1.5 SED and 6 SED [25], which corresponds to the UVB MED values in table 2.1.

Both the MED and the SED are calculated from erythemally weighted irradiance. The erythema action spectrum is presented in section 2.7.1.

2.6.1 Determination of changing optical parameters for the skin types

The skin phototypes are extremely subjective, as the skin is characterized by subjective evaluations of response to sunlight. The behaviour of skin responses such as penetration depth and radiative transfer are dictated by the optical parameters of the skin. Such optical parameters are related to specific optical chromophores, such as melanin, hemoglobin, bilirubin and carotenoids [89]. Skin types and the response of skin when exposed to radiation depend on several other factors as well, for instance previous exposure to radiation. Pigmentation and skin types are not equal or interchangeable, and the definitions must be kept separate. The skin types have not been described in terms of optical parameters to this date. However, in this thesis, a set of optical parameters, specifically the melanin pigmentation, are assigned to the different skin types. This adjustment to the skin types is used throughout this thesis.

Skin response to short wavelength radiation, for instance UV radiation, is dependent of the amount of melanin in the epidermis. The melanin absorption coefficient μ_a^m is shown in figure 2.9, and this figure shows how the melanin absorption coefficient decreases for increasing wavelengths. The melanin content of the epidermis is highly dependent on hereditary skin type and pigmentation, and might be considered one of the defining characteristics of each skin type. An illustration of different skin types as a function of changing levels of melanin pigmentation may be seen in figure 2.11.

There are several methods to determine the amount of melanin absorption in the epidermis. Both Svaasand et al [123] and Norvang et al [89] used analytical models derived from the diffusion approximation for the determination of the melanin absorption coefficient μ_a^m in different skin types, which was later compared to actual measurements. These results will be used in this thesis.

Skin type	Melanin absorption coefficient μ_a^m at $694\,\mathrm{nm}$
II	$200\,\mathrm{m}^{-1}$
IV	$900\,\mathrm{m}^{-1}$
V	$1500\,\mathrm{m}^{-1}$
VI	$2500\,\mathrm{m}^{-1}$

Table 2.2: Table of skin type and the associated melanin absorption coefficient μ_a^m, based on data from Norvang et al [89] and Svaasand et al [123].

There are some agreement between the melanin absorption of skin and the skin type. However, due to the definition of the Fitzpatrick phototypes, this agreement is not unambiguous. Norvang et al used classifications of skin type based on ethnicity, rather than the Fitzpatrick classification. The skin types were African, Asian, Persian Caucasian, North European Caucasian and Scandinavian Caucasian [89]. The resulting optical parameters fitted reasonably with earlier findings, including the melanin absorption coefficients. However, an important result from this study was that the individual differences are extremely large. Measurements on skin optical parameters may have high variability dependent on body location, blood pressure, age, and sun tan. This variability is also reported by Jaqcues when discussing the optical absorption of melanin [54]. He states that the volume fraction of melanin in the epidermis may change with $1-3\%$ for fair Caucasians, $11-16\%$ for well-tanned Caucasians and Mediterraneans, and $18-43\%$ for darkly pigmented Africans.

For this thesis, the Fitzpatrick skin phototypes have been chosen as a basis for comparison, with the addition of a melanin absorption in epidermis based on the results form Norvang et al [89] and Svaasand et al [123]. The melanin absorption coefficients chosen for the relevant skin types may be seen in table 2.2. The values in this table are given for wavelengths of $\lambda = 694\,\mathrm{nm}$, and may be defined for any other wavelength by changing equation (2.30) to

$$\mu_a^m(\lambda) = \mu_a^m(694\,\mathrm{nm}) \cdot \left(\frac{694\,\mathrm{nm}}{\lambda}\right)^{3.48}. \tag{2.36}$$

This approach results the melanin absorption coefficients based on actual measurements.

2.6.2 Infant skin

Infant skin is markedly different from adult skin. It depends largely on gestation age and will continue to develop after birth [99]. However, very little research has been conducted to determine this difference and few studies have followed the development of infant skin over time [27, 69].

One of the differences is the level of melanin in the epidermis. Most infants are born relatively light skinned [110], and darken over time [114] due to both hereditary pattern and sun exposure [99]. The age at which skin adaptation to solar UV radiation becomes perceptible, which is due mainly to melanin, has not been defined as of 2010 [69]. When treating infants for neonatal jaundice, the skin type of the infant is determined by the skin type of the mother. This determination means that several infants are classified as skin type VI, or black Africans as is the case for Slusher et at in [113]. However, it is stated that the skin colour of these infants vary significantly, especially at birth. According to Norvang et al, skin type may also be misleading when the skin has not been exposed to the

sun [89], which is the case for newborn infants. It may be discussed whether any infant can be determined as a skin type of V or VI, or based solely on the skin type of the mother, but this will not be discussed further in this thesis.

Caucasian infants often have a reddish appearance, which is due to less connective tissue than in adult skin and little subcutaneous fat [99]. Younger children will also have thinner, less elastic and more delicate skin than adults [99, 110]. According to Randeberg et al [99], the reflectance of the skin increases rapidly after birth. For a wavelength of 490 nm, the reflectance increases significantly in the first four years of age. This increase of reflectance is caused by maturation of the collagen fibers in the skin combined with a build-up of a thicker subcutaneous fat layer [99]. Infants are thought to be unusually vulnerable to UV radiation, due to the lower levels of protective melanin, the thinner epidermis and the higher surface area and body mass ratio [94, 110].

It has not been possible to uniquely determine the structure of infant skin, as it varies with several parameters. However, it may be assumed that the structure can be approximated to the structure of adult skin, only thinner. Optical parameters are in this thesis considered similar to those of adult skin, except for the scattering coefficients which have been classified uniquely as a function of gestation maturity (GM), measured in weeks. This gestation maturity is the age of the infant in weeks spent both in the womb and after birth.

According to Saidi et al [108], the scattering coefficient in infant skin is a combination of Rayleigh scattering and Mie scattering. Mie scattering is mainly due to the collagen fibers in the skin, and the Rayleigh scattering is due to small tissue structures. The fraction of scattering due to Mie scattering increases as a function of GM, and for term infants this fraction is about 90%, which is similar to adult skin. For infants below 40 weeks of GM, the fraction of Mie scattering compared to Rayleigh scattering is less.

The reduced scattering coefficient μ_s' have been determined uniquely as a function of both wavelength and age given in GM, and is given as [108]

$$\begin{aligned}\mu_s' &= \mu_s'(\text{Mie}) + \mu_s'(\text{Rayleigh}) \\ &= A\left[1 - (1.745 \cdot 10^{-3})\lambda + (9.8453 \cdot 10^{-7})\lambda^2\right] + B\lambda^{-4},\end{aligned} \tag{2.37}$$

where A is the Mie scattering parameter and B is the Rayleigh scattering parameter. Both A and B increase linearly with increasing GM.

2.7 Risk factors of radiation

There are several risk factors related to radiation exposure. These risks occur mainly from the exposure of UV radiation, although visible radiation and IR radiation may also contribute.

The most relevant harmful acute effect of UV radiation is erythema, or sunburn. The difference between erythema and sunburn is that erythema is a slight reddening of the skin which peaks after 24 hours after exposure, while more severe sunburn includes blistering and ulceration. The development of erythema may be seen in figure 2.12. Erythema is an acute reaction, and the development of skin cancer is linked to episodes of sunburn and the associated DNA damage [126]. Erythema can be induced by UVA radiation alone at high radiant exposures of around $50\,\text{J/cm}^2$ in individuals of skin type II-III [112]. This immediate erythema lasted for 24 hours, while erythema produced by the threshold value of $13\,\text{J/cm}^2$ faded within minutes. These doses agree with the values of UVA induced MED

Figure 2.12: Images illustrating the development of erythema using the BioSpec model for skin spectral simulation. Image copied with permission from [62].

in table 2.1. Erythema might even be produced by visible light, especially in dark-skinned subjects [112]. However, UVB radiation is the most effective in producing erythema.

Chronic effects of UV radiation are the development of skin cancer, especially of cutaneous melanoma (CM), and permanent damage to the eyes [126]. Compelling evidence links excessive sun exposure in early childhood to skin cancer later in life [94]. Eye damage may also be induced by visible light in addition to UV radiation, specifically in the blue wavelength range [128]. Other types of skin cancer, basal cell carcinoma (BCC) and squamous cell carcinoma (SCC), may also be a consequence of exposure to UV radiation. According to Lucas et al [67], solar exposure is the major environmental risk factor for all three types of skin cancer in fair skin types, where SCC depends on the cumulative sun exposure, BCC depends on intermittent exposure to UV radiation especially in childhood and adolescence, and CM is related to episodes of sunburn from childhood onwards.

The incidence of different types of cancer change with ethnicity, and for skin type VI, the most frequent type of cancer on the African continent is CM. For the fair-skinned population of South Africa and the population with Arab ancestry in Egypt, i.e. skin types II to IV, on the other hand, CM is the least frequent type of skin cancer. For these lighter populations, the most frequent type of cancer is BCC [67]. However, the highest incidence of all cancers still occurred for the population of light skin types.

IR radiation has harmful effects which mostly concern hypothermia and hyperthermia, which means large changes in body temperature. However, also IR radiation may cause damage to the eyes.

2.7.1 Biological action spectra for beneficial and adverse effects

To determine biological effects of the incoming solar irradiation, the beneficial effects as well as the adverse effects must be taken into account. The effects may be described by an action spectrum which describes the efficacy at each wavelength to cause a specific biological effect. The action spectra included in this thesis are the isomerisation of bilirubin and the development of erythema. When weighting the spectral irradiation spectrum with the action spectrum, the results becomes the effective biological irradiance, given in W/m^2.

The bilirubin action spectrum, denoted $\Gamma_{\text{bil}}(\lambda)$, includes the absorption, the skin penetration and the efficiency of the photons of wavelength λ in isomerising molecules of bilirubin in blood and skin as described in section 1.2. The beneficial effect of the sunlight exposure on the condition can be approximately determined by looking at the bilirubin weighted irradiance. However, the action spectrum for bilirubin has not been uniquely determined.

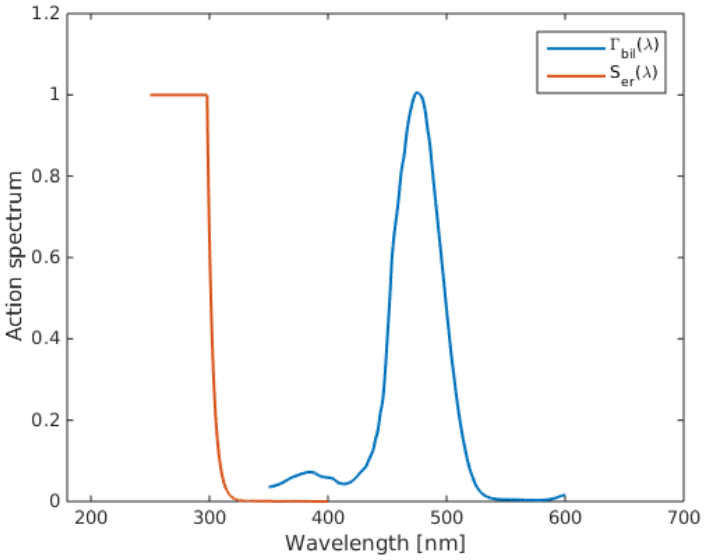

Figure 2.13: Biological weighting action spectra for bilirubin and erythema. The bilirubin action spectrum $\Gamma_{\text{bil}}(\lambda)$ is set equal to the absorption spectrum calculated by Lamola and Russo [64]. The erythema action spectrum $S_{\text{er}}(\lambda)$ is the standard published by CIE and corresponds to equation (2.38) *[25].*

In 2014, Lamola and Russo recorded the fluorescence excitation spectrum of bilirubin in blood, and found this spectrum to be very similar to a calculated absorption spectrum for bilirubin photochemistry in infant skin [64]. This similarity indicates that the calculated absorption spectrum is a fairly good approximation to the desired action spectrum. The action spectrum for bilirubin isomerisation that is used in this thesis is therefore equal to the absorption spectrum from Lamola and Russo [64]. This spectrum is shown in figure 2.13, where it has been normalized to 1.0 at the maximum. The original data from Lamola has a maximum absorption probability of 0.0773 (Lamola, personal communication to Lise Lyngsnes Randeberg).

Earlier action spectra for bilirubin, for instance the one used by Tan in 1983 [125], had a peak absorption around 450 nm. However, recent research has shown that the bilirubin absorption spectrum *in vivo* has a peak around 490 nm [1, 18, 28, 68], corresponding to the peak of the absorption spectrum from Lamola and Russo.

As a comparison to the beneficial effect of bilirubin, the adverse effect of erythema is determined. Erythema is one of more potentially dangerous effects of solar radiation since it has been linked to increased risk of skin cancer at later time. Erythema is assumed in this thesis to be the most relevant adverse effect of sunlight exposure. The biological effect of erythema is calculated by using the erythema action spectrum, $S_{\text{er}}(\lambda)$, where λ denotes the wavelength of the radiation. This action spectrum is standardised by the CIE (Commission Internationale de l'Éclairage) and the International Organization for Standardisation (ISO)

in ISO-standard 17166, and is defined as [25]

$$S_{\text{er}}(\lambda) = \begin{cases} 1, & \text{for } 250 < \lambda \leq 298 \\ 10^{0.094(298-\lambda)}, & \text{for } 298 < \lambda \leq 328 \\ 10^{0.015(140-\lambda)}, & \text{for } 328 < \lambda \leq 400 \\ 0, & \text{otherwise.} \end{cases} \tag{2.38}$$

This standard is an internationally accepted representation of the erythema-inducing effectiveness of wavelengths in the UV part of the spectrum [111, 140]. It also forms the basis of the UV index, which is used for public health information. The erythema action spectrum is displayed together with the bilirubin action spectrum in figure 2.13.

The skin type is not specified for either of the action spectra. It is assumed in this thesis that they are defined mostly for skin type II and III, as these skin types are the most common for Western populations.

2.7.2 Exposure limits

Even though the incoming solar irradiation has both beneficial effects on the concentration of bilirubin and acute adverse effects in the form of erythema, there are other more long term effects that need to be taken into account. In this respect, the International Commission on Non-Ionizing Radiation Protection (ICNIRP) has published several guidelines that outline exposure limits for different kinds of radiation [126–128]. These exposure limits represent conditions under which it is expected that nearly all individuals may be repeatedly exposed without acute effects and without noticeable risk of delayed effects.

It is important to note that the exposure limits detailed by ICNIRP and described in this section are developed for the general public or working population. As such, medical treatment are exempt and may give larger doses than described here. However, the exposure limits are important because they give advice on which medical effects to look out for during different exposures. It is good to keep the limits in mind when deciding the radiant exposure and to keep the radiant exposure within the limits when possible.

Some exposure limits are determined by using a spectral weighting function, which gives an effective irradiance and radiant exposure. The relevant spectral weighting functions are displayed in figure 2.14, as functions of the wavelength λ. $S(\lambda)$ is the UV spectral weighting function [126], $R(\lambda)$ is the retinal thermal hazard spectral weighting function, $A(\lambda)$ is the aphakic hazard spectral weighting function and $B(\lambda)$ is the blue-light hazard spectral weighting function [128]. The difference between $S(\lambda)$ and $S_{er}(\lambda)$ is that $S(\lambda)$ is the spectral weighting function for all adverse effects of UV radiation, while $S_{er}(\lambda)$ is only concerned with the development of erythema. $S_{er}(\lambda)$ is described in equation (2.38) and only deals with wavelengths above 250 nm. $S(\lambda)$ as displayed in figure 2.14 includes wavelengths down to 180 nm.

The effective irradiance for total UV exposure is found by multiplying $S(\lambda)$ with the incoming spectral irradiance. When multiplied with exposure time, the effective irradiance gives the effective radiant exposure to UV radiation. According to the exposure limits, the effective radiant exposure should not exceed $30\,\text{J/m}^2$ [126]. The limit concerns both skin and eyes, and applies for exposures within a time period of 8 hours.

For visible radiation and IR radiation, the ICNIRP guidelines describe 9 different biological effects. These effects are thermal damage to cornea, iris, crystalline lens and

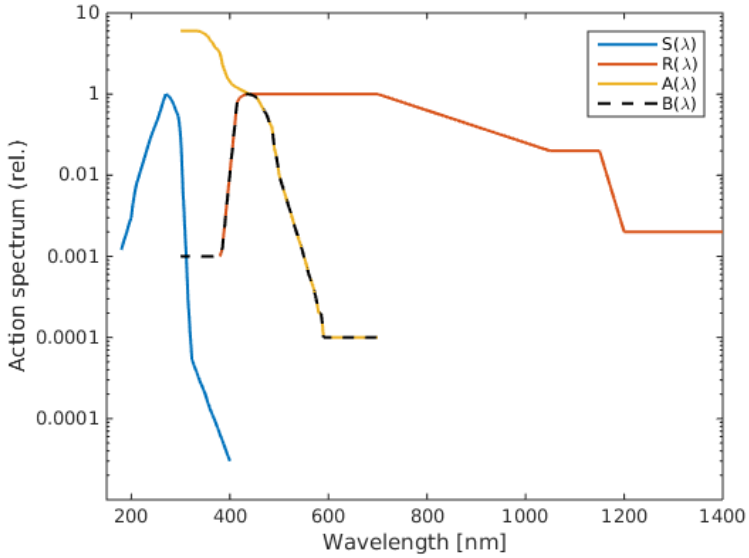

Figure 2.14: Spectral weighting functions, as defined in guidelines from ICNIRP [126, 128] for exposure limits of UV, visible radiation and IR radiation. $S(\lambda)$ is the UV spectral weighting function, $R(\lambda)$ is the retinal thermal hazard spectral weighting function, $A(\lambda)$ is the aphakic hazard spectral weighting function and $B(\lambda)$ is the blue-light hazard spectral weighting function.

retina, blue-light photochemical damage of the retina, photochemical retinal damage from chronic exposure to bright light, thermal damage of skin in the form of burns, damage to the skin from photosensitization and photoallergic reactions [128]. All effects have their own action spectrum. The most relevant exposure limits in this case concern the retinal damage, as the damage to the skin from visible and IR radiation is often avoidable by physically instinctive adverse reactions. It is important to assess the effect of both UV radiation and blue-light retinal damage when investigating outdoors treatment. In contrast to the exposure limits for UV radiation, the limits for retinal damage have not been separated for the general public and professionals.

All spectral weighting functions from retinal damage due to exposure to visible and IR radiation are also displayed in figure 2.14. As for the UV exposure limits, the effective

Spectral weighting function	Wavelength range [nm]	Exposure limit	Description
UV, $S(\lambda)$	$180-400$	$30\,\mathrm{J/m^2}$	Within 8 hours, both skin and eyes
Blue-light hazard, $B(\lambda)$	$300-700$	$100\,\mathrm{J/m^2}$	Exposures of $0.25-100$ s
Aphakic hazard, $A(\lambda)$	$300-700$	$100\,\mathrm{J/m^2}$	Exposures of $0.25-100$ s
Retinal thermal hazard, $R(\lambda)$	$380-1\,400$	$1\,\mathrm{W/m^2}$	Exposures of $100\,\mathrm{s}-8\,\mathrm{h}$

Table 2.3: Collection of the exposure limits as defined by ICNIRP for the UV spectral weighting function [126], the blue-light hazard spectral weighting function [128], the aphakic hazard spectral weighting function [128] and the retinal thermal hazard spectral weighting function [128].

irradiance is found by spectrally weighting the incoming irradiance with the spectral weighting functions for each wavelength λ. These spectral weighting functions are $R(\lambda)$ for thermal retinal damage and $B(\lambda)$ for blue-light photochemical retinal hazard. As can be seen from figure 2.14, the relevant wavelengths are from 380 nm, and the spectral weighting functions follows each other for short wavelengths.

However, for children below 2 years of age, the spectral weighting function for blue-light photochemical retinal damage should be replaced with another spectral weighting function. In young children, the lens transmits more UV radiation than the adult lens, and the aphakic hazard function should be applied instead. This hazard function is denoted by $A(\lambda)$, and has a higher damage effect in the wavelength range $400 - 440$ nm.

The exposure limits for retinal damage caused by exposure to blue light is dependent on the exposure time. For exposures between 0.25 s and 100 s, the limit is an effective radiant exposure of 100 J/m^2. However, for exposures between 100 s and $30\,000$ s (≈ 8 h), the limit is an effective irradiance of 1 W/m^2. If the aim is avoiding adverse effects from the exposure, these limits should not be exceeded. All the exposure limits from ICNIRP have been summarised in table 2.3.

It is important to note that ocular exposure to radiation and blue light is not a necessary part of treatment for neonatal jaundice. Several treatment guidelines mention the importance of shielding the eyes of infants undergoing phototherapy treatment. These guidelines will be described in section 2.8.1. With sufficient ocular shielding possibilities, the exposure limits from ICNIRP concerning retinal damage may be adhered, in contrast to the UV exposure limit when concerning medical treatment and phototherapy.

2.8 Current treatment of neonatal jaundice

In Norway, approximately $4 - 8\%$ of infants undergo phototherapy for treatment of neonatal jaundice [70, 132]. Exchange blood transfusion (ET) is the last option when treating neonatal jaundice, and is not used unless the infant is in immediate danger of kernicterus. Phototherapy consists of irradiating the infant with wavelengths within the visible range of $400 - 550$ nm, from violet to green. In Norway, the number of cases that require ET treatment of neonatal jaundice is negligible and no infant has been diagnosed with kernicterus since the introduction of new guidelines for treatment in 2006 [16]. Norwegian guidelines for treatment of neonatal jaundice were provided by paediatrician Anders Aune from St. Olavs Hospital.

To diagnose neonatal jaundice, the main tool is a blood sample analysed for the total serum bilirubin concentration (TsB), which is the amount of bilirubin molecules present in the blood measured in unit µmol/L. This analysis is often taken after a preliminary test, called transcutaneous bilirubinometry (TcB). TcB tests the reflective properties of the skin and measures the degree of yellowing. It has been shown that TcB and TsB correlates relatively well before start of phototherapy [68]. However, TcB is less effective when the skin is highly pigmented and in the period after administered phototherapy [16, 68]. Phototherapy by itself has also been shown by Randeberg et al to induce pigmentation with the associated increase of melanin concentration in epidermis [68].

Treatment of neonatal jaundice in Norway is started when results of TsB measurements exceed the limits displayed in figure 2.15. For term infants, the limits are 350 µmol/L for term infants of normal weight after 3 days [90]. Figure 2.15 also details limits for pre-term

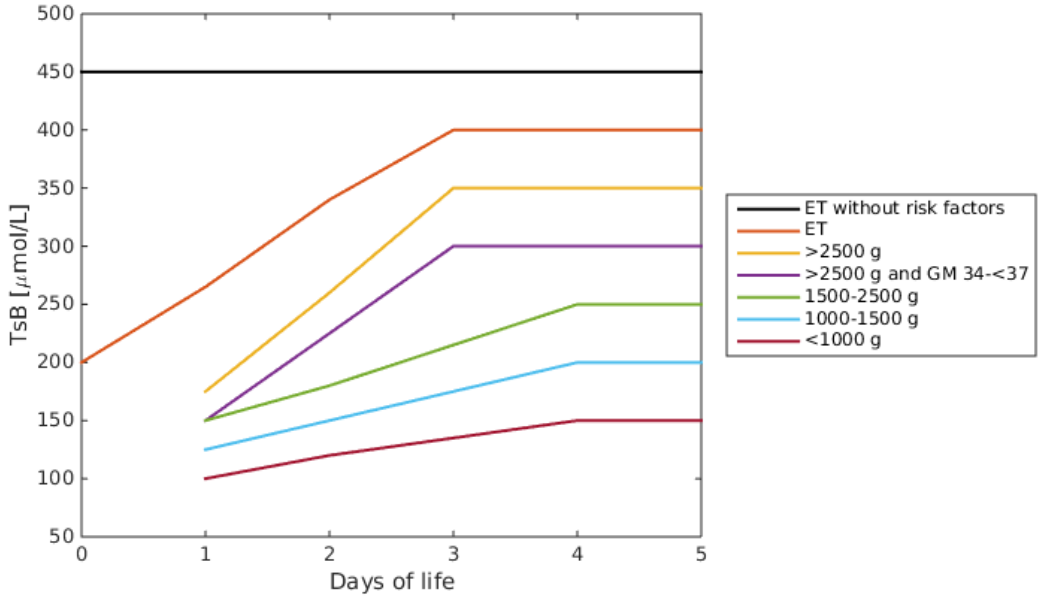

Figure 2.15: Illustration of values from TsB blood measurements which require phototherapy treatment, as a function of age in days and birth weight in g*, including GM measured in weeks for one case. The values in this figure are based on the Norwegian guidelines from [90], described in [16]. ET denotes exchange blood transfusion, and risk factors are for instance haemolysis.*

infants classified by birth weight, and states the values where the treatment should be upgraded from phototherapy to exchange blood transfusion. No infants are checked for neonatal jaundice before the first day of life unless risk factors are present.

A typical conventional phototherapy unit is shown in figure 2.16. The picture shows an overhead unit in use at the St. Olavs Hospital in Trondheim, Norway. Other phototherapy units may irradiate the infant from beneath. The routines that are used at the St. Olavs Hospital in Trondheim might be assumed to be in accordance with the national guidelines in Norway [85, 90], and are assumed to be representative for the treatment in the rest of the country as well.

The recommended routines consist of placing the infant on its back in the phototherapy unit with all skin exposed, except for the eyes and the area beneath the diaper. The overhead light source is placed about 25 cm above the infant, and the unit is covered in reflective white fabric. One course of treatment lasts 24 hours, and the infant spends most of this timespan in the phototherapy unit. The treatment may be interrupted for feeding according to the feeding regime of the infant, which is often every 3 hours. For one course of treatment, the infant spends 24 hours in the unit excluding breaks. After completed phototherapy, new blood samples should be taken after $6 - 24$ hours [16, 85, 90].

Radiation treatment like phototherapy may cause potential damage. To minimise these risks, the exposure limits from ICNIRP [126–128] should be followed when possible. These exposure limits are detailed in section 2.7.2. It is however important to note that the ICNIRP exposure limits are meant for the general public, and may be disregarded when it comes to medical treatment. The International Electrotechnical Commission (IEC) published standards specifically applying to phototherapy equipment in 2009 [52], and it

Figure 2.16: Illustration of treatment of neonatal jaundice with a conventional overhead phototherapy unit, taken at St. Olavs Hospital in Trondheim at the 4^{th} *of September 2015 by the author.*

is mandatory to follow these standards in Norway [24]. The IEC exposure limits state that the UV radiation within the wavelength range $180 - 400$ nm must be below 10^{-5} mW/cm^2, and that the IR radiation within the wavelength range $760 - 1400$ nm must be below 10 mW/cm^2. It is also stated as important that an infant undergoing treatment always wears shielding over its eyes to avoid photo damage from blue light.

2.8.1 Comparisons of guidelines used for treatment of neonatal jaundice

Guidelines for treatment of neonatal jaundice are often determined on a national level, and a collection of different national and international guidelines have been used as a basis for this section. The included guidelines are presented in appendix D. The guidelines were found mostly in reviews by Olusanya et al [92] and Bratlid et al [16].

In most of the guidelines, all aspects of treatment of neonatal jaundice are addressed. These aspects include the serum bilirubin concentration that indicates treatment, procedures of the different treatments and procedures for follow-up after discharge. In this thesis, the irradiance, wavelength range and radiant exposure are most relevant.

Of the guidelines assessed, the guideline published by the American Academy of Pediatrics (AAP) in 2011 [12] is one of the most complete, in that it describes the treatment process with the most details. The recommendations from the AAP is to use what they define as intensive phototherapy, which is spectral irradiances of $\geq 30\,\mu$W/cm^2/nm within the wavelength range of $430 - 490$ nm. These recommendations, with slight amendments, are found in nine out of 18 guidelines for irradiance and five out of 18 guidelines for wavelength range. The rest of the guidelines do not explicitly state neither the wavelength range nor optimal values of spectral irradiance. When it comes to treating neonatal jaundice with sunlight, only four out of 18 guidelines mention this option. Of the four, three are explicitly advising against sunlight exposure while Ghana advises a use of phototherapeutic sunlight for brief periods during mid-morning. The number of guidelines that mentions

National Standards		Mentions irradiance		**Total**
		Yes	No	
Mentions spectrum	Yes	7	1	8
	No	3	7	10
Total		10	8	**18**

Table 2.4: The amount of assessed national and international guidelines that mentions optimal irradiance and wavelength range for treatment of neonatal jaundice by phototherapy.

irradiance or wavelength range can be seen in table 2.4. The differences in the guidelines might be due to a weak evidence base [16, 22, 42].

None of the investigated guidelines advices on the radiant exposure. Some of the guidelines mention the total exposure time, for instance a recommendation for 24 hours of treatment in Norway, but the amount of continuous treatment or pauses are not mentioned. As neither the total irradiance nor the end-point exposure time are given, the recommended radiant exposure is not able to calculate.

2.8.2 Spectral characteristics of phototherapy units

Concerning recommendations for irradiance of phototherapy, most guidelines recommend only a spectral irradiance. However, even though recommended spectral irradiance is advised in several guidelines, this information does not give sufficient information. Measured spectral irradiances of unit μW/cm^2/nm are dependent on both the wavelength range of the radiation source and the spectral response and effect of the detector. It follows that when both lamp and detector is unknown, a measured spectral irradiance given in μW/cm^2/nm cannot be compared to another phototherapy unit [18]. A better comparison would be irradiance, or total irradiance, which is given in W/m^2 or mW/cm^2. All measurements of irradiance or spectral irradiance from phototherapy units should be given in total irradiance. Two phototherapy units which both show sufficient spectral irradiance according to the guidelines, may give different values of total irradiance.

In a study published in 1992 by Christensen et al [22], the results were presented in total irradiance. This study tested a total of 57 phototherapy units in use at that time in Norwegian hospitals. The measurements varied greatly from values below $0.5\,$mW/cm^2 to values at almost $5\,$mW/cm^2, measured with a broad spectrum detector of wavelength range $400 - 700\,$nm. A study published by Tan in 1982 [125] showed that an increase in total irradiation from $0.5\,$mW/cm^2 to $2\,$mW/cm^2 gave twice the effect of reducing the bilirubin concentration in the infants, while a further increase had little or no effect. It may be concluded from Tan's observations that all phototherapy units should have a total irradiance of at least $1.5 - 2\,$mW/cm^2 to provide adequate treatment. Christensen et al found a total irradiance of $\geq 2\,$mW/cm^2 in only nine out of 57 measured phototherapy units in Norway [22]. It is worth mentioning that a follow-up investigation in 2002 showed considerably higher irradiances (Christensen et al, unpublished).

2.8.3 Limitations in low-income countries

One of the challenges of phototherapy in some regions is intermittent access to electricity [91, 116], which disables the operation of electricity-driven phototherapy units. Such phototherapy units are also expensive, and the effectiveness of the devices may be compromised by inadequate skin exposure in cases where several infants are placed under a single device as well as poor device maintenance and sub-optimal irradiance levels [92]. For instance, in a study performed in Nigeria, none of the phototherapy units in 12 referral nurseries provided what the AAP [12] defines as intensive phototherapy, and only 6% of the 63 investigated devices provided spectral irradiances of above $10\,\mu W/cm^2/nm$ [116].

Some low- and middle-income countries may also lack guidelines for treatment, even where the phototherapy units are available [92]. This lack is substantiated by the substantial diversity of the investigated treatment guidelines in appendix D. Such a lack of guidelines might lead to a variety of advice and recommendations from medical professionals [93]. Some medical professionals may give the wrong diagnosis or treatment plan, and there are reported an excessive use of ET in low-income countries [91]. This overuse might be caused by disagreements concerning the severity of the neonatal jaundice of an infant due to e.g. lack of diagnostic tools. It could also be caused by a focus on ET in the treatment guidelines, as seen by Ghana [75]. In low-income countries, a particular challenge is also the discovery and diagnosis of the condition in the infant [31, 93].

In 2015, a protocol for treatment of neonatal jaundice in low- and middle-income countries was published by Olusanya et al [92]. This protocol introduces 4 major points for improving care of the jaundiced neonates, which are primary prevention, early detection and monitoring, treatment and follow-up. The protocol also includes an algorithm for the treatment of neonatal jaundice, with specifications of the recommended type of phototherapy and limits for both phototherapy treatment and ET treatment. The administered phototherapy may either be conventional or intensive, which corresponds to the specifications of the AAP [12, 92].

Chapter 3

Methods

3.1 Measurements of spectrum and delivered irradiance of phototherapy units

To determine the effect of conventional phototherapy units used in high-income countries, two typical phototherapy units in use at St. Olavs Hospital in Trondheim were investigated. Both the spectrum and the irradiance was measured for different configurations. The spectrum was measured with a USB4000 spectrometer (S/N USB4C03284, Ocean Optics, Inc., 830 Douglas Avenue Dunedin, FL 34698 United States), with a UV+VIS fiberoptic cable, also from Ocean Optics. Both spectrometer and fiberoptic cable were from NTNU. The software *Spectral suite* was used to manage the spectrometer during measurements. The irradiance was measured with a PMA2100 radiometer (S/N 6679, Solar Light, 100 East Glenside Avenue, Glenside, PA 19038, USA) [117], which was borrowed from the Norwegian Radiation Protection Authority (NRPA) and Lill Tove Norvang Nilsen. The radiometer used three probes, which were the PMA2121 Blue light safety detector probe (S/N 2894) [118], the PMA2110 UVA probe (S/N 6393) and the PMA2101 UVB erythema weighted probe (S/N 4152). Values from the radiometer were recorded manually. The measurements were conducted at St. Olavs Hospital during the 15th of March 2016, together with fellow master student Adrian Sjøholt.

Two phototherapy units were investigated in this thesis, a Medela 038.0111 overhead unit and a BiliBed mattress (Medela Inc. Healthcare U.S., 1101 Corporate Drive, McHenry, IL 60050, USA). Both units were investigated with respect to spectrum and irradiance. The overhead unit is used above the infant, and aims to bathe the infant with radiation from above. The BiliBed is designed as a mattress for the infant to lie on, which irradiates from below. As the hospital uses a white reflective curtain around the unit during treatment, such a curtain was included in the measurements.

Both of the measured phototherapy units used Osram Ralutec Long 18W/71 [98] as fluorescent light source. These phototherapy units are typical for treatment of neonatal jaundice at St. Olavs Hospital, and are two of the three types of phototherapy units in use throughout the hospital. The last type of phototherapy unit is Natus neoBLUE (Håvard Sagvik Børseth, personal communication), which uses LED as radiation source [82]. The Natus neoBLUE has not been included in this thesis. There are 18 phototherapy units available to the hospital.

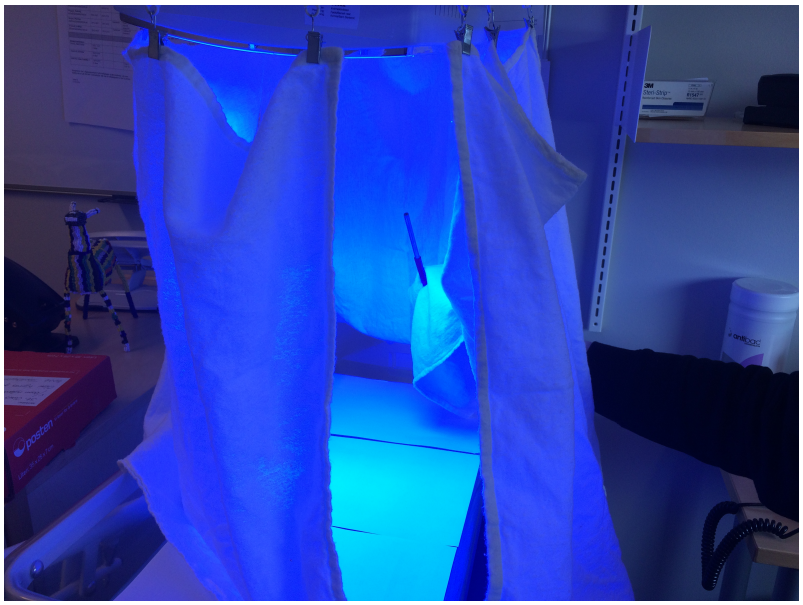

Figure 3.1: Depiction of the set-up for measuring of the spectrum of overhead phototherapy lamp at St. Olavs Hospital in Trondheim. The probe was positioned inside the area protected by curtains, pointed upwards. The curtains were closed during spectral measurements. Photo taken by the author at the 15th of March 2016.

3.1.1 Spectral measurements

The spectra of each of the units were measured separately. In the overhead unit, several fluorescent lamps made up the total light source. These fluorescent lamps could be turned on separately, and were measured both individually and together. The sum of the lamps were measured first, followed by the outermost lamps and then the middle lamps. The number of measurements were 10, 5 and 5, respectively. All measurements were performed surrounded completely by the reflective curtain, and the probe was held by one hand from behind the curtain as shown in figure 3.1 to minimize disturbances from absorption due to the arm inside the protection of the curtains. During measurements of the overhead lamps, reflective white sheets of paper were placed on the BiliBed below to minimize absorption by the mattress underneath.

The BiliBed spectrum was measured similarly, now with the probe pointing downwards at the mattress. The probe was held by the curtains in a similar way as in figure 3.1, and the probe was situated in approximately the same spot. 6 different measurements were performed on the spectrum of the BiliBed phototherapy unit, which has only one setting.

3.1.2 Irradiance measurements

When measuring the irradiance of the phototherapy units, a 3×9 grid on the BiliBed was used to place the measurement probes, laid out as shown in figure 3.2. There were a total of 27 measurement points, with the top edge of the overhead lamp corresponding to the left row of measurement points $1 - 3$. The length of the overhead lamp reached to between measurement points 16 and 19. The measurement points were placed on the mattress with the distances indicated in figure 3.2. The distances were measured with a ruler, and the margin of error is $\pm 0.5\,\text{cm}$. The measurement probes were always placed

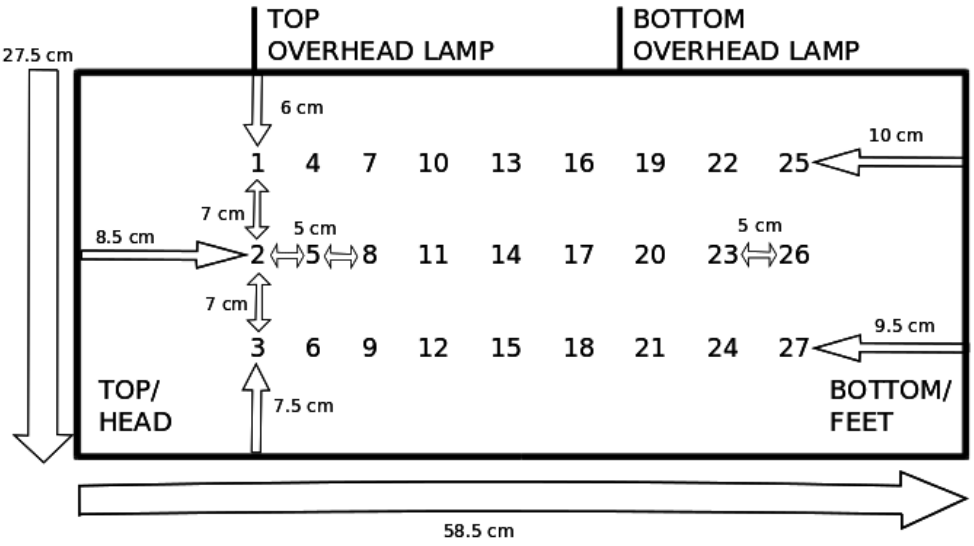

Figure 3.2: Graphical illustration of the measurement set-up for measuring irradiance of the phototherapy equipment at St. Olavs Hospital in Trondheim. The distances connecting the measurement points to the edges of the BiliBed mattress has been specified.

on the measurement points by the same person, to minimize individual variation in the placement. The actual set-up used can be seen in figure 3.3, and the measurement points were marked with small post-its that were completely covered by the probe. The top of the mattress is where the head of the baby would be, and is defined by a white area and logo as visible in figure 3.3.

The Baby Anne (Laerdal Medical, 167 Myers Corners Rd. Wappingers Falls, NY 12590, USA), which was borrowed from the hospital, was used to approximate a typical infant. A depiction of an infant undergoing phototherapy treatment with the investigated units is shown in figure 3.4. This figure shows the correspondence with an infant and the measurement points. By measuring the Baby Anne, the width of an infant measured from upper back to chest is approximated to $10\,\text{cm}$. The measurement probes have a height of $5\,\text{cm}$ [118]. The recommended distance between the overhead light and the infant in Norway thus corresponds to a distance of $30\,\text{cm}$ from the overhead lamps to the BiliBed beneath the measurement probe.

To get realistic values of the irradiance for different treatment schemes, the irradiance was measured for several distances from overhead radiation source to infant. As a distance corresponding to $25\,\text{cm}$ from overhead lamp to the infant is considered optimal, the irradiance was measured for effective distances of $35\,\text{cm}$, $30\,\text{cm}$, $25\,\text{cm}$ and $20\,\text{cm}$ from the overhead unit to the assumed surface of the infant. A distance of $15\,\text{cm}$ was not deemed relevant, as this short distance would deliver irradiance to the infant only from chin to knees. As the aim of phototherapy is to irradiate as much skin as possible, this distance would clearly be insufficient.

For all distances between the mattress and the overhead lamps, the irradiance was measured with all three probes, both with and without the reflective curtains. For the UVB erythema weighted probe, none of the measurements of the irradiance was significantly altered when measuring the phototherapy units compared to the surroundings. They can therefore be assumed neglectible and are not included in the results. The measurements

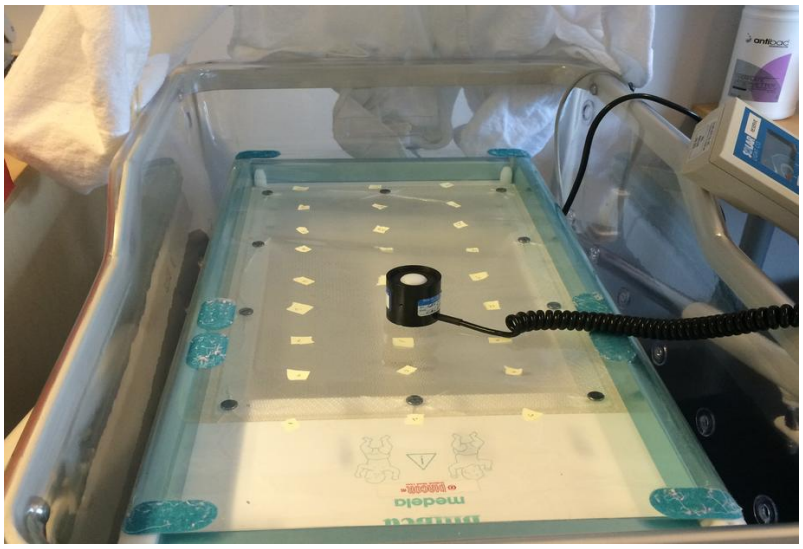

Figure 3.3: Depiction of the actual measurement set-up used to measure irradiance at St. Olavs Hospital in Trondheim, with the probe placed on top of the post-its marking the measurement points. The measurements are in declining order from left to right and front to back. For the irradiance measurements of the BiliBed, the probe was turned upside down, and placed to the immediate right of each measurement point. Photo taken by the author at the 15th of March 2016.

Figure 3.4: Depiction of an infant during phototherapy, approximated with the Baby Anne. The measurement points can be seen on the BiliBed beneath the infant, and covers the area of the baby. Photo taken by the author at the 15th of March 2016.

from the UVA probe when measuring the BiliBed mattress was similarly insignificant.

When measuring the delivered irradiance of the BiliBed, the probes were placed upside down to the immediate right of the measurement points. The diameter of the probes are $4\,\text{cm}$, which means that the measurement points are moved $2\,\text{cm}$ down with respect to the placements illustrated in figure 3.2. As the infant is placed directly on the BiliBed during treatment and the detector is placed near the top of the probe, the only relevant measurement distance was to place the probe directly on the mattress. The reflective curtains were not used when measuring the irradiance from the BiliBed phototherapy unit. For the BiliBed mattress, the values of UVA were indistinguishable from the UVA irradiation of the surroundings.

The probes used for the measurements of the irradiance have a distinct angular response, which for the blue probe is close to the cosine angular dependence of the radiation for angles of less than $60°$. The error for these angles are less than 5% [118]. However, for angles larger than $60°$, the angular response fall quickly until it reaches zero for angles of between $75° - 80°$.

All irradiance measurements were recorded manually. Typical measured values for the Blue light safety detector were of the order $1000.0\,\mu\text{W/cm}^2 (1.00\,\text{mW/cm}^2)$, with an error of $\pm 2\,\mu\text{W/cm}^2$. For the UVA probe, typical values were of the order $0.010 - 0.001\,\text{mW/cm}^2$ with an error of $0.003\,\text{mW/cm}^2$.

3.1.3 Treatment procedures at St. Olavs Hospital

To determine whether the practices at St. Olavs Hospital in Trondheim follow the Norwegian guidelines [90] when treating infants with neonatal jaundice, questions were posed to the nurses on call during the visits to the hospital.

Beate Herfjord was the most helpful in uncovering the procedure followed at the neonatal ward, but the questions were not systematic and she had no time for preparation. Her answers may only be used indicatively due to the informality and irreproducibility of the questions she was posed, as well as the lack of preparation time. The interview was also not formalised nor posed to other nurses. The answers only provide a probability of whether the Norwegian guidelines are followed at St. Olavs Hospital.

3.1.4 Calculation of averaged irradiances

For the measured irradiances to be comparable to other phototherapy units, the total irradiance needs to be calculated as described in section 2.8.2. The total irradiance of the phototherapy units investigated in this thesis are found by averaging the measured irradiance over the measurement points.

There are several possible ways of calculating the average total irradiance. The first is to use the numerical average over all the measurement points. The second is to use an average of a collection of measurement points, for instance the average of the measurement points completely covered by the irradiation source. This average is denoted as a partial average. For the overhead unit, the measurement points directly below the irradiation source are measurement points between $1 - 18$ according to the schematic in figure 3.2. For the BiliBed mattress, the measurement points directly above the irradiation source were the measurement points between $7 - 21$ corresponding to figure 3.2. The third option for calculating averaged total irradiance is to create a weighted average which gives each

Figure 3.5: The set-up of the calibration of the Blue light safety detector probe with the radiometer. The radiation source was situated on the right side of a black partition with an opening, which directed the radiation directly at the center of the probe. The probe was placed $500\,\text{mm}$ *from the radiation source. All distances and planes were measured with lasers.*

measurement point different weights compared to the phototherapeutic efficacy of the irradiation at this point. In this thesis, the total average of the irradiance has been calculated with the first two options, and the main results are chosen as the first option of numerical average over all measurement points.

3.1.5 Calibration and correction factors

The spectrometer was recently calibrated, and the recorded spectra are therefore assumed to be correct within a small range of uncertainty. This assumption may be checked by comparing the wavelengths of the peaks to the known emission spectra of the light sources. Because of this simple check, the calibration of the spectrometer will not be investigated specifically.

The calibration of the radiometer probe of blue hazard light was performed at NRPA by Bjørn Johnsen. No calibration was needed for the UVA or the UVB erythema probe as the results from these probes are not as relevant as the results for the Blue light safety detector probe, whose results may be converted to bilirubin weighted irradiance. The calibration radiation source was a $1000\,\text{W}$ tungsten halogen lamp with a calibration traceable to the World Radiation Calibration centre (WRC, PMOD, Davos). The spectrum of this source can be seen in figure F.1 (appendix F). The calibration was performed with the probe placed as described in figure 3.5. With this set-up, the radiometer showed $291.5 \pm 0.2\,\mu\text{W/cm}^2$.

The calculation of the following calibration and correction factors was performed with an algorithm detailed by Bjørn Johnsen. This algorithm started by weighting the spectrum of the calibration radiation source with the blue light hazard spectral weighting function $B(\lambda)$ [128]. This calculation gave $305.9\,\mu\text{W/cm}^2$. The calibration factor of the Blue light

safety detector probe is given by the measured value divided by the ideal value, which gives

$$C_{probe} = \frac{291.5\,\mu\text{W/cm}^2}{305.3\,\mu\text{W/cm}^2} = 0.95. \tag{3.1}$$

This calibration factor must be used as a weighting to get actual values for all measurements with the blue probe.

The desired result of the irradiance measurements at St. Olavs Hospital was the effect of the phototherapy in reducing the amount of bilirubin in the infants. To acquire these values, a correction factor between the blue light hazard spectral weighting function and the bilirubin action spectrum [64] must be included. This correction factor is found by weighting the normalized spectrum from the overhead phototherapy unit with both the bilirubin action spectrum and the blue light hazard spectral weighting function. The results of this weighting can be seen in figure F.2. The correction factor then becomes

$$C_{corr} = \frac{\Sigma_{bil}}{\Sigma_{blue}} = \frac{163.9}{241.0} = 0.68. \tag{3.2}$$

The total correction factor is given by both the calibration factor and the correction factor to bilirubin. The result becomes

$$C_{tot} = C_{probe} \cdot C_{corr} = 0.65. \tag{3.3}$$

To get correct bilirubin-effective irradiances for the measured phototherapy units at St. Olavs, all measurements with the blue probe must be weighted with this total correction factor.

3.1.6 Conversion to spectral irradiance

The measured spectra of the phototherapy units may be displayed either as a function of counts per wavelength or of spectral irradiance with W/m^2 per wavelength. By using known values of irradiance, a spectrum measured by counts from a spectrometer may be converted to spectral irradiance. This conversion has been performed for the spectrum of the overhead phototherapy unit measured at St. Olavs Hospital with a procedure detailed by Bjørn Johnsen. The measured spectrum in counts from this overhead phototherapy unit can be seen in figure F.3. The spectrum used in the following calculation corresponds to the overhead unit with all lamps switched on.

To achieve a conversion of measured spectra from counts to irradiance, the integral of the spectral irradiance must be compared with a known value of total irradiance. By using a correction value k, the connection between the counts and the levels of irradiance can be found. In this case, the known value of irradiance E was measured at St. Olavs Hospital and converted to bilirubin effective irradiation. This known irradiance is equal to the sum of the bilirubin weighted spectrum of the radiation source when multiplied with k,

$$\sum_{\lambda} N_\lambda \cdot k = C_{tot} E, \tag{3.4}$$

where N_λ is the spectral counts with bilirubin weighting and C_{tot} the correction value from equation (3.3) to convert the measured irradiance to bilirubin weighted irradiance.

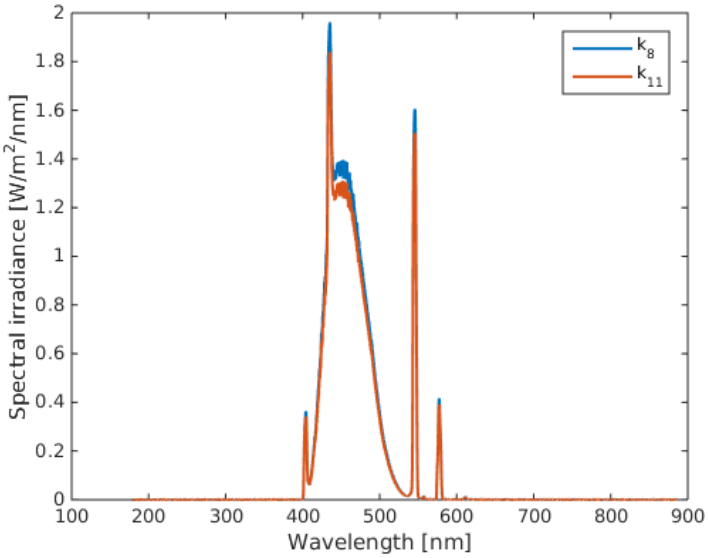

Figure 3.6: The measured spectra of the overhead phototherapy unit at St. Olavs Hospital in Trondheim in terms of spectral irradiance, by using conversion factors from equation (3.5).

The irradiance E was used both from measurement point 8 and 11, as shown in figure 3.2. The measurement series chosen were with a distance of 20 cm between overhead phototherapy unit and infant with reflective curtains. This series and these measurement point were chosen as they represent the nearest approximation of the position of the spectrometer probe when measuring N_λ. The correction factors for the two measurement points are given by

$$\begin{aligned} k_8 &= 4.18 \cdot 10^{-5}, \\ k_{11} &= 3.93 \cdot 10^{-5}, \end{aligned} \tag{3.5}$$

and the resulting phototherapy spectra $N_\lambda k$ of spectral irradiance are presented in figure 3.6. As can be seen from this figure, the spectral irradiance for measurement point 8 is higher in value than the spectral irradiance for measurement point 11. Measurement point 8 is also slightly more centred with respect to the overhead unit. k_8 is therefore used as the correction value to calculate the phototherapy spectrum in spectral irradiance throughout this thesis.

3.2 Atmospheric simulations using *libRadtran*

The incoming solar irradiance was simulated with *libRadtran* for three separate locations. *libRadtran* was installed and used with help from the NRPA. The programs written were based on previous programs from Bjørn Johnsen at the NRPA, and the installation was performed by Dag Robøle.

The selected locations can be seen in table 3.1. Both Dar es Salaam in Tanzania and Kathmandu in Nepal are locations relevant for sunlight treatment of neonatal jaundice, as they have abundant sunlight and are situated in areas of the world where the mortality associated with neonatal jaundice is high. Østerås, situated close to Oslo in the south of

City	Latitude	Longitude	Coordinates	Time zone	Altitude
Dar es Salaam	$6°52'$ S	$39°12'$ E	$(-6.870, +39.200)$	$+3$h	55 m
Kathmandu	$27°43'$ N	$85°19'$ E	$(+27.720, +85.320)$	$+5$h45min	1350 m
Østerås	$59°57'$ N	$10°36'$ E	$(+59.946, +10.598)$	$+1$h	100 m

Table 3.1: Selected locations for simulating solar irradiance. Østerås is the location of the NRPA, close to Oslo, Norway. Dar es Salaam is situated in Tanzania, and Kathmandu is situated in Nepal. Coordinates were taken from satellite data [79], and time zones were found from [131].

Norway, is included mostly to compare the simulations to real irradiance measurements from Østerås and for reference, but also to assess the potential for using sunlight to treat neonatal jaundice in Norway.

To approximate individual weather conditions, satellite overpass data was used. These satellite data were taken from the National Aeronautic and Space Administration (NASA), Goddard Space Flight Center. The satellite measurements originates from the Aura spacecraft [78], and was downloaded from [79] for the selected locations. The location of the satellite overpass data was given by Bjørn Johnsen. Only measurements from 2015 were included in the simulations.

The Aura spacecraft obtains measurements of ozone, aerosols and key gases throughout the atmosphere [78]. In this thesis, the satellite data describing cloud optical depth, level of ozone in the atmosphere and albedo were included to approximate actual atmospheric conditions during simulations. Other data from the satellite overpass were not included, such as levels of aerosols. The included variables were chosen for their importance concerning the atmospheric transmission [107]. The dependence of albedo on solar zenith angle and wavelength has been neglected, and the cloud cover was assumed to be evenly distributed throughout the atmosphere.

Because of the nature of satellite overpasses and the changing orbit, the amount of overpasses each day are highly dependent on location. The number of data points per day of year in 2015 vary from none to three, with a trend of an increasing amount closer to the poles. For Dar es Salaam, 2015 provided a total of $n = 331$ overpasses, which increased to $n = 347$ over Kathmandu and $n = 661$ over Østerås.

Due to the inconsistency of the timing of the overpass, the atmospheric conditions has been approximated as constant during each day. Each set of data points is therefore taken as atmospheric parameters for a whole day, and simulated for each whole hour at each location. The result is that several days are simulated more than once with different atmospheric conditions, and some days are not simulated. However, the results are still representable to actual conditions when viewed as a whole.

The incoming solar irradiation is highly dependent on time of the year. To account for the variations of the seasons as a function of the movement of the sun, the temporal scale has been chosen to fit the solar cycle. This cycle consists of the spring equinox around the 23^{nd} of March, the summer solstice around the 24^{th} of June, the autumn equinox around the 22^{nd} of September and the winter solstice around the 22^{nd} of December. These dates correspond to day 82, 175, 265 and 356 of a year containing 365 days such as 2015. The connection between the dates and days of year can be seen in appendix E. All atmospheric simulations use these days, or days in the immediate vicinity, as comparative times. The actual dates of the solar cycle vary slightly from year to year [53, p.6], which indicates

that the dates of the solar cycle change annually. However, this variation is small. For all results as a function of day of year, the day or date is specified.

For more information about the way the atmospheric parameters are input to the *libRadtran* software package, see section 2.1-2.2 and section 2.4 in [107].

3.2.1 Corrections for real conditions and weighting functions

The atmosphere is highly complex and unpredictable. When dealing with simulations, it is always important to be aware that the results will not mimic real conditions accurately. To investigate the accuracy of the simulations of atmospheric irradiance, simulation results from Østerås has been compared to solar irradiance measurements performed at this location. These irradiance measurements was measured, structured and provided by Bjørn Johnsen at the NRPA.

The irradiance measurements for 2015 were recorded for every minute throughout the year from March 19^{th} until December 31^{st}, and were measured by a GUV-2511 (S/N 25110808136, Biospherical Instruments Inc., 5340 Riley Street San Diego, CA 92, 110-2621 US) [14]. The irradiance has been measured for wavelengths of 305 nm, 313 nm, 320 nm, 340 nm, 380 nm and 443 nm. By investigating the spectral irradiance for the appropriate wavelength, a correction factor for actual irradiance compared to simulated irradiance can be approximated for both bilirubin weighted irradiance and erythema weighted irradiance, corresponding to the biological action spectra described in section 2.7.1. According to figure 2.13, the spectral irradiance at wavelength 443 nm may be approximated to the maximum of the bilirubin weighted irradiance and the spectral irradiance at wavelength 305 nm may be approximated to the maximum of the erythema weighted irradiance. These two wavelengths are therefore used for assessing the correction factors.

Only spectral weightings with the bilirubin action spectrum and the erythema action spectrum are used to compare the incident atmospheric irradiance. However, the adverse effects of the irradiation may also be assessed by using the ICNIRP exposure limits from section 2.7.2 or the MED for the different skin types from table 2.1.

To compare simulated irradiances with measured irradiances as accurately as possible, it is important to have predictable atmospheric conditions. The spectral irradiance which the correction factors are based on should therefore represent clear atmospheric conditions, in other words a cloudless sky. Such conditions were found by searching for a cloud optical depth $\tau = 0$ in the satellite overpass data for Østerås.

For Østerås, there are more sets of data points from the satellite overpass than days of the year, which means that there have been more than one satellite overpass daily. The probability of a measured cloud optical depth of zero representing a truly cloudless day increases when all cloud optical depths of that day equal zero. When this criteria is combined with a desire for the days to be situated in spring or summer due to higher values of incoming irradiance, there are three days which appear suitable. These are March 21^{st}, April 19^{th} and April 21^{st}, corresponding to day number 80, 109 and 111 according to appendix E. The correction factors are based on the simulated and measured solar irradiance at Østerås for these days, and these spectral irradiances are shown in figure 3.7 and figure 3.8. In both figures, the time of day for the simulations have been changed to fit with the measured irradiance. This fit is necessary due to internal differences within each time zone in the movements of the sun, and required subtracting 0.5 h from the time of the simulations.

The correction factors are found by dividing the sum of the measured spectral irradiance by the sum of the average of the simulated spectral irradiances for the same day. The correction factors for actual conditions then become

$$\begin{aligned} C_{bil} &= 0.89, \\ C_{ery} &= 0.81. \end{aligned} \tag{3.6}$$

By scaling all simulation results with these correction factors, the results are more likely to mirror the actual incoming irradiance for any given day.

However, the correction factors are based on measurements performed with a GUV that has been measuring solar irradiance on the roof of the NRPA since 2009, and although the instrument has been checked regularly, there has not been performed a complete calibration since the start of the measurements. The variability of the real-time measurements are therefore both unknown and perhaps as large as 10% (Bjørn Johnsen, personal communication). As C_{bil} reduces the simulated irradiation with 11% and C_{ery} reduces the simulated irradiation with 19%, the corrected simulation results might be within the variability of the GUV performing the real-time measurements. To perform a correction of the simulation results might therefore be misleading.

As can be seen from figures 3.7 and 3.8, the values corresponding to local noon are slightly lower for the measurements than for the simulations. This decrease changes as a function of day and weather. The correction factors are based on the sum of daily irradiance and are therefore not dependent on the timing. However, the weather conditions are apparent in the measurements for even simulated days with three satellite overpass data of clear sky. Due to all these variabilities, the results of the atmospheric simulations displayed in the rest of this thesis are the results of the simulations in *libRadtran* without further corrections. By presenting the uncorrected results of the simulations, the results and discussion will also be reproducible to a larger degree.

3.2.2 Cloud modification factor

An appropriate index to compare weather effects in different parts of the world is the amount of clouds, and the effect of this cloud layer on the incoming irradiation. This index is called the cloud modification factor (CMF). It is calculated by taking the ratio of the incoming irradiance with cloud cover and the incoming irradiance for completely clear conditions. The CMF is always between 0 and 1. If CMF $= 1$, the incoming irradiance is the same for the actual conditions and for completely clear conditions, which means that there are no clouds.

When calculating the CMF, the only instances that have been taken into account is when the sun is above the horizon with the irradiance thus above zero. The CMF is a good measure of the general trend in the weather patterns for a given location, and illustrates how much the incoming irradiance is reduced due to atmospheric factors.

3.2.3 Average days of atmospheric simulations

To determine seasonal variances of solar irradiance, average days for different months may be calculated. These days are based on the simulations of surface solar irradiance for all simulated days situated in the relevant month. The months chosen for the averages are March, June, September and December, which correspond with the solar cycle.

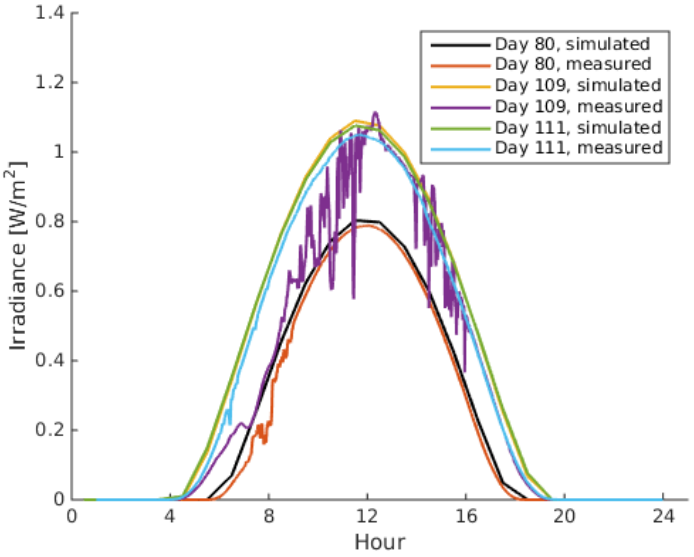

Figure 3.7: Simulated and measured spectral irradiance for wavelength $\lambda = 443\,\mathrm{nm}$ *for days* 80, 109 *and* 111 *(March* 21^{st}*, April* 19^{th} *and April* 21^{st}*). These ratios are the basis of the correction factor* C_{bil}*. The time of day for the simulations have been fit to the measured results.*

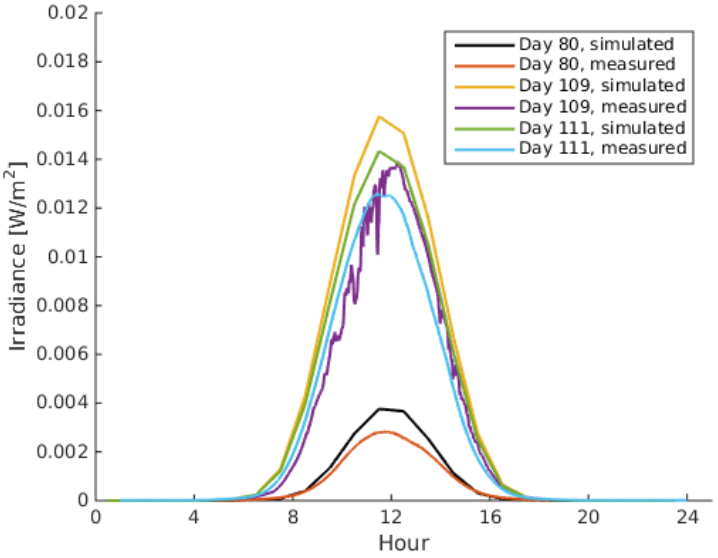

Figure 3.8: Simulated and measured spectral irradiance for wavelength $\lambda = 305\,\mathrm{nm}$ *for days* 80, 109 *and* 111 *(March* 21^{st}*, April* 19^{th} *and April* 21^{st}*). These ratios are the basis of the correction factor* C_{ery}*. The time of day for the simulations have been fit to the measured results.*

The average days are generated by calculating the average irradiance at each time point throughout the day for simulations with observed cloud cover. The time scale was then interpolated to yield irradiance values every 5 minutes. The resulting average days include the cloud cover representative for each month. The averages therefore give information about typical seasonal weather patterns and amount of sunlight, both for level of surface irradiance and sunlight hours. The average days were calculated for all three selected locations.

3.3 Simulations of radiative transfer in different skin types using Monte Carlo simulations

The radiative transfer of infant skin was simulated based on the Monte Carlo Multi-Layered media (MCML) program [136] described in section 2.5.4. The model was developed by Lise Lyngsnes Randeberg and Asgeir Bjørgan at NTNU, and the simulations were run by Asgeir Bjørgan, who provided the results.

The skin types investigated were skin type II, IV, V and VI, with the associated pigmentation as described in table 2.2. Skin type II is assumed to be the reference for treatment guidelines as it is assumed to be the typical skin type for the population of Norway. Skin type IV, V and VI are included due to relevance for the investigated geographical areas, and to investigate the radiant effect in the darkest skin types compared to the reference. The more pigmented skin types are associated with locations with abundant sunlight. These locations are assumed more relevant for sunlight treatment of neonatal jaundice than locations associated less sunlight and thus less skin pigmentation.

The skin is simulated with two layers according to skin parameters as described by Spott et al [119] and Lyngsnes Randeberg et al [68]. The epidermis is simulated with a depth of $80\,\mu$m and an even distribution of melanin. The blood volume fraction is set to 0.2% to correct for the wave-like boundary to the dermis [123], with a blood oxygenation of 60%. The melanin content of the epidermis is described in table 2.2 for the different pigmentations. The dermis is simulated as semi-infinite, with a 5% blood volume fraction and an oxygenation of 80%. The amount of photons for each iteration were $100\,000$, and the simulations were conducted for wavelengths in the range of $400 - 800\,$nm, with separate simulations for every 3 nm.

Input-parameters for the model are the absorption coefficient μ_a, the scattering coefficient μ_s, the scattering anisotropy g, the refractive index n and the depth of the layer d as well as the amount of layers. The absorption coefficient was determined from the absorption of hemoglobin given an oxygen saturation, and the background absorption was set to $25\,\text{mm}^{-1}$. All the melanin was distributed in the epidermis, and the melanin absorption was therefore included in the absorption coefficient for the epidermis. The scattering in both skin layers was set to match the scattering of infant skin of gestation maturity 40 weeks according to Saidi et al [108]. The values for the scattering anisotropy g was taken from [133]. The refractive index was set to 1.4.

The simulations were run for both healthy infant skin and jaundiced infant skin, where $350\,\mu$mol/L bilirubin was evenly distributed throughout the dermis. This bilirubin concentration corresponds to the beginning of phototherapy treatment in healthy term infants according to the Norwegian guidelines [90], as illustrated in figure 2.15.

To determine the amount of photons available to isomerise bilirubin in the skin, it is

important to determine the depth of the bilirubin molecules in the skin. There are still uncertainties about the behaviour of bilirubin in skin, as seen in section 1.2. However, it may be assumed that a great deal of bilirubin is found in the tissue near the blood vessels, as the bilirubin will diffuse to the skin out of the blood stream. According to Svaasand et al, dimensions of blood vessels vary over a range of $10 - 200\,\mu m$ and the vessels are typically located at a depth from the skin surface of $200 - 300\,\mu m$ and deeper [122, 123]. Assuming that infant skin is thinner than adult skin, it may be assumed that bilirubin is found in the skin at distances of $150 - 400\,\mu m$ from the surface.

A depth of $295\,\mu m$ has been chosen as the depth to compare the effects of radiative effect for isomerising bilirubin in the skin. The fluence at this skin depth was simulated for different skin types to investigate the variation due to pigmentation. A depth of $295\,\mu m$ was chosen because this depth is situated between the blood vessels and the skin surface of infant skin, and it is well within the assumed range of bilirubin. Provided that the previous assumptions on infant skin hold, the concentration of bilirubin should be substantial at this distance from the skin surface. A substantial concentration of bilirubin in the skin indicates a large phototherapeutic effect of the present photons.

As the behaviour of bilirubin in infant skin is largely unknown at the current time, healthy infant skin has been used for comparisons. Simulations of skin with $350\,\mu mol/L$ of bilirubin has been included solely to compare the reflectance and fluence as a function of wavelength.

The simulation also calculates the optical properties of the skin tissue for both epidermis and dermis as a function of the input parameters, which depend on wavelength. From the optical parameters of the skin layers, the penetration depth δ may be calculated according to equation (2.33). The penetration depth is thus assessed separately for both the epidermis and the dermis as a function of wavelength.

Chapter 4

Results

4.1 Measurements of phototherapy units

The measured spectrum of the phototherapy units at St. Olavs Hospital has been compared to the bilirubin action spectrum [64] in figure 4.1. The fluorescent peaks are present at 404 nm, 435 nm, 545 nm and 577 nm, and the main peak occurs at the 450 nm wavelength. The spectra were similar in form for both phototherapy units. All spectra are shown in appendix F.

The averaged total irradiances of the phototherapy units are shown in table 4.1 together with the maximal and minimal irradiances measured for the different configurations. The spatial bilirubin weighted irradiance distribution from the overhead phototherapy unit for recommended treatment conditions is shown in figure 4.2, and the spatial bilirubin weighted irradiance distribution from the BiliBed phototherapy mattress is shown in figure 4.3. A comparison of bilirubin weighted irradiances as a function of distance between the overhead phototherapy unit and the infant is shown in figure 4.4. The difference between bilirubin weighted irradiance for the overhead unit with and without reflective curtains is shown in figure 4.5.

All measurement series and results are further detailed in appendix F.

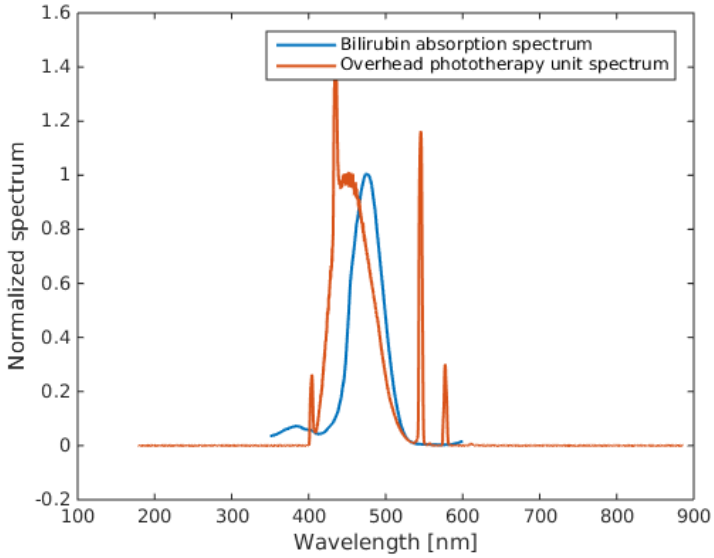

Figure 4.1: Spectrum of phototherapy units for treatment of neonatal jaundice at St. Olavs Hospital in Trondheim compared with the action spectrum of bilirubin [64]. Both graphs have been normalized to 1 *at maximum level, fluorescent peaks excepted.*

Unit	Probe	Curtains	Average [mW/cm^2]	Partial average [mW/cm^2]	Max [mW/cm^2]	Min [mW/cm^2]
Overhead	Blue	Yes	1.04 ± 0.005	1.32 ± 0.005	1.57 ± 0.005	0.28 ± 0.005
Overhead	Blue	No	0.78 ± 0.005	1.01 ± 0.005	1.26 ± 0.005	0.16 ± 0.005
Overhead	UVA	Yes	0.009 ± 0.003	0.012 ± 0.003	0.015 ± 0.003	0.002 ± 0.003
Overhead	UVA	No	0.009 ± 0.003	0.012 ± 0.003	0.015 ± 0.003	0.001 ± 0.003
BiliBed	Blue	No	0.73 ± 0.005	1.15 ± 0.005	1.60 ± 0.005	0.08 ± 0.005

Table 4.1: Irradiance measurements for the phototherapy units in use at St. Olavs Hospital in Trondheim. Results from the blue probe are weighted with C_{tot} from equation (3.3)*. The UVA values have not been weighted. The averages has been calculated according to section 3.1.4. The errors for the blue probe are related to the significant digits.*

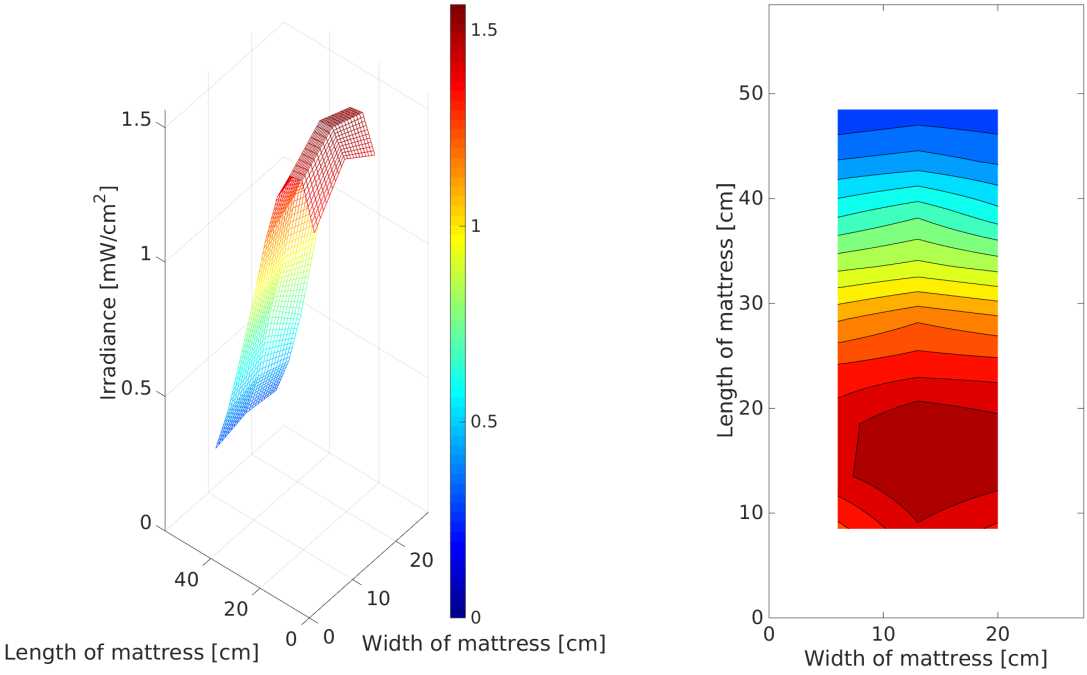

Figure 4.2: Surface plot of measured bilirubin weighted irradiance for overhead phototherapy unit with reflective curtains at St. Olavs Hospital, given in $\mathrm{mW/cm^2}$. *Effective distance between infant and phototherapy unit is* $25\,\mathrm{cm}$.

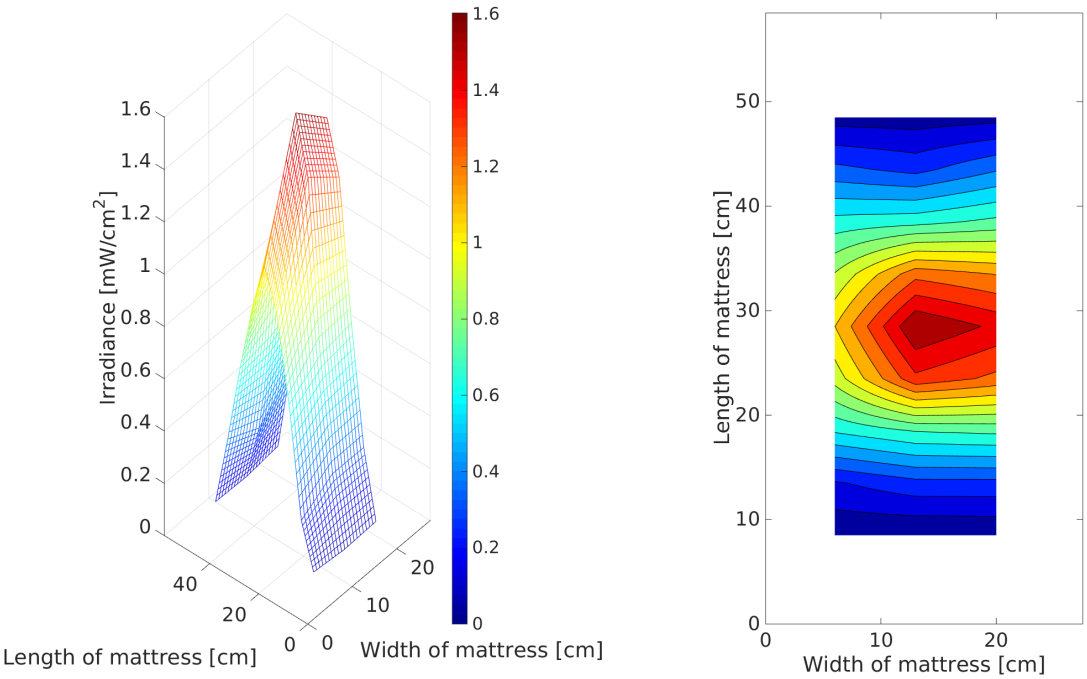

Figure 4.3: Surface plot of measured bilirubin weighted irradiance for the BiliBed phototherapy unit at St. Olavs Hospital, given in $\mathrm{mW/cm^2}$.

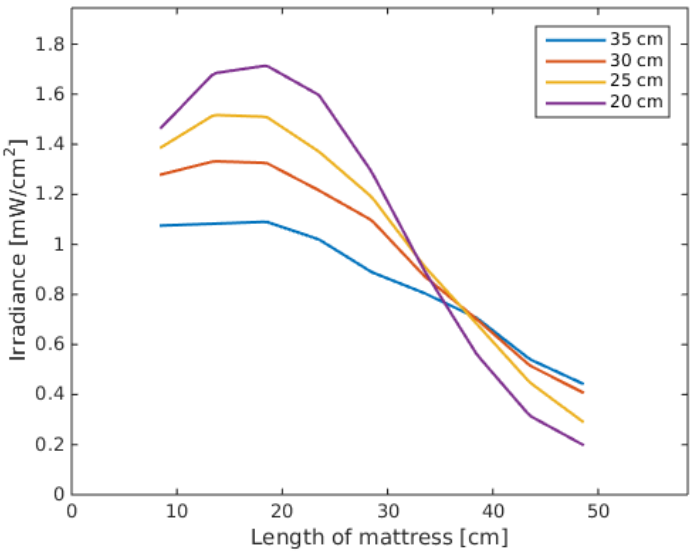

Figure 4.4: Comparison of bilirubin weighted irradiance for overhead phototherapy unit with reflective curtains given in $\mathrm{mW/cm^2}$ *as a function of the effective distance between infant and phototherapy unit.*

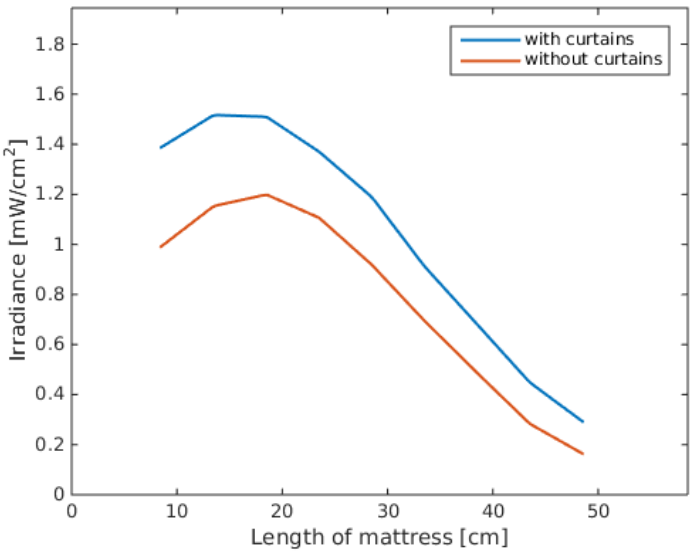

Figure 4.5: Comparison of bilirubin weighted irradiance for overhead phototherapy unit with and without reflective curtains, given in $\mathrm{mW/cm^2}$*. Effective distance between infant and phototherapy unit is* $25\,\mathrm{cm}$*.*

4.2 Practices at St. Olavs Hospital

According to nurses at St. Olavs Hospital, the Norwegian guidelines detailing the limits of bilirubin concentration corresponding to the start of phototherapy treatment, reproduced in figure 2.15, are always followed at St. Olavs Hospital within the uncertainty limits stated by the guidelines. The use of reflective curtains is a part of the standard treatment, and the infants are placed on reflective white sheets during phototherapy with the overhead unit. The number of infants treated at the ward at any given time varied from none to three or four, and there are no statistics on the percentages of infants requiring phototherapy treatment at this hospital.

When treating infants with phototherapy, the overhead unit is used alone for all cases where the infant does not have additional risk factors or conditions, or where the bilirubin concentration is not substantially higher than the treatment limits. The BiliBed mattress is not used routinely, and only as an addition to the overhead unit. When using the overhead phototherapy unit, the distance between the infant and the unit is often as low as possible, to maximize the delivered irradiance.

Regarding the exposure time of the infants, one treatment period at St. Olavs Hospital is always 24 hours although infants might require several treatment periods. The amount of breaks from the treatment are decided by the nurses on staff, and depends on the severity of the neonatal jaundice, the general feeding regime and the need for parental bonding.

4.3 Calculation of adverse effects from conventional phototherapy

The risks associated with erythema and the exposure limits from ICNIRP can be calculated for conventional phototherapy by weighting the phototherapy spectrum in units of spectral irradiance with the relevant spectral weighting functions. This weighting has been performed for the spectra shown in figure 4.6. The spectral weighting functions included in this figure are the erythema action spectrum $S_{er}(\lambda)$, the UV spectral weighting function $S(\lambda)$, the aphakic hazard spectral weighting function $A(\lambda)$ and the retinal thermal hazard spectral weighting function $R(\lambda)$.

To calculate the adverse effects, the radiant exposure must be calculated. The adverse radiant exposures for conventional phototherapy have been calculated with exposure times of both 2.5 hours and 20 hours, which are the longest continuous exposure and the total amount of exposure per phototherapy treatment [90]. The resulting radiant exposures are shown in table 4.2.

Spectral weighting function radiant exposure	Exposure time 2.5 h	Exposure time 20 h
D_{ery}	$105.0\,\mathrm{J/m^2}$	$839.5\,\mathrm{J/m^2}$
D_S	$91.9\,\mathrm{J/m^2}$	$734.8\,\mathrm{J/m^2}$
D_A	$6.19 \cdot 10^5\,\mathrm{J/m^2}$	$5.00 \cdot 10^6\,\mathrm{J/m^2}$
D_R	$8.36 \cdot 10^5\,\mathrm{J/m^2}$	$6.90 \cdot 10^6\,\mathrm{J/m^2}$

Table 4.2: Radiant exposure in J/m^2 *for all spectral weighting functions describing adverse effects of irradiation relevant for phototherapy treatment.*

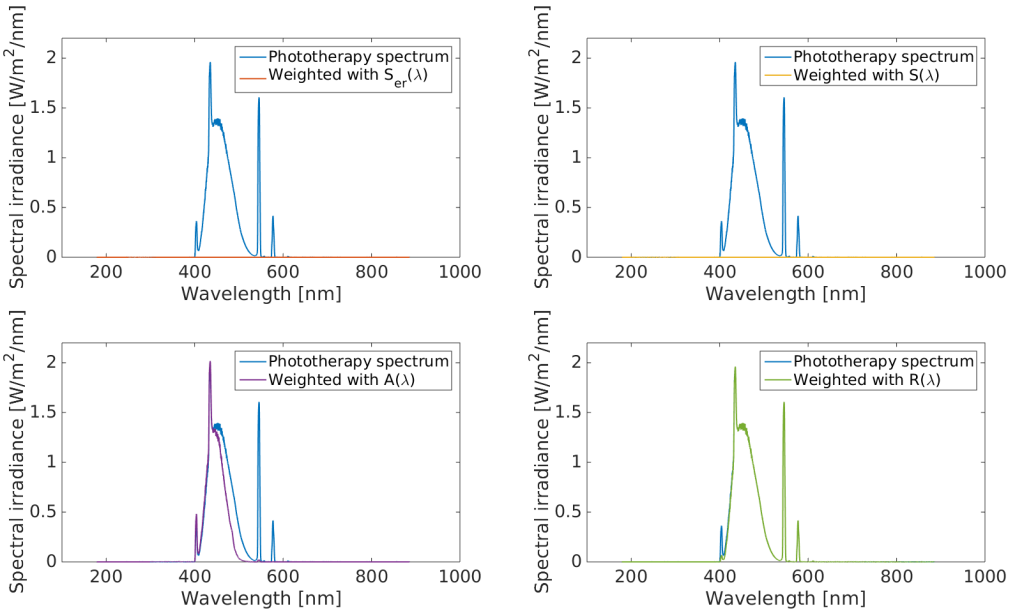

Figure 4.6: The different adverse effects of the irradiation of an infant undergoing phototherapy treatment with an overhead phototherapy unit. $S_{er}(\lambda)$ is the erythema action spectrum [25], $S(\lambda)$ is the UV spectral weighting function [126], $A(\lambda)$ is the aphakic hazard spectral weighting function [128] and $R(\lambda)$ is the retinal thermal hazard spectral weighting function [128].

4.4 Simulated solar irradiance at the surface for selected geographical locations

The incoming solar irradiance at surface level for the three selected locations are displayed in figures 4.7 to 4.9. These irradiances have been weighted with the bilirubin action spectrum $\Gamma(\lambda)$ to assess the effect on isomerisation of bilirubin in irradiated skin. All irradiances are showed as a function of hour of day and day of year in 2015. The irradiance in Dar es Salaam is showed in figure 4.7, the irradiance in Kathmandu is showed in figure 4.8 and the irradiance at Østerås is showed in figure 4.9.

All other simulation results are shown in appendix G. These results include irradiances for both cloudy and clear conditions for all three locations and weightings with both bilirubin action spectrum and the erythema action spectrum. In addition to these results, all data from the satellite overpass have been illustrated graphically.

The bilirubin weighted irradiance for average days calculated for March, June, September and December can be seen in figures 4.10, 4.11 and 4.12 for Dar es Salaam, Kathmandu and Østerås, respectively. These average days give information about the seasonal variations, mean monthly irradiance and length of day for all three locations.

Typical values of irradiance for all three locations are shown in table 4.3. This table shows only irradiance levels at noon for each locations, and specifies the overall maximum and minimum irradiance at noon together with the noon irradiance of the average days for each calculated month.

To assess how the amount of beneficial bilirubin weighted irradiation compares to the amount of potentially harmful erythema weighted irradiation changes, the ratio of the two

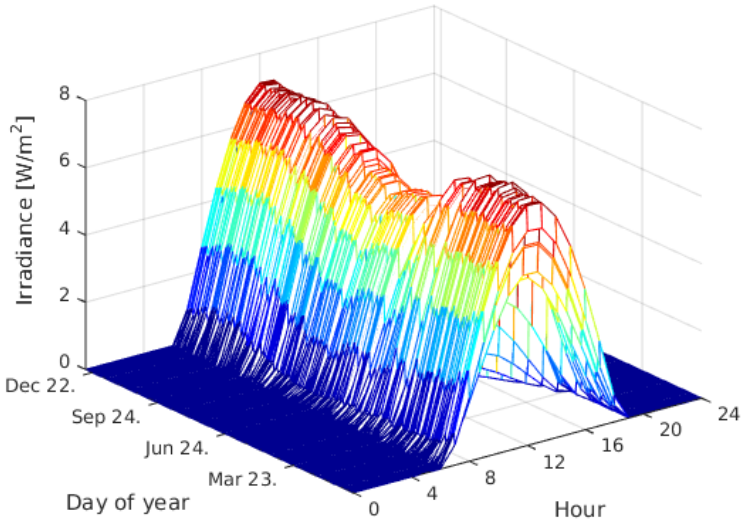

Figure 4.7: Incoming bilirubin weighted solar irradiance in Dar es Salaam as a function of hour of day and day of year throughout 2015. The atmospheric parameters, including cloud cover, were approximated daily by satellite data from [79].

Location	Max	Min	Averages			
			March	June	September	December
	[W/m^2]	[W/m^2]	[W/m^2]	[W/m^2]	[W/m^2]	[W/m^2]
Dar es Salaam	7.3	0.8	6.0	5.2	6.3	6.7
Kathmandu	6.7	0.7	5.2	5.9	5.3	4.0
Østerås	5.4	0.1	2.3	4.0	2.3	0.5

Table 4.3: Overview of the simulated bilirubin weighted irradiances at noon for all three locations for selected situations. The maximum and minimum values denote the noon value with highest and lowest irradiance throughout the entire year. The averages denote the bilirubin weighted irradiance at noon for the average days calculated as described in section 3.1.4.

has been displayed in figure 4.13, figure 4.14 and figure 4.15. This ratio is shown as a function of both hour of day and day of year throughout 2015.

The CMF is shown as a probability density function in figure 4.16. This figure illustrates the probability of measuring a certain CMF at any given day in 2015 for all three locations. The distributions of CMF for all three locations can be seen in appendix G.

In table 4.4, the uncertainties of the coordinates measured by the satellite overpass data are shown for all three locations in latitude and longitude. The actual coordinates are shown in appendix G.

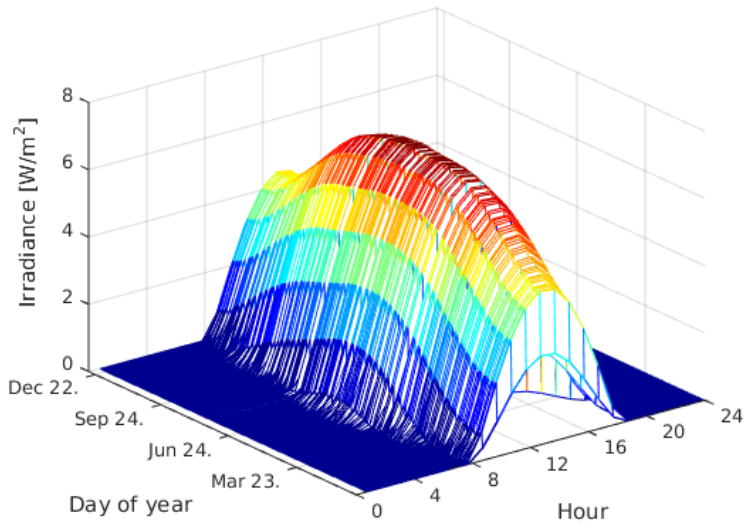

Figure 4.8: Incoming bilirubin weighted solar irradiance in Kathmandu as a function of hour of day and day of year throughout 2015. The atmospheric parameters, including cloud cover, were approximated daily by satellite data from [79].

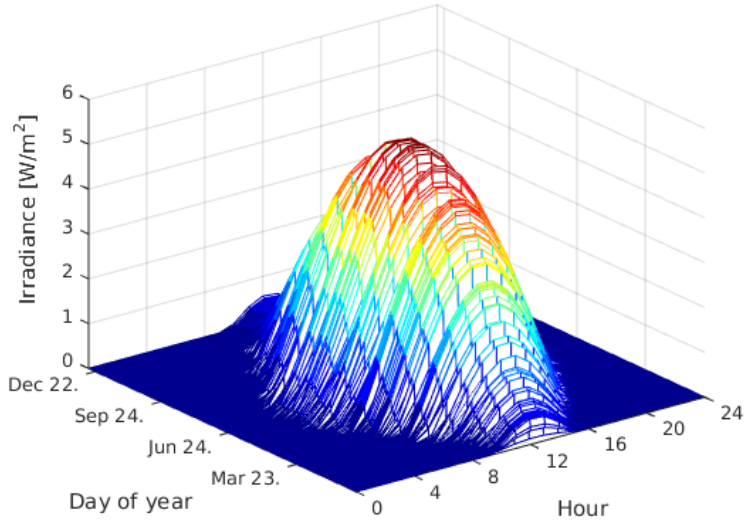

Figure 4.9: Incoming bilirubin weighted solar irradiance at Østerås as a function of hour of day and day of year throughout 2015. The atmospheric parameters, including cloud cover, were approximated daily by satellite data from [79].

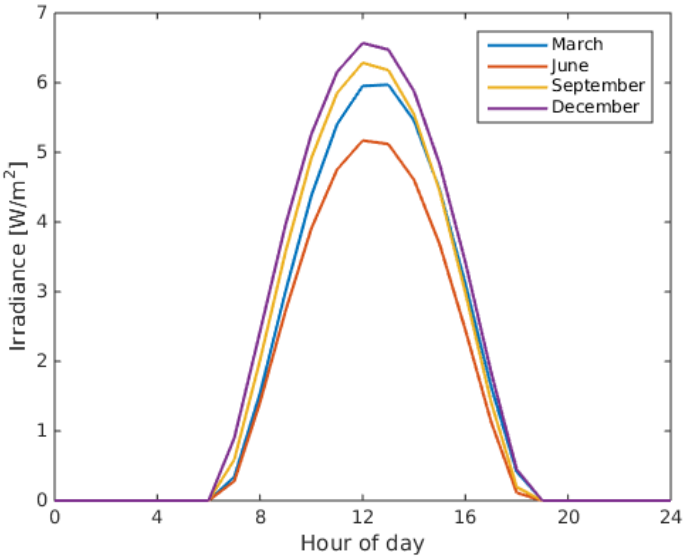

Figure 4.10: Collection of irradiance for average days in Dar es Salaam for March, June, September and December in 2015, based on satellite data from [79].

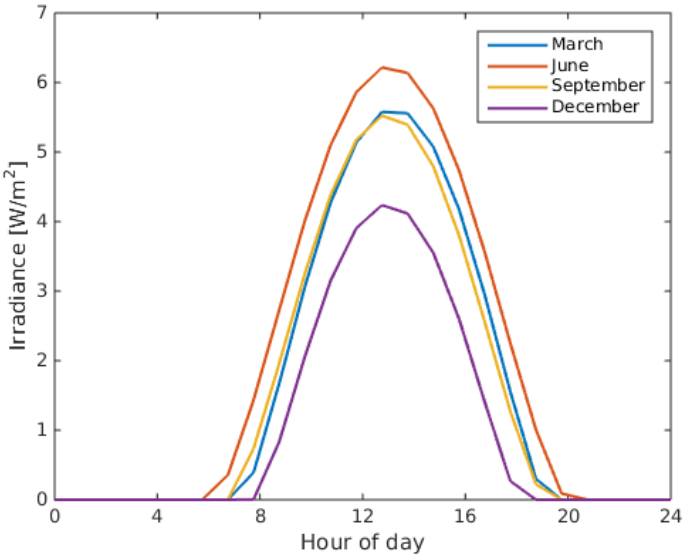

Figure 4.11: Collection of irradiance for average days in Kathmandu for March, June, September and December in 2015, based on satellite data from [79].

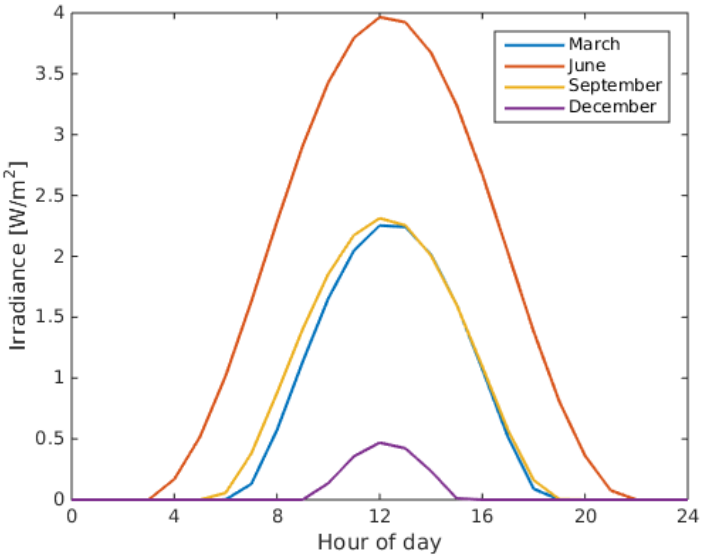

Figure 4.12: Collection of irradiance for average days at Østerås for March, June, September and December in 2015, based on satellite data from [79].

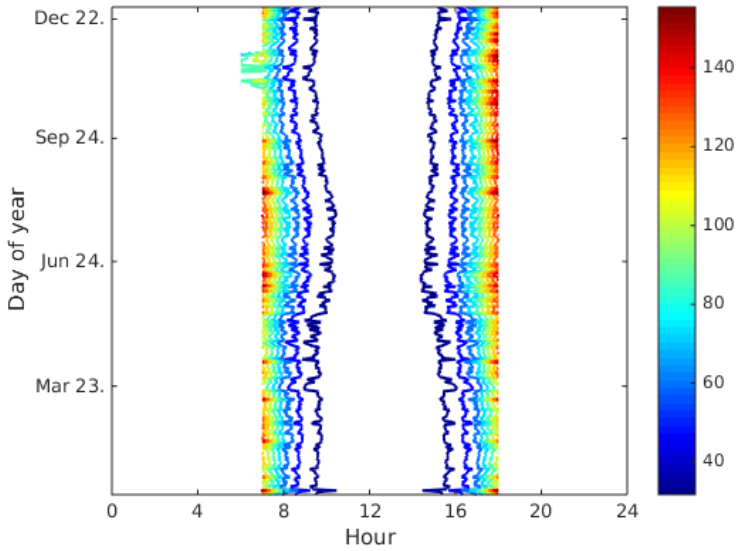

Figure 4.13: Ratio of incoming bilirubin weighted irradiance and erythema weighted irradiance as a function of hour and day of year for Dar es Salaam in 2015. Ratio indicated by colour value.

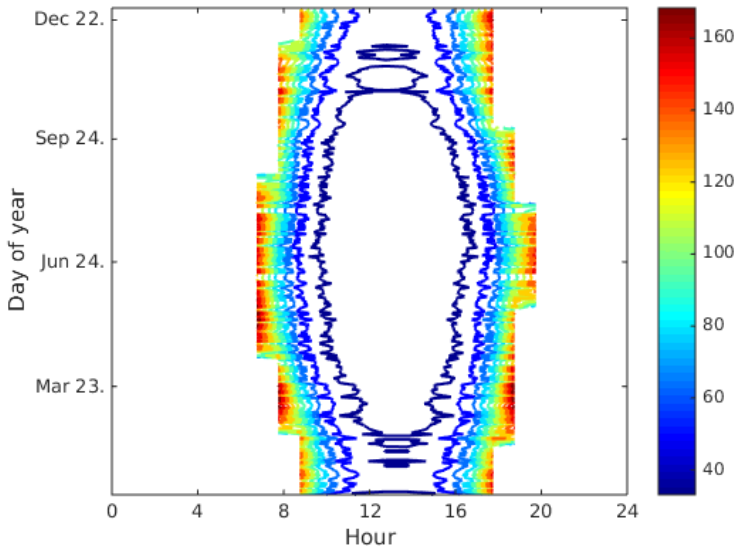

Figure 4.14: Ratio of incoming bilirubin weighted irradiance and erythema weighted irradiance as a function of hour and day of year for Kathmandu in 2015. Ratio indicated by colour value.

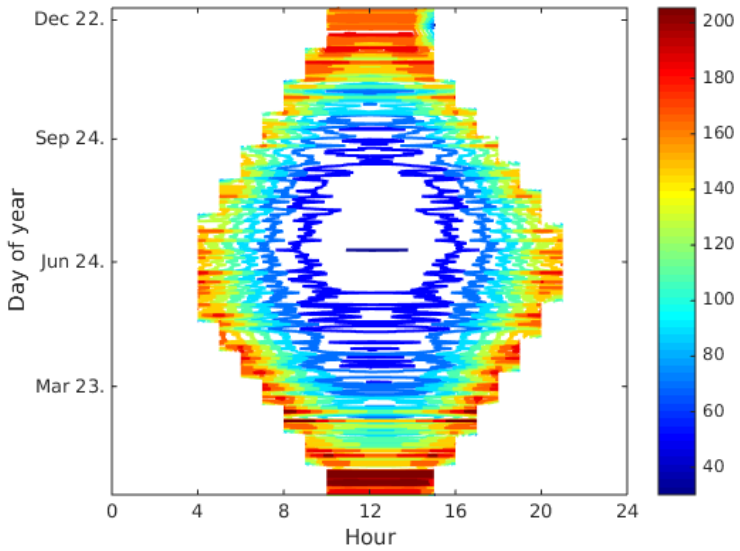

Figure 4.15: Ratio of incoming bilirubin weighted irradiance and erythema weighted irradiance as a function of hour and day of year for Østerås in 2015. Ratio indicated by colour value.

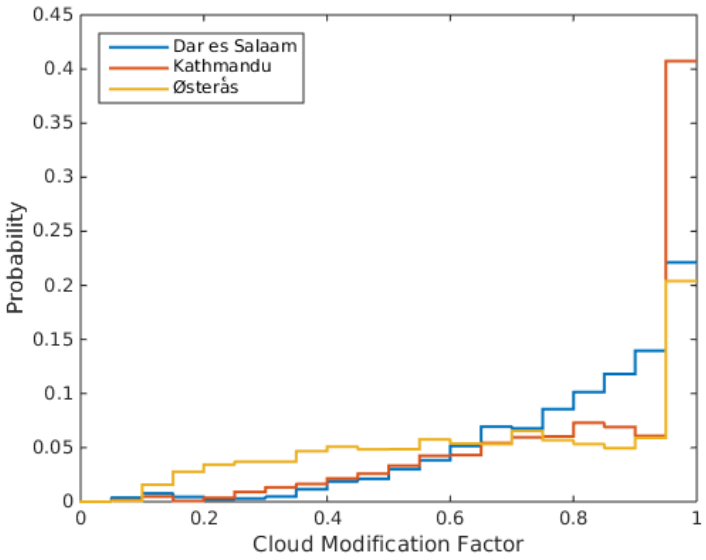

Figure 4.16: The CMF of all three locations, displayed as the probability of getting a certain CMF on any given day in 2015.

Location	Latitude	Longitude
Dar es Salaam	$\pm 0.25°$	$\pm 1°$
Kathmandu	$\pm 0.25°$	$\pm 1°$
Østerås	$\pm 0.50°$	$\pm 2°$

Table 4.4: Illustration of the uncertainty of the geographical coordinates of the satellite data [79] from 2015 for the different locations as compared to the fixed coordinates of table 3.1. The values are approximated from figure G.5.

4.5 Simulations of radiative transfer in skin for different skin colours

Relevant results of the simulations of radiative transfer in skin are presented in this section. The reflectance of the skin for the different skin types are shown in figure 4.17. A comparison of reflectance between healthy infant skin and jaundiced infants is shown in figure 4.18. The skin types with different pigmentation has been plotted separately to clarify the differences between the normal skin colour and the skin colour of an infant suffering from neonatal jaundice.

The main aim of the skin simulations was to investigate the difference in the amount of fluence F at the depth of bilirubin isomerisation for different pigmentations. In figure 4.19, the fluence for wavelength $490\,\text{nm}$ as a function of skin depth z in µm can be seen for the different skin types. The wavelength of $490\,\text{nm}$ has been chosen because this wavelength equals the maximum of the bilirubin action spectrum [64], and thus is the most important wavelength for bilirubin isomerisation *in vivo*. The fluence exceeds 1 close to the surface due to backscattering. The fluence has been made dimensionless according to [139, p.56].

In figure 4.20, the fluence for skin depth $295\,\mu\text{m}$ from the surface for different skin types can be seen as a function of wavelength. This figure illustrates how the different

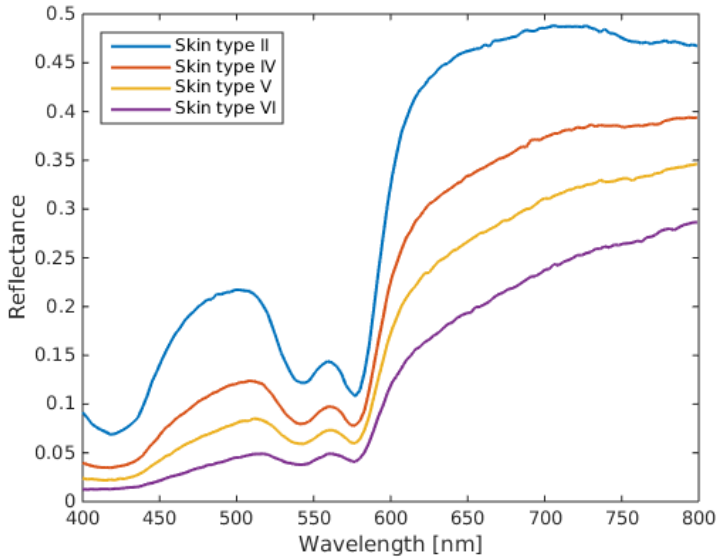

Figure 4.17: Simulated reflectance of newborn skin with GM of 40 *weeks for skin type II, IV, V and VI as a function of wavelength.*

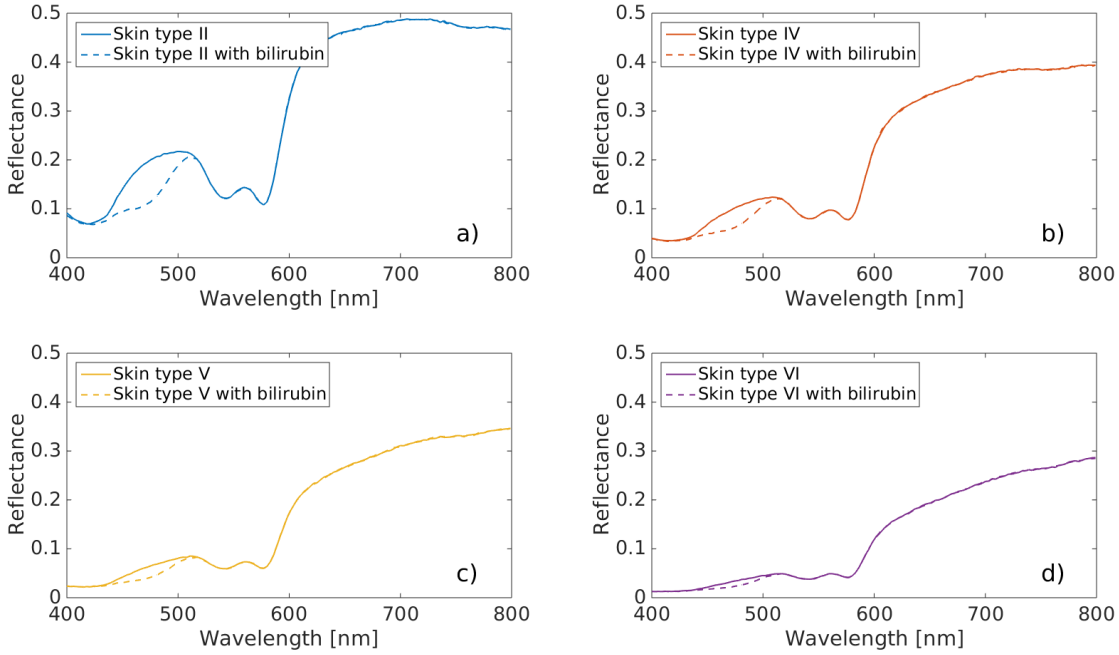

Figure 4.18: Comparison of the simulated reflectance of newborn skin with GM 40 *for skin type II (a), IV (b), V (c) and VI (d) as a function of wavelength for both healthy newborn skin and for skin with a bilirubin concentration of* 350 µmol/L.

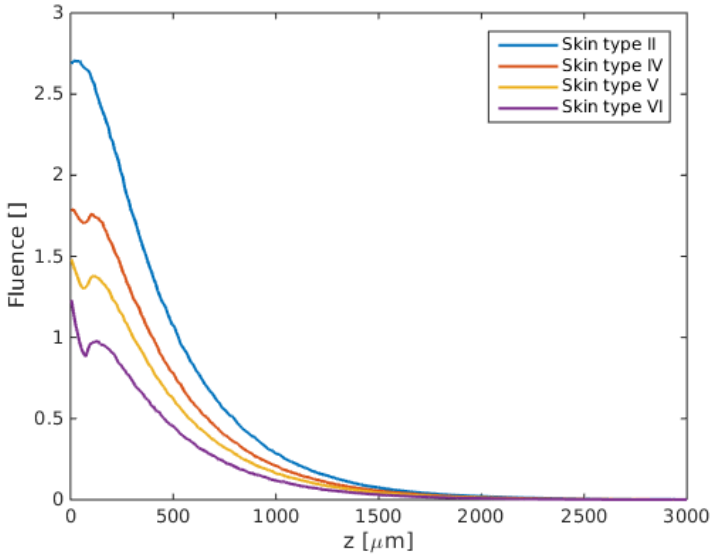

Figure 4.19: Simulated fluence F as a function of the depth of newborn skin z with GM of 40 *weeks for radiation of wavelength* 490 nm *for skin types II, IV, V and VI. The fluence has been made dimensionless as described in [139, p.56].*

wavelengths penetrate the epidermis and dermis down to the assumed depth of bilirubin. In figure 4.21, a comparison of the fluence at 295 µm for healthy infant skin and jaundiced infant skin is illustrated. The skin types has been separated to clarify the differences.

In table 4.5, the numeric results of the fluence assumed most relevant for isomerisation of bilirubin is displayed. In this table, the decreasing fluence for the different skin types is shown together with the relative amount of fluence compared to the reference of skin type II. The fluence is showed for both healthy infant skin and for jaundiced infant skin. The fluences have been compared separately for healthy infants and infants suffering from neonatal jaundice.

The optical coefficients of infant skin of GM 40 weeks for different skin types are graphically presented in appendix H. From the absorption coefficient μ_a, the scattering coefficient μ_s and the scattering anisotropy g, the penetration depth δ may be calculated according to equation (2.33). The penetration depth of radiation as a function of wavelength in the epidermis for each skin type is illustrated in figure 4.22, and the penetration depth of

Skin type	Fluence	Comparison in %	Fluence with bilirubin	Comparison in %
II	1.78	100%	1.18	100%
IV	1.28	71%	0.88	75%
V	1.03	58%	0.71	60%
VI	0.75	42%	0.52	44%

Table 4.5: Simulated fluence F for visible light with wavelength 490 nm *at* 295 µm *depth in newborn skin with GM of* 40 *weeks for skin types II, IV, V and VI. The fluence has been made dimensionless according to [139, p.56]. Jaundiced skin with bilirubin contains* 350 µmol/L *bilirubin evenly distributed in the dermis. Skin type II has been chosen as reference.*

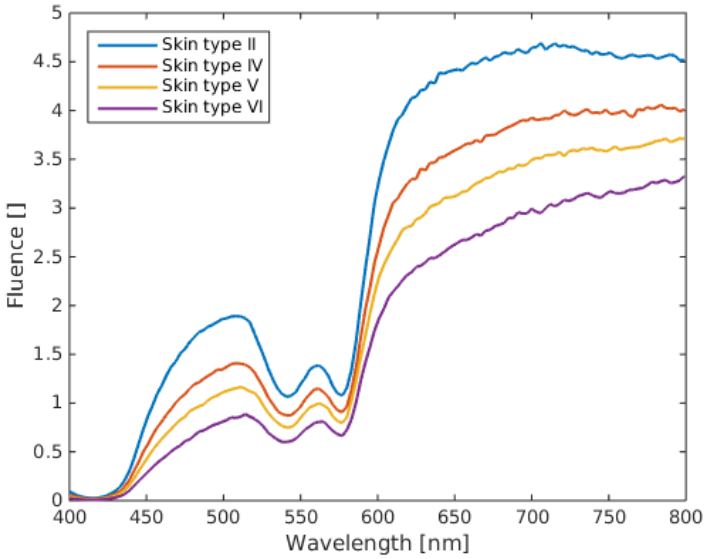

Figure 4.20: Simulated fluence F at a depth of $295\,\mu m$ *in newborn skin with GM* 40 *weeks as a function of wavelength for skin types II, IV, V and VI. The fluence has been made dimensionless as described in [139, p.56].*

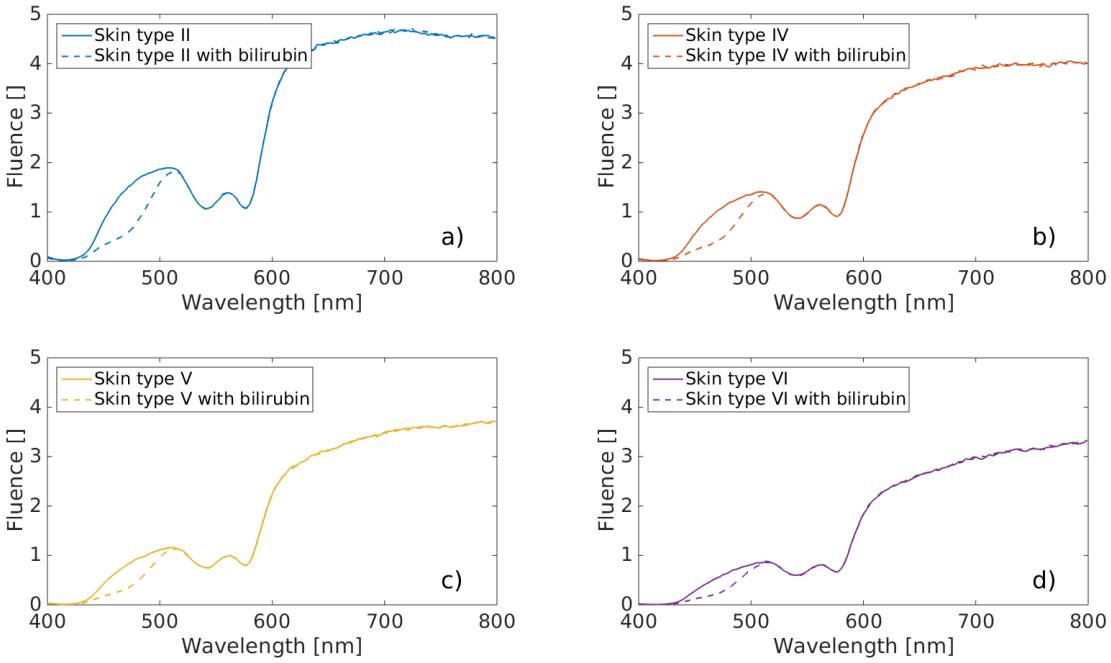

Figure 4.21: Comparison of the fluence F at a depth of $295\,\mu m$ *in newborn skin with GM* 40 *weeks as a function of wavelength for skin types II (a), IV (b), V (c) and VI (d) for both healthy newborn skin and for skin with a bilirubin concentration of* $350\,\mu mol/L$*. The fluence has been made dimensionless as described in [139, p.56].*

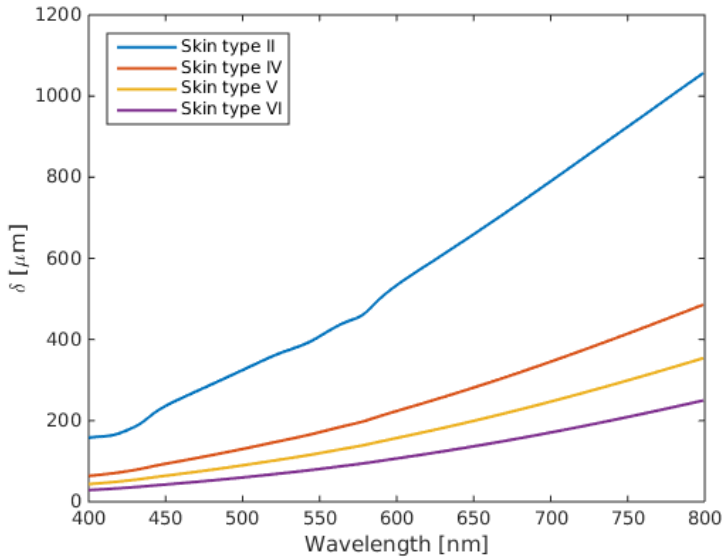

Figure 4.22: The calculated penetration depth δ for the epidermis of infant skin with GM 40 *weeks as a function of wavelength for skin types II, IV, V and VI.*

the radiation as a function of wavelength in the dermis for healthy and jaundiced infant skin can be seen in figure 4.22. In table 4.6, the penetration depth for radiation of wavelength 490 nm is displayed for both epidermis, normal dermis and jaundiced dermis as a function of simulated skin type.

Skin type	δ epidermis [μm]	δ normal dermis [μm]	δ jaundiced dermis [μm]
II	307	368	251
IV	122	368	251
V	84	368	251
VI	56	368	251

Table 4.6: Calculated penetration depth of radiation with wavelength 490 nm *for both epidermis and dermis for skin types II, IV, V and VI. When bilirubin is present in jaundiced skin, it is uniformly distributed in the dermis with a concentration of* 350 μmol/L.

4.6 Calculation of exposure times for sunlight treatment

In this section, the exposure times necessary for gaining a radiant exposure equal to conventional phototherapy at St. Olavs Hospital are calculated for average simulated days for the chosen locations and skin types II, IV, V and VI. The amount of adverse radiant exposure is also calculated.

Received radiant exposure during conventional phototherapy

When calculating the received bilirubin weighted [64] radiant exposure during phototherapy, it is necessary to know both the total irradiance and the exposure time. If different

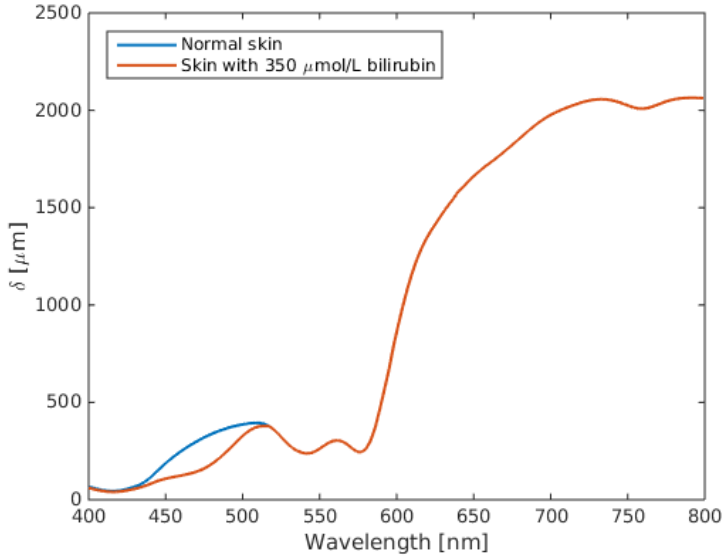

Figure 4.23: The calculated penetration depth δ for the dermis of infant skin with GM 40 *weeks as a function of wavelength, both for normal skin and for skin with* 350 µmol/L *bilirubin.*

sources are to be compared, a statement of radiant exposure is not sufficient. To state only the radiant exposure does not give the necessary information of the biological effect of the radiant exposure, as a very high irradiation for a short timespan does not have the same effect as a low irradiance over a long timespan [21, 102, 103].

For phototherapy treatment, the schedule stated as an example in the Norwegian guidelines [90] will be used as the basis for the exposure time. This example states a treatment exposure of 24 hours, with a 30 min feeding every 2.5 hours. This schedule thus corresponds to 2.5 hours of irradiation for every 3 hours of treatment for a normal infant, and a total of 20 hours of irradiation for 24 hours of treatment.

In table 4.1, the total average irradiance for the recommended type of phototherapy is given as $1.03\,\mathrm{mW/cm^2}$. The calculation of received radiant exposure D_bil for bilirubin weighted irradiance becomes

$$D_{bil} = 10.3\,\mathrm{W/m^2} \cdot (2.5\,\mathrm{h} \cdot 8) \cdot 3600\,\mathrm{s/h} = 7.42 \cdot 10^5\,\mathrm{J/m^2}, \tag{4.1}$$

and similarly, the radiant exposure for irradiance in the UVA range D_{UVA} becomes

$$D_{UVA} = 0.009\,\mathrm{W/m^2} \cdot (2.5\,\mathrm{h} \cdot 8) \cdot 3600\,\mathrm{s/h} = 6.77 \cdot 10^3\,\mathrm{J/m^2}. \tag{4.2}$$

These equations give the necessary radiant exposures in $\mathrm{J/m^2}$ for phototherapy as according to the Norwegian guidelines. As the Norwegian guidelines are assumed to be optimal, this radiant exposure is similarly assumed to be optimal regarding treatment of neonatal jaundice.

Calculating necessary exposure time for sunlight

The acquired radiant exposures for each average day are shown in table 4.7. This table includes the calculation of both the bilirubin weighted radiant exposure and the erythema

Location	Month	Radiant exposure per day [J/m^2]	Days required	SED per day
Dar es Salaam	March	$1.50 \cdot 10^5$	4.9	59.5
	June	$1.27 \cdot 10^5$	5.8	40.9
	September	$1.58 \cdot 10^5$	4.7	55.3
	December	$1.73 \cdot 10^5$	4.3	63.8
Kathmandu	March	$1.43 \cdot 10^5$	5.2	40.9
	June	$1.77 \cdot 10^5$	4.2	64.6
	September	$1.41 \cdot 10^5$	5.3	49.4
	December	$9.41 \cdot 10^4$	7.9	20.2
Østerås	March	$5.52 \cdot 10^4$	13.4	6.3
	June	$1.36 \cdot 10^5$	5.4	27.1
	September	$6.03 \cdot 10^4$	12.3	9.8
	December	$5.87 \cdot 10^3$	126.4	0.4

Table 4.7: Overview of received radiant exposure per average days for all three locations, both for bilirubin weighted irradiation in J/m^2 *and erythema weighted irradiation in SED. The average days of solar exposure required to achieve the phototherapy radiant exposure from equation* (4.1) *are also specified.*

Month	D per day [J/m^2]	D per midday [J/m^2]	$\%D$ during midday
March	$1.50 \cdot 10^5$	$9.93 \cdot 10^4$	66%
June	$1.27 \cdot 10^5$	$8.55 \cdot 10^4$	67%
September	$1.58 \cdot 10^5$	$1.04 \cdot 10^5$	66%
December	$1.73 \cdot 10^5$	$1.10 \cdot 10^5$	63%

Table 4.8: Calculation of the bilirubin weighted radiant exposure D in Dar es Salaam for both daylong exposure and exposure during midday from 10:00 to 15:00. The percentage of the daily radiant exposure incident in the midday period is also calculated.

weighted radiant exposure. The erythema weighted radiant exposure is given in SED as defined in section 2.6. The amount of average days required to achieve a radiant exposure equal to D_{bil} from equation (4.1) for the bilirubin weighted irradiance has also been specified. One average day is counted as exposure from sunrise to sunset.

To determine the amount of radiant exposure for the midday hours, Dar es Salaam has been used as an example. In table 4.8, both the radiant exposure for the whole average day and the radiant exposure for the midday hours from 10 am to 15 pm are shown. Further, table 4.8 shows the percentage of the daily radiant exposure which is incident in the midday hours.

Differentiating for skin types

To account for the difference in pigmentation of different skin types, the amount of necessary days to achieve D_{bil} by use of sunlight may be scaled with the differences in fluence from table 4.5 with skin type II as reference. The results of such a scaling is shown in table 4.9. The resulting exposure times for the different pigmentations will results in the same amount of total fluence at a skin depth of 295 µm.

Location	Month	Days required to achieve D_{bil}			
		Skin type II	Skin type IV	Skin type V	Skin type VI
Dar es Salaam	March	4.9	6.9	8.6	11.8
	June	5.8	8.1	10.1	13.9
	September	4.7	6.5	8.1	11.2
	December	4.3	6.0	7.4	10.2
Kathmandu	March	5.2	7.2	9.0	12.4
	June	4.2	5.8	7.3	10.0
	September	5.3	7.3	9.1	12.6
	December	7.9	11.0	13.7	18.9
Østerås	March	13.4	18.7	23.3	32.2
	June	5.4	7.6	9.4	13.0
	September	12.3	17.2	21.3	29.4
	December	126.4	176.2	218.9	302.4

Table 4.9: Overview of average days required to achieve the phototherapy radiant exposure from equation (4.1) *for different skin types by sunlight exposure. The increase of days for skin types are found from the reduction of fluence for the different skin types as defined in table 4.5.*

Skin type	UVB MED [mJ/cm^2]	UVB MED lower range [SED]
I	$15-30$	1.5
II	$25-40$	2.5
III	$30-50$	3
IV	$40-60$	4
V	$60-90$	6
VI	$90-150$	9

Table 4.10: Overview of values of UVB MED for different skin types, with the range of values taken from table 2.1 [7]. The lower range value is given in SEDs.

Calculating adverse effects

Adverse effects of sunlight in this thesis are mostly limited to erythema. In table 4.10 the UVB MED is shown for all skin types, both as given by Astner and Anderson [7] and in SEDs for the lower range. This lower range is used for calculating the adverse effects of an average day of solar exposure from sunrise to sunset. The results of this calculation is shown in table 4.11, where the amount of SED per day is calculated in table 4.9.

Location	Month	Amount of MED per day per skin type					
		I	II	III	IV	V	VI
Dar es Salaam	March	39.6	23.8	19.8	14.9	9.9	6.6
	June	27.3	16.4	13.6	10.2	6.8	4.5
	September	36.9	22.1	18.4	13.8	9.2	6.1
	December	42.5	25.5	21.3	16.0	10.6	7.1
Kathmandu	March	27.2	16.3	13.6	10.2	6.8	4.5
	June	43.0	25.8	21.5	16.1	10.8	7.2
	September	32.9	19.8	16.5	12.3	8.2	5.5
	December	13.5	8.1	6.7	5.0	3.4	2.2
Østerås	March	4.2	2.5	2.1	1.6	1.1	0.7
	June	18.1	10.8	9.0	6.8	4.5	3.0
	September	6.5	3.9	3.3	2.4	1.6	1.1
	December	0.3	0.2	0.1	0.1	0.1	0.0

Table 4.11: The amount of MEDs for average days of the different months, with the MEDs for the different skin types given in table 4.10. The level of SED per day is given in table 4.7.

Chapter 5

Discussion

This chapter contains the discussion of the results, including comparisons between the results and the different phototherapy guidelines, theory and research previously conducted. In section 5.4, all results are compared in a calculation of the exposure time necessary to achieve the required bilirubin weighted radiant exposure when treating infants with neonatal jaundice. The resulting possibility for treating neonatal jaundice with sunlight is discussed in section 5.5.

5.1 Conventional phototherapy units

When assessing conventional phototherapy, the two important spectral characteristics are the delivered wavelength range and the delivered irradiance to the infant. These two aspects are the ones most frequently specified in treatment guidelines, as seen in section 2.8.1 and the ones necessary to calculate the radiant exposure together with the exposure time [21]. An assessment of equipment used for conventional phototherapy treatment of infants should therefore include both measurements of the spectrum and the delivered spectral and irradiance.

The conventional phototherapy treatment in Trondheim has been defined as the optimal treatment of neonatal jaundice in this thesis. The spectral measurements and spectral measurements of this treatment is compared to the Norwegian guidelines described in section 2.8.

5.1.1 Spectrum and irradiance

When using phototherapy, it is important that the light exposing the infant is as effective as possible, and that it provides as little risk as possible of both acute and chronic damage to the infant. Recent research has shown that the most effective spectrum for isomerising bilirubin in the skin includes longer wavelengths than previously assumed. For lamps used for phototherapeutic treatment today, the typical wavelength peak is 450 nm with a spectral width of about 55 nm. However, lamp spectra with emission around 490 nm seem to be more optimal according to the bilirubin action spectrum shown in figure 2.13 [28, 64, 104, 134]. This result indicates that the treatment of neonatal jaundice would be more effective if the light used was within the turquoise part of the visible spectrum rather than the blue. Such an optimisation must be a weighting between isomerising

bilirubin and avoiding adverse effects. It has been shown *in vitro* that blue radiation causes higher degrees of DNA damage and cytotoxicity than green light [23, 102, 104], which substantiates the advantage of using longer wavelengths.

The measured spectra of both phototherapy units are similar in form and situation of peaks, as expected. The general spectrum can be seen together with the bilirubin action spectrum in figure 4.1, while the specific measurements of each unit can be seen in appendix F. The recorded spectrum corresponds to the spectrum of the Ralutec 71 lamp [98]. The fluorescent peaks similarly correspond to the known peaks of mercury [83]. The Ralutec 71 lamps are low pressure mercury discharge lamps [98], and the correspondence to the known mercury peaks therefore substantiates both the calibration of the spectrometer and the classification of the type of lamps in the units.

The spatial distribution of the irradiance of the overhead phototherapy unit for the recommended settings is shown in figure 4.2. This distribution shows that the bilirubin weighted irradiance varies across the mattress, with the highest values close to the top of the mattress and a decrease of values along the length of the mattress. Maximum and minimum values of the irradiance is shown in table 4.1. The range indicates a large spatial variance from one side of the mattress to another when using the overhead unit. As can be seen in figure 3.4, an infant undergoing treatment might cover the entire mattress. A spatial variance of irradiance such as was measured might make the phototherapeutic effect over the skin variable.

The spatial variance of the irradiance measured from the BiliBed mattress can be found in figure 4.3. This spatial variance is different from the one from the overhead unit, with the maximum irradiance found at the middle of the mattress. The measured range of irradiance for the BiliBed mattress shown in table 4.1 is larger than for the overhead unit, as both the maximum value is larger and the minimum value is lower. For the BiliBed mattress to have full effect, it is therefore important that the infant is placed as near the middle of the mattress as possible.

There were several uncertainties in the irradiance measurements. The greatest uncertainties were connected to the distances, both between the measurement points in the grid and between the infant and the overhead lamp. The uncertainties in distances were always at least ± 0.5 cm due to the ruler used to perform the measurements. For the distance between the overhead lamps and the infant, the uncertainties increased to ± 1.5 cm because of the softness of the mattress which caused the probe to sink down when measuring in the middle of the mattress. However, this effect will be experienced by the infants during treatment as well.

Another uncertainty in the measurement of the irradiances was the direction of the probe. To get comparable results from the different measurement points, the probe should always be facing the same way. This consistency ensures that the cosine dependence of the detector is similar. However, the probe leaned inwards when it was placed on the measurement points at the edges of the mattress, especially at the furthest row of points. The probe was connected to the radiometer by a black cord, and this cord also provided an uncertainty as it might have affected absorption and reflectance to varying degrees. In addition, the cord changed the angle of the probe by providing force and influenced the opening in the reflective curtains when they were drawn.

For the overhead unit in particular, another uncertainty that needs to be accounted for was the variability in the physical placement of the unit compared to the mattress. For each measured distance, the overhead unit was moved manually. This movement may

have caused the unit to become skewed in the horizontal direction, so that either the sides differed in distance to the mattress or that the overhead unit was closer to the mattress at the far side from the stand compared to the bottom of the mattress. The middle of the overhead unit might also have changed from the middle of the grid. In addition, the fluorescent lamps used in both units are only fastened on one end of the lamp. This fastening may cause changing effects and irradiances along the lamps. Both of these uncertainties may account for some of the spatial variability of the phototherapy units.They are however probably representative of the uncertainties during practical use of phototherapy at St. Olavs Hospital.

5.1.2 Effect of curtains and distance on measured irradiance

To investigate the effect of different guidelines for treatment of neonatal jaundice, the irradiance of the overhead phototherapy unit at St. Olavs Hospital was measured for several distances between the infant and the unit as well as both with and without reflective curtains.

The effect of the distance between the infant and the overhead unit for the bilirubin weighted irradiance can be seen in figure 4.4. As can be seen from the figure, the irradiance is higher for closer distances. However, the range of the irradiance values increase as well. For a distance of 20 cm, the maximum bilirubin weighted irradiance approaches $1.8\,\mathrm{mW/cm^2}$ while the minimum value is below $0.2\,\mathrm{mW/cm^2}$. The corresponding extreme points of the irradiance for a distance of $35\,\mathrm{cm}$ is $1.1\,\mathrm{mW/cm^2}$ as the maximum value and $0.4\,\mathrm{mW/cm^2}$. These values gives a decrease in irradiance range of 44%. The changes in variability indicates that the closer an infant is to the overhead unit, the more the effect of the phototherapy depends on the placement of the infant relative to the overhead unit.

The use of a reflective curtain substantially increases the bilirubin weighted irradiance of the overhead phototherapy unit, as seen in figure 4.5. By calculating the ratio between the irradiance at each measurement point for reflective curtains compared to no reflective curtains, the average increase of irradiance is found to be about 40%. This increase corresponds to the increase found by Christensen et al in 1992 for similar experiments [22].

An increase of irradiance due to reflective curtains might influence the effect of the phototherapy treatment considerable. It should be noted that several guidelines differ on the topic of reflective curtains. For instance in the UK, where the use of reflective curtains is expressly advised against [80], the irradiance of the phototherapy will be markedly less than in Trondheim assuming the equipment used is similar. According to Tan, this decrease will greatly impact the effect of the treatment on the reduction of bilirubin [125]. However, it is important to note that there are several reasons for not employing the use of reflective curtains. One is the direct visibility of the infant undergoing treatment. If there are few nurses on call, the time required to lift the reflective curtains manually to check on each infant may be time-consuming and impair effectiveness. However, the reflective curtains shield the nurses from the blue irradiation, which might otherwise be uncomfortable to be exposed to over extended time periods.

When the reflective curtains are used, the amount of diffuse radiation incident on the mattress from the overhead phototherapy unit increases due to the additional reflected irradiation. Due to the angular cosine dependence of the blue probe for angles of less than $60°$, the incoming irradiation in these angles will be recorded accurately. However, for

angles larger than $60°$, the probe does not detect the actual incident irradiation due to a falling angular response. As the infant will benefit from the diffuse irradiation with all incident angles, the effective irradiation with the reflective curtains are likely even higher than measured by this set-up. In addition, the clinical efficiency is probably dependent on irradiated skin area. This irradiated skin area increases with increased reflection, as the irradiation is scattered to otherwise shaded skin.

5.1.3 Comparison of treatment guidelines and treatment at St. Olavs Hospital

The treatment of neonatal jaundice at St. Olavs Hospital is described in section 4.2. This treatment follows the Norwegian guidelines [90] to a substantial degree, for instance by the use of the treatment limits detailed in figure 2.15 and by the use of reflective curtains. The exposure time for infants in phototherapy treatment at St. Olavs Hospital agree with the recommended exposure time of 24 hours for each bout of treatment. The subjectivity of the breaks from treatment are also mentioned in the guideline.

As the amount of available phototherapy units are much larger than the amount of infants normally treated, the availability of the phototherapy units is sufficient. During phototherapy with the overhead unit, the infants at St. Olavs Hospital are placed on a reflective sheet. This reflective sheet was not included in the irradiance measurements of table 4.1, and may increase irradiance to the infant through reflectance. The actual irradiance during phototherapy with the overhead unit might therefore be higher than measured in this thesis.

Regarding the distance between the infant and the overhead unit during phototherapy, the Norwegian guidelines are not followed at St. Olavs Hospital. The guidelines state a recommended distance of $25\,\text{cm}$, while the practice is as little distance as possible. This practice might make the irradiance measurements for a distance of $20\,\text{cm}$ more relevant.

5.1.4 Comparison of total averaged irradiance

The average irradiance of the phototherapy units can be seen in table 4.1. The averages are both over all measurement points and over the measurement points corresponding to the area of the lamps of the phototherapy units. The latter is denoted as a partial average. These two options for calculating the average irradiance has been chosen to achieve a higher reproducibility and because the placement of the infant might vary from treatment to treatment. An averaged total irradiance weighted with phototherapeutic efficacy at every measurement point would depend on the exact placement of the infant undergoing treatment with respect to the irradiation source. This method for averaging is not reproducible, and requires information that is not easily available about the kinetics of bilirubin in different areas of skin. However, a numeric average over the measurement points, either all the points or a collection, is more reproducible. For the average over the measurement points completely covered by the irradiation source, the average is higher than for the average over all measurement points. In this thesis however, the average over all measurement points was chosen as the main average for comparison. This choice increases the reproducibility, while the inclusion of the average calculated over the collection of some measurement points illustrates the effect of the spatial variability of the irradiance.

According to Tan [125], the greatest effect of phototherapy for isomerising bilirubin is found when the irradiance is greater than about $1.2\,\text{mW/cm}^2$ for the wavelength range of $440 - 480$ nm and greater than about $1.75\,\text{mW/cm}^2$ for the wavelength range of $425 - 475$ nm and $400 - 480$ nm. It can be concluded from these results that the irradiance used in phototherapy of infants should exceed $1\,\text{mW/cm}^2$ for adequate effect. This limit agrees with other observations [22].

When following the recommendations of the Norwegian guidelines, the measured average irradiance is $1.03\,\text{mW/cm}^2$ for the overhead unit as shown in table 4.1. This value is just above the minimum recommended irradiance. However, when taking into account that the infants are placed closer to the units than recommended and that the measurement probe most likely did not measure all the diffuse radiation, the actual irradiance might be higher than the recorded average. On the other hand, treatment with shorter distances between the infant and the unit may give the infant variable irradiance for different areas of the skin. The effect of such differences is not clear.

The average irradiance of the BiliBed mattress is $0.67\,\text{mW/cm}^2$ for the entire mattress, which is below the recommended value. However, the BiliBed mattress is only used as an addition to the overhead unit, and is therefore not as important in itself.

It is important to note the specifications of the spectra used for these calculations. Tan used a bilirubin absorption curve with a peak at 450 nm [125]. This bilirubin action spectrum is different from the one found by Lamola and Russo [64], which might make the minimum recommended irradiance different. However, more research is needed to determine optimal irradiance and irradiation conditions. The recommendations from Tan are also based on likely unweighed irradiances [124, 125]. This indicates that the recommendations of total phototherapy irradiance might not be optimal.

5.1.5 Adverse effects of radiant exposure from phototherapy units

There are risks of adverse effects from all radiation when the radiant exposure reaches a certain level. These risks are detailed in section 2.7. To assess what adverse effects the phototherapy treatment of neonatal jaundice might have on the infants, the risks associated with the development of erythema [25] and the spectral weighting functions from ICNIRP [126–128] have been investigated together with the spectrum of the overhead phototherapy unit in spectral irradiance, as found in section 3.1.6. These calculations have been performed in section 4.3.

In figure 4.6, the phototherapy spectrum has been weighted with the erythema action spectrum $S_{er}(\lambda)$, the UV spectral weighting function $S(\lambda)$, the aphakic hazard spectral weighting function for blue light retinal damage of children below 2 years of age $A(\lambda)$ and the retinal thermal hazard spectral weighting function $B(\lambda)$. The results show that the adverse effects of UV radiation, both for UV radiation in general and for the specific effect of erythema, are very small in the spectral range of blue of the phototherapy lamps investigated. However, the retinal hazard functions have higher values in the spectrum of the phototherapy, and may affect the infant during treatment.

The received radiant exposure weighted with the adverse effects for both exposure times are shown in table 4.2. The values in this table may be directly compared to the limits set by the international standards for exposure to radiation in the visible and UV ranges.

For the erythema weighted irradiance, the standard of adverse effects is measured in

MEDs or SEDs, as described in section 2.7.1. For skin type I, which is characterized by having the greatest effect of UV radiation, the lower range of the UVB MED is set at $150\,\mathrm{J/m^2}$ according to table 2.1. This value is used as reference as it is the lowest limit for all skin types, and therefore the lowest radiant exposure which may cause adverse effect for erythema. It can be seen from table 4.2 that D_{ery} is below this limit for an exposure of 2.5 hours, while it is above the limit for exposure of 20 hours. This indicates that erythema might be a possible reaction of phototherapy, which is substantiated by increased pigmentation in infants after treatment [68].

However, erythema might be induced by UVA irradiation alone [112], and MED values for UVA irradiation is displayed in table 2.1. Equation (4.2) state the radiant exposure from unweighed UVA irradiation, which is it assumed the MED values are calculated for. The lower range of the UVA MED for skin type I gives an MED of $2 \cdot 10^5\,\mathrm{J/m^2}$. The calculated effect of D_{UVA} from equation (4.2) for the entire phototherapy treatment is about 3% of this MED. This low value indicates that the risk of erythema from the UVA radiant exposure of conventional phototherapy is extremely low, assuming the UVA MED values calculated by Fitzpatrick [7, 33] are accurate, and that they apply to infant skin.

The exposure limits set by the ICNIRP can be seen in table 2.3. By comparing table 4.2 with these exposure limits that none of the radiant exposures are within the limits. However, these limits are calculated for the general population and do not apply to medical treatment. In addition, infants treated with phototherapy wear shielding over their eyes which reduce the retinal irradiation. Due to this, the adverse effect of D_A and D_R will be substantially less than calculated here.

There are several accounts of risks from the use of phototherapy on infants in the literature. Roll and Christensen summarises some of these risks in [103]. One of the suggested risks includes an increased risk of acute lymphoblastic leukemia, which might be connected to a history of phototherapy treatment. It has also been shown that bilirubin irradiated with visible light might form hydrogen peroxide (H_2O_2). In addition, the photo reactions of bilirubin itself may cause DNA damage and mutations as cited in [102, 104]. However, radiation with longer wavelengths, i.e. green or turquoise light, cause less cellular effects than blue light [104].

On the other hand, there have been several studies which conclude that the phototherapy treatment pose no long term adverse effects to infants [12, 103]. According to Paller et al [94], the exposure of infants to the blue light of phototherapy increases the risk of melanocytic nevi, often also called moles, but not the risk of developing skin cancer. However, it should be discussed whether the relevant studies have been conducted long enough after the phototherapy treatment was conducted and if the history of phototherapy can be found in hospital records for possible future epidemiological studies. As stated by Lucas et al [67], solar exposure may cause increased risk of cancer later in life. If infants treated with phototherapy experience a similar increase of risk, the results will not be apparent until later in life. The follow-up studies must therefore be conducted with a greater timespan for the risks to be determined with greater accuracy [103].

5.2 Atmospheric simulations

The possibility of treating infants with neonatal jaundice by exposure to sunlight may be assessed by investigating the atmospheric irradiation through the atmosphere for different

atmospheric conditions and geographical locations. However, the atmospheric conditions change often. This variability makes the prediction of the efficacy of sunlight for treatment of neonatal jaundice difficult. In addition, atmospheric processes are coupled between the dynamics, radiation and chemistry of the atmosphere [4, p.216]. An atmospheric modelling needs to account for all the physical parameters within the three categories. As with other chaotic processes, the evolution of the atmospheric irradiation is sensitive to the initial conditions [4, p.219].

5.2.1 Satellite overpass data

By using initial atmospheric conditions from data captured by satellite overpass, the initial conditions of the atmospheric modelling may be approximated closer to real conditions. The results become more accurate, and are perceptibly different for different geographical locations. The locations chosen in this thesis are displayed in table 3.1. In appendix G, the satellite data appropriated from [79] are displayed for all locations. It can be seen that the ozone levels of the atmosphere above Østerås is larger, and more variable, than above both Kathmandu and Dar es Salaam, which have approximately stable ozone levels of about $275\,\mathrm{DU}$ throughout the year. It is also apparent that the variability of the ozone level is larger in winter. These observations correspond with the predictions of section 2.4.1.

The albedo is also more variable for Østerås than for the other locations, both on a weekly basis and a seasonal basis. This variability may be explained with the latitude. Østerås is at 60° N, which gives snow during winter time. The albedo is higher for the winter season than for the rest of the year, which might be due to the snow. For the summer months, the albedo of Østerås is however lower than for both Kathmandu and Dar es Salaam. This difference might be due to the large wooden areas around Østerås. The areas around both Dar es Salaam and Kathmandu are dominated by grasslands and desert or mountains, respectively, according to the satellite view on Google maps [38]. According to Hansen [41], dry and sandy soil has an albedo of 0.25, grass has an albedo up to 0.27, while coniferous trees has an albedo of 0.14. A light snow cover has an albedo from 0.31 and above. These values correspond to the values of albedo collected from the satellite overpass data.

The effective cloud cover is approximated by the cloud optical depth. This cloud optical depth is more variable at Østerås than at the other locations, and at Østerås there is a larger probability of getting a cloudy day. The greatest probability of getting completely clear cloud conditions is found in Kathmandu, where this probability is above 60%. This high proportion of clear conditions might be a consequence of the latitude of Kathmandu, which is situated at 30° N. This latitude is the same latitude as large desert areas like the Sahara, and the latitude where cool, dry air often descend from the atmosphere between the Hadley cell and the Ferrel cell on the northern hemisphere [30]. This descending air creates a stable high pressure area, which results in more clear cloud conditions. The cloud optical depth also includes information on the seasonal cloud cover, and how the time of year impacts the level of clouds in the atmosphere.

The accuracy of the satellite overpass data may be indicated by assessing the position of the different measurements. The uncertainty of the satellite positions in terms of coordinates for the overpass data is displayed in table 4.4. The length of one degree of latitude is approximately constant at $111\,\mathrm{km}$ [141], while the length of one degree of longitude varies with the latitude, as the longitude circles diminish closer to the poles.

Close to the equator, the length of one degree of longitude is ≈ 111 km, at 30° the length is ≈ 96 km, at 60° the length is ≈ 56 km, and at the poles the length is of one degree of longitude is zero [141]. The uncertainties in table 3.1 now correspond to around $20-50$ km in North-South direction and about 100 km in East-West direction. These uncertainties are quite large when the satellite datasets are used to approximate the atmospheric conditions in one fixed location. However, it is not of an order of magnitude which will change the general surface conditions, ozone level or weather conditions for the atmospheric input data. A larger uncertainty is connected to the constant value of the atmospheric conditions for entire simulated days at a time, and the varying amount of datasets for the separate locations. The inherent uncertainty in satellite overpass data must also be accounted for, as the satellite has trouble seeing the difference between the low atmospheric cloud cover and the albedo on the surface.

The use of satellite data for simulating atmospheric conditions is not a novel idea. The accuracy of typical satellite overpass data when assessing the solar UV irradiation, and thus the ozone layer, has been previously recounted by Bhattarai et al in 2007 [11] for Kathmandu and by Bernhard et al in 2015 [10] for high northern latitudes.

The assessment by Bhattarai et al was done by measuring the incident UV irradiation in Kathmandu with a GUV instrument from Biospherical Instruments Inc, which may be similar to the GUV used at the NRPA described in section 3.2.1. Further, they simulated the incident irradiation with uvspec from *libRadtran*, using the ozone measurements from TOMS (total ozone mapping spectroradiometer) by satellite [11]. Bhattarai et al found that the UV index calculated from TOMS gives values higher than the ground measurements by about 30%. This difference is substantial, and is an indication of the great variability of the atmospheric modelling and the low accuracy of the satellite overpass data. It might also indicate that the level of UV radiation at the surface is less than found by the simulations performed in this thesis. However, Bhattarai et al [11] used a different source of satellite data than was used in this thesis, as well as a different time-span. In addition, they used the uvspec mid-latitude winter profile for atmospheric composition, while the mid-latitude summer profile was used in this thesis.

Bernhard et al also found large differences in the UV satellite measurements, which were especially connected to errors in the satellite surface albedo [10]. For large differences in satellite surface albedo, the UV results differed with more than 50%. If such differences are present in this thesis, the calculation of the adverse effects of UV radiation might be exaggerated or understated.

5.2.2 Potential for sunlight therapy as function of location

To account for the potential of sunlight therapy as a function of geographical location, the incoming irradiance simulated for approximately real atmospheric data from the satellite overpass measurements must be assessed. The simulated incoming irradiance is displayed in figures 4.7, 4.8 and 4.9 for cloudy conditions. It may be seen that the cloud cover varies greatly, and does not impact the underlying yearly variations of the irradiation. This yearly variation is a function of the geographical location, which influences the solar zenith angle as a function of day of year and time of day. Comparable solar zenith angles as a function of day of year and time of day may be seen in [107].

The CMFs for the different locations are displayed in figure 4.16 as probability density functions. This figure shows what effect the typical atmospheric cloud cover has on the

incoming irradiation for the different locations, and the probabilities of a certain CMF for any glance upwards as long as the sun is above the horizon. Figure 4.16 shows that the most probable cloud cover is a clear sky for all locations, but that it is about twice as likely to happen for Kathmandu as for Østerås. The probability of a clear sky is not much higher for Dar es Salaam than for Østerås, but Dar es Salaam has the largest probability of getting a thin cloud cover which does not impair the incoming solar irradiance by more than 20%. For heavier cloud covers, which impair more than 40% of the incident solar irradiation, the largest probability is found for Østerås.

The cloud cover has the largest impact on the effect of sunlight for treatment of neonatal jaundice [107]. On one hand, the total irradiance in cloudy conditions diminish as can be seen in figures 4.7 to 4.9. On the other hand, the ratio of the beneficial to harmful irradiation increases, as was seen in the previous specialization project [107]. This effect can also be seen in figure 4.13, 4.14 and 4.15. In these figures, the ratio of the bilirubin weighted irradiation and the erythema weighted irradiation is presented as a function of day of year and time of day. The time of sunrise and sunset is also apparent as a function of latitude.

As mentioned in section 2.4, the erythema weighted irradiance decreases as the path through the atmosphere lengthens due to scattering and for less transparent atmospheres due to an increased amount of Mie scattering. This increase causes the effect on the ratios of beneficial to harmful irradiation, as the reducing effects are less apparent for the visible light than for UV radiation. It can be seen from figures 4.13 to 4.15 that the ratio is larger for Østerås than for the other locations, which may be due to a lower CMF, and that the higher latitude has a larger degree of high solar zenith angles, which gives higher ratios. A higher ratio means that the amount of beneficial effect on the bilirubin concentration of the infant is higher for each exposure equivalent to one MED of UV-exposure. To avoid the risk factors and adverse effects of the sunlight and still acquire the largest possible radiant exposure of beneficial irradiation, the treatment of neonatal jaundice by sunlight should be conducted in the timespan where the ratio is highest. This procedure means to avoid exposure during the midday, and to instead use longer exposure times in the morning and evening.

The effect of less transparent atmospheres on both the solar irradiance and the ratio of beneficial to harmful irradiation is not discussed further here, but is mentioned in section 5.6 as future research.

5.2.3 Comparison of irradiances from sunlight and conventional phototherapy

In table 4.3, the ranges of the simulated bilirubin weighted solar irradiance at the selected locations are displayed for different situations. These irradiances might be compared to the irradiance of the conventional phototherapy.

The average bilirubin weighted irradiance for the recommended phototherapy at St. Olavs is $10.3\,\mathrm{W/m^2}$, according to table 4.1. This irradiance exceeds all values for the solar irradiation, which has its overall maximum value of $7.3\,\mathrm{W/m^2}$. This maximum irradiance occurs at Dar es Salaam, while the maximum value at Kathmandu is about 92% of the overall maximum. For the bilirubin weighted irradiance at noon for the average days, the irradiance ranges from 65% to 50% of the total irradiance for conventional phototherapy in Dar es Salaam and from 57% to 39% in Kathmandu. For Østerås, the noon irradiance for

June is 39% of the total irradiance for conventional phototherapy, while the other months are considerably lower.

For average noon irradiances, both Dar es Salaam and Kathmandu are within the range of measured bilirubin weighted irradiances from the recommended settings of conventional phototherapy, which can be seen in table 4.1. This range defines the phototherapy treatment which is deemed effective at St. Olavs Hospital, and indicates that sunlight treatment of neonatal jaundice might be considered effective for these locations. However, Østerås is only within the range of irradiance from the overhead unit when reflective curtains are not in use, and if the average noon irradiance from December is neglected.

5.3 Simulations of fluence in skin

To assess the effect of the treatment of phototherapy for different skin types and ethnicities, this thesis has investigated the effects of the different optical parameters for skin with different pigmentations with a Monte Carlo simulation. In a Monte Carlo simulation, the incident photons are followed individually, and a large number of photons are gathered to generate statistical probability densities which mirror the actual conditions sufficiently well. However, this applicability depends on the amount of photons modelled.

In this thesis, a number of $100\,000$ photons were modelled for every Monte Carlo simulation of radiative transfer. In examples of a similar program written by Wang and Wu [139, p.55], the amount of photons used are $50\,000$. Wang and Wu here finds a good agreement between their simulations and the reality. It is therefore safe to assume that the results of the MCML-simulation performed in this thesis results in a good agreement with reality as well, assuming that the initial values and optical parameters are defined correctly. A larger number of photons would not have made a difference to the results, but would have used substantially more computational time.

5.3.1 Optical differences in skin types

The aim of the skin simulations was to determine the differences between skin types as this will influence the efficiency of the phototherapy. The most important results are the fluence and the penetration depth. However, the reflectance is also interesting as it is a measure of the perceived colour of the skin. A greater deal of reflectance indicates a perceived lighter colour of skin, similar to how white surfaces reflecting all incoming irradiation compared to black surfaces.

In figure 4.17, the reflectance can be seen for the infant skin of different skin types. As expected, the reflectance drops for the darker skin types and these skin types absorb more of the incoming irradiation. This effect is especially clear for the shorter wavelengths, where the melanin has a stronger absorption. For jaundiced skin, the reflectance is affected in the blue wavelength range. This effect is illustrated in figure 4.18. As the absorption in the blue and green wavelengths is larger for jaundiced skin, the skin will appear more yellow than for healthy skin. It is evident from the difference in skin types that this effect is more pronounced for infants with a lighter skin type, which makes neonatal jaundice easier to spot by skin colour in skin types below V. This observation corresponds with results from Olusanya et al [92].

The range of the photons depend on optical parameters. One way of assessing the amount of photons for a given distance from the skin surface is by determining the simulated fluence F. In figure 4.19, the fluence for wavelength 490 nm is illustrated as a function of skin depth in µm. From this figure it is apparent that the amount of photons reaching the skin at a certain depth is largely dependent on skin type, as the fluence of skin type II is more than double that of skin type VI already at the skin surface. The largest difference is found in the epidermis, which is the first 80 µm of the skin and which is where the melanin is situated. The fluences of the different skin types converge in the dermis, but do not correspond until deeper than 1500 µm, where the fluence becomes very small.

The bilirubin is assumed to be diffused into the skin from the blood vessels, and to exist at most depths in the skin. As described in section 3.3, a skin depth of 295 µm has been chosen to investigate the phototherapeutic difference between skin types of different pigmentations. This depth is not chosen because of large amounts of bilirubin at exactly this distance from the skin surface, but because the probability of finding bilirubin molecules in this depth is high. This high probability is due to the placement near the blood vessels which bilirubin diffuse from, and it is situated in the dermis where the bilirubin is modelled. In addition, the amount of fluence at this depth is relatively high as shown in figure 4.19.

By comparing the fluence at a skin depth of 295 µm as seen in figure 4.20 to the reflectance at the surface in figure 4.17, a red-shift of the fluence is apparent. The short wavelengths are absorbed more by the outer layer of skin, e.g. by melanin, while the longer red wavelengths have a larger penetration depth. When comparing healthy skin to jaundiced skin, it may be seen that the fluence in the wavelengths relevant for photoisomerisation of bilirubin has been further reduced. This may indicate that the phototherapy is less effective for very jaundiced skin than for healthy skin due to the decreased penetration depth, as less of the photons reach the assumed depth of the bilirubin. However, for jaundiced skin the concentration of bilirubin in the skin will be higher and distributed throughout the skin volume, which increases the phototherapy efficiency.

The blood fraction of the tissue is important for the detection of bilirubin in tissue. For high hemoglobin absorption in skin, the bilirubin absorption is masked. This shielding effect of blood has been described by Svaasand et al [122], and simulated by Randeberg et al [99]. In the simulation by Randeberg et al, a higher blood fraction, and thus higher hemoglobin absorption, caused the bilirubin absorption to be less pronounced in the reflectance [99]. A lower hemoglobin absorption increased the bilirubin absorption. The shielding effect comes from the high absorption of hemoglobin, which acts as a sink for the optical radiation. The photons are absorbed by the hemoglobin, and the penetration depth is decreased. This effect is also mentioned by Lamola and Russo [64], who states that the competition for phototherapy light by hemoglobin in the skin is the defining factor for the absorption spectrum of bilirubin. The shielding of bilirubin by blood might therefore impact the degree of observable yellowing for infants, especially with a high blood absorption and volume fraction in the skin.

The penetration depth in the epidermis is displayed in figure 4.22 for the different skin types, and the penetration depth in the dermis is displayed in figure 4.23 for both healthy and normal infant skin. As the scattering coefficient and the scattering anisotropy are constant as a function of wavelength for differences in concentrations of melanin and bilirubin, it is the dependence of the absorption coefficient for these chromophores that determine the penetration depth. This dependence might change when other chromophores are included. Numerical values of the penetration depth for wavelengths of 490 nm are

displayed in table 4.6. However, according to Lister et al [66], melanin contributes greatly to skin scattering. This contribution indicates that the scattering coefficient should be dependent on the concentration of melanin, and thus the skin type. This disparity is a possible uncertainty of the skin simulations.

The penetration depth states the depth at which 63% of the incident photons have been absorbed. The penetration depth is also a measure of how visible the skin is to radiation, as the tissue below 2δ cannot be observed visually since so few photons return from this depth. Although there are several important processes taking place here, among other the kinetics of bilirubin diffusion from larger blood vessels, the processes seem invisible to an observer based on transport of radiation.

For skin type II and wavelengths of $490\,\text{nm}$, the penetration depth is sufficient to penetrate through all skin layers. The penetration depth is markedly smaller for jaundiced dermis than normal dermis. However, as the melanin content in the skin increases, the penetration depth decreases rapidly for this wavelength. For skin type V the penetration depth is slightly deeper than the epidermis, while for skin type VI the majority of the photons appear to be absorbed already in the epidermis so that they never reach the dermis. If the main part of the bilirubin is situated in the dermis as assumed, this reduction in penetration depth indicates that the dark skin types get substantially less effect from the same amount of phototherapy as the lighter skin types does.

5.3.2 Depth of bilirubin in skin

As the penetration depth is estimated based on optical parameters which differ between skin types and pigmentations, it is important to know the location of the bilirubin in the skin subject to phototherapy. This depth is currently not uniquely determined.

In section 3.3, the depth of bilirubin was approximated to $295\,\text{nm}$ by using the adult skin structure from Svaasand et al [122, 123] and assuming the infant skin structure to be similar but thinner. However, in an experiment conducted by Narendran et al in 2015 [77], bilirubin was found in both dermis and epidermis. The experiment aimed to prove that bilirubin binds *in vitro* to newborn skin, and used freshly sampled foreskin specimens to investigate the absorption of unconjugated bilirubin in infant skin when indirectly exposed to bilirubin molecules. The skin samples was placed dermis down, and the absorption of bilirubin therefore went upwards through the dermis. Narendran et al found in this experiment that the unconjugated bilirubin was present in both dermis and epidermis, particularly in the inner layer of the epidermis. The authors further discuss that the inner layer of the epidermis is the optimal location for presentation to blue light phototherapy, and hypothesises that the function of jaundiced skin is to protect the blood-brain barrier and to avoid kernicterus in the infants by making the unconjugated bilirubin more accessible to natural light [77]. However, as the experiment was performed *in vitro*, the circulation of blood was neglected. This exclusion may have substantial impact on the observed kinetics of unconjugated bilirubin compared to the behaviour *in vivo*.

The substantial differences in penetration depth for the different skin types as seen in table 4.6 indicates that the depth of bilirubin in the skin has great importance on the effect of phototherapy treatment. However, if other research verifies the experiments performed by Narendran et al, the reduction in penetration depth for higher concentrations of melanin in the epidermis will have a smaller effect on the efficacy of the treatment.

5.3.3 Effect of pigmentation

Melanin is present in the epidermis to protect the skin from adverse effects of short wavelength radiation. Melanin may be present in the skin both as constitutive pigmentation, which is the level of pigmentation in skin areas shielded from light, and the facultative pigmentation which is induced in the skin by direct exposure to radiation, specifically UV radiation [57]. This inducible pigmentation may be seen as immediate or delayed tanning, and the longest wavelength shown to elicit immediate pigment darkening is 470 nm [68]. This wavelength is well into the visible spectrum. Visible light has also been known to cause pigmentation in skin of darker skin types [112].

The amount of incident irradiation during phototherapy was shown by Lyngsnes Randeberg et al [68] to induce a pigment darkening in infants, shown by an increased melanin index. This result shows that infant skin changes during phototherapy. As the infant is treated for neonatal jaundice, the bilirubin concentration decreases and the fluence for wavelengths of 490 nm at a skin depth of 295 µm increases as in figure 4.21. However, if the same treatment induces a higher level of epidermal melanin content, the fluence will decrease as in figure 4.20. The processes of skin irradiated with visible light will then experience a trade-off in effect, where the irradiation penetrates more deeply in the dermis due to the lessening of the bilirubin concentrations but the epidermis absorbs more irradiation due to a higher melanin content. This trade-off will impact the effect of the treatment for long exposure times, as the pigmentation increases. The trade-off might also be more substantial for sunlight treatment, which has a higher content of short wavelengths than conventional phototherapy.

5.4 Amount of time necessary for treatment by sunlight exposure

The main topic of this thesis is the investigation of the possibility for treating neonatal jaundice with sunlight exposure in exchange for phototherapy. The treatment at St. Olavs Hospital has been assumed optimal, and the radiant exposure received from this treatment will be compared to radiant exposure from sunlight. To assess the possibility of using solar treatment, the required solar exposure time for the different locations throughout the year must be calculated. The risk associated with this exposure time must also be assessed, and the effect of different skin types must be considered. These calculations were performed in section 4.6.

Only the radiant exposure of the conventional phototherapy will be discussed in this section. Neither the spatial variability nor the effects of reflective curtains or a variable distance between the overhead unit and the infant will be discussed in reference to the treatment by sunlight exposure.

5.4.1 Calculating necessary exposure time for sunlight

The radiant exposure received by conventional phototherapy is denoted by D_{bil} and was calculated in equation (4.1). It is important to remember that the assumption of one specific exposure is not accurate, and cannot be numerically relied upon or given as a separate conclusion or result. The radiant exposures calculated in equation (4.1) and (4.2) are

only assumptions, which may give indications of the effect of phototherapy treatment, approximate the adverse effects and assess necessary exposure time to sunlight. The Norwegian guidelines are not necessarily the optimal regarding treatment of neonatal jaundice. It is simply the best option at this time, as it has not been possible to find any mention of radiant exposure concerning the treatment of neonatal jaundice.

The necessary sunlight exposure time to achieve a radiant exposure equal to D_{bil} are shown in table 4.7. These exposure times were much larger than expected. The possibility of using sunlight exposure as a substitute for phototherapy treatment is possibly life-saving, but a necessary exposure of several days with exposure from sunrise to sunset is not necessarily feasible. If a solar treatment were to be performed with equal procedure as a conventional phototherapy treatment, the infant would be lying outside for several hours at a time which would not necessarily be healthy due to adverse effects of radiation and other effects of exposure, e.g. thermal effects. There is a trade-off between the beneficial and possibly life-saving effect of the treatment for neonatal jaundice and the adverse effects.

It can be seen from table 4.7 that the geographical location has a great impact on the amount of days necessary to acquire the radiant exposure D_{bil} by sunlight exposure. For Dar es Salaam, which is close to the equator, the amount of days vary from just above 4 in the summer (December) to almost 6 in winter. For Kathmandu, situated at a latitude of about 30° N, the number of days vary from just above 4 to almost 8. During the most beneficial time of year, the amount of days required is lower in Kathmandu than Dar es Salaam. This effect might be due to the larger amount of sunlit hours during the day, and thus more time per day possible for treatment. It can be seen from table 4.3 and figures 4.10 and 4.11 that the irradiance is higher for Dar es Salaam in December than for Kathmandu in June, but the timing of the rising and setting of the sun is different.

Both Dar es Salaam and Kathmandu are locations where the mortality of neonatal jaundice is high, and where a solar treatment of the condition might be relevant. The sunlight exposure of infants at Østerås is not as relevant, and would have been substantially less effective than for lower latitudes. The average irradiance for Østerås as seen in figure 4.12 is substantially lower than for the other locations, and the necessary exposure time is likewise higher. Only in summer is the exposure time required at Østerås comparable to the other exposure times, and in winter the necessary exposure time is 16 times larger than in December for Kathmandu. For December in Dar es Salaam, the exposure time of winter at Østerås is almost 30 times higher. The main reason the exposure time at Østerås is comparable to the exposure times of the other locations during summer is the long duration of summer days.

For the erythema weighted radiant exposure per average day as seen in table 4.7, the variations are large between the locations and depend on the layer of ozone in the atmosphere at that locations. As may be seen in appendix G, the ozone layer is thicker towards the pole of the northern hemisphere, and this might account for the low amount of SED per day in Østerås, together with the lower solar irradiance. However, in both Kathmandu and Østerås, the levels of erythema weighted irradiation vary greatly, with the maximum value being more that 60 times the minimum value at Østerås and more than 3 times in Kathmandu. For Dar es Salaam the maximum value is only 1.5 times that of the minimal value, but the values in term of SED are higher on average than for the other locations.

5.4.2 Differentiating for skin types

As discussed in section 5.3.1, the radiation transport depends on skin type and pigmentation. For more pigmentation, the amount of irradiation penetrating the skin at a given depth becomes substantially smaller. This reduction was taken into account for table 4.9, where the days required to achieve D_{bil} by sunlight exposure is calculated for skin types II, IV, V and VI. Skin type II is assumed to be the skin type corresponding to the pigmentation of most Norwegian infants, and is thus considered the reference for the conventional phototherapy treatment.

In table 4.9, it can be seen that the exposure times calculated in table 4.7 increased substantially when scaled with the skin type. For skin type VI, the exposure times more than doubled when compared to skin type II. This result is important for the relevant populations comprising of darker skin types where the sunlight exposure treatment is relevant, for instance in Dar es Salaam. For sub-Saharan Africa, which includes Dar es Salaam, the ethnic groups are dominated by highly pigmented populations according to Lucas et al [67]. This term indicates a skin type of V or VI, which according to table 4.9 would require much longer exposure times. For sunlight treatment of infants by sunlight, a treatment plan should therefore include a determination of skin type to ensure that the infant receives adequate irradiation and is treated sufficiently to cure the neonatal jaundice.

It is important to stress that this calculation only gives indications, and may not be used for concluding remarks on account of results. The scaling of the exposure times directly on account of the simulated reduction in fluence for the assumed depth of bilirubin has too many uncertainties to be able to conclude with the resulting values. The uncertainties are among others the variations in skin type for infants and the large uncertainty of the satellite overpass data for which the average values of solar irradiance are based.

5.4.3 Exposure to UV radiation

There are substantial risks associated with exposure to sunlight, of which the largest is from exposure to UV radiation. The details of the risks are covered in section 2.7. The adverse effects of the absorbed irradiation depends on the radiant exposure and the skin type of the exposed skin, among other factors. As described in section 2.6, the different skin types react differently to the same amount of erythema weighted radiant exposure. In table 4.10, the MED values from UVB radiation for the different skin types is stated in units of both mJ/cm^2 and SED. The values in SED are chosen as the lowest range of the MED-inducing radiant exposure since the population in question is infants. Infants have thinner and more delicate skin than adults [99] and are recommended to stay away from all UV radiation for the first 6 months of life [94]. It may therefore be assumed that the infant skin will react at the lowest range of exposure.

The resulting MEDs for the six different skin types as a function of average day for all three locations are found in table 4.11. The ICNIRP guideline limits for UV radiant exposures which expresses no acute or long term effects are approximately $2-4$ times less than the values of the MED [126]. This reduction indicates that exposures of several MEDs may have both acute and long term effects on the general health and skin. For the calculated MEDs per day, it is apparent that the skin type may be considered important for the adverse effects of sunburn or erythema. The amount of daily MEDs are for instance 6 times as large for skin type I as for skin type VI in Dar es Salaam during December.

In locations with abundant sunlight, the exposure to UV radiation and the erythema weighted irradiation might often be comparable to the results of table 4.11. The adverse effects of the sunlight exposure may therefore be large compared to the beneficial effects. However, the acute condition of neonatal jaundice must be weighted against the future risk of skin cancer to determine whether the treatment is justified.

5.4.4 Validating exposure time by comparing spectra

To validate the exposure times calculated in table 4.7, the spectrum of the measured overhead phototherapy unit in units of spectral irradiance has been compared to the solar spectrum. The spectrum of the phototherapy unit was calculated as described in section 3.1.6, and the solar spectrum was taken from the atmospheric simulations with *libRadtran*. The results are displayed in appendix I.

The solar spectra has been investigated for all three locations and for times of both 08:00 in the morning and at noon for the 21^{st} of March, the 24^{th} of June, the 22^{nd} of September and the 22^{nd} of December. Both the unweighed spectra and the spectra weighed with the bilirubin action spectrum are displayed in appendix I. The magnitude of the solar spectra changes as a function of both time of day and day of year. As a general trend, the solar spectra in the morning are lower than the phototherapy spectrum, while the solar spectra at noon are larger than the phototherapy spectrum. However, the solar spectra are all of an order of magnitude directly comparable to the spectral irradiance of the phototherapy.

These comparisons substantiates the long exposure times necessary for a radiant exposure similar to D_{bil} from equation (4.1). While the noon irradiation is larger than the irradiance delivered from phototherapy, the irradiance from the phototherapy unit stays constant throughout the entire treatment. For the sunlight, the irradiance decreases until the solar zenith angle becomes larger than $90°$, which effectively cuts off the treatment potential. This decrease is seen in the comparisons for 08:00, as well as the form of the spectral irradiance curve for average days displayed in figures 4.10 to 4.12. It is not the irradiance from the sun which is the limiting factor and which causes the exposure times to lengthen, but the range of time where the sun is above the horizon.

5.4.5 Feasibility of sunlight exposure times

The results of the calculations in section 4.6 show clearly that it is possible to treat infants with neonatal jaundice with sunlight. However, if the treatment of neonatal jaundice by sunlight is to be feasible as well as possible, the adverse effects of the sunlight exposure must be manageable. The adverse effects of the sunlight for an exposure of several days will most likely induce painful erythema and sunburn, which in turn might lead to an increased risk of developing skin cancer. The feasibility of treatment by sunlight exposure depends on the severity of these adverse effects, and thus the exposure time of the end-point treatment plan.

However, the calculated exposure time necessary for the treatment of neonatal jaundice in section 5.4 does not agree with the exposure time used by Slusher et al [113] in Lagos, Nigeria, when they determined that the use of filtered sunlight phototherapy was non-inferior to conventional phototherapy. Conventional phototherapy was here defined equal to the definition of conventional phototherapy by the AAP [12], where irradiances can be

found in appendix D. On one hand, the sunlight used for the phototherapy was filtered with the filters described by Vreman et al [135] so that the infants were irradiated with a minimum amount of UV radiation. This reduction may make a day-long sunlight exposure for infants less likely to amount to serious risks to the infants. On the other hand, one day of sunlight phototherapy was determined to be an exposure of at least 5 hours. On average, the infants required 1.13 days of filtered sunlight phototherapy [115]. In addition, Slusher et al states that only five out of 243 infants needed more than four days of phototherapy, and all these infants were treated with conventional phototherapy [113].

Lagos, Nigeria, is located at $6°31'21''$ N and $3°22'31''$ E [37], which is comparable to the locations of Dar es Salaam when it comes to the length of day and solar irradiance as the latitude is mirrored on the equator. For Dar es Salaam, the average day length throughout the year is from 06:00 to 19:00, or 13 hours, according to figure 4.10. This length of day is more than double the length of the exposure time which accounted for one day of exposure in the experiment by Slusher et al [113]. However, there are more incoming irradiation during the midday period than during the rest of the day. In table 4.8, it can be seen that only two thirds of the incoming radiant exposure per day is found in the midday hours in Dar es Salaam. As Lagos is comparable to Dar es Salaam in geographical position, this result may be extrapolated to the solar conditions in Lagos.

The fact that the results from the randomized trial conducted by Slusher et al [113] showed that the filtered sunlight phototherapy with only five hours of exposure time per day was non-inferior to conventional therapy as defined by the AAP [12], suggests that the radiant exposure acquired by the infants during conventional phototherapy might be too high. It is not possible to ensure that the definitions of conventional phototherapy from the AAP is comparable to the phototherapy used in Norway, as the spectral irradiances cannot be compared. However, if the infants of skin type VI are treated successfully with a sufficiently lower exposure time than calculated, there should be cause to evaluate the radiant exposure received in conventional phototherapy to ensure that this radiant exposure is not larger than necessary and thus does not subject infants to higher risks than absolutely required.

The conventional phototherapy which the sunlight treatment is compared with, has a high degree of variability. In table 4.1, it can be seen that the highest measured irradiance is 5.6 times as high as the lowest measured irradiance for recommended phototherapy settings [90]. This variability indicates that there are large variations in the treatment of phototherapy. As solar irradiance is inherently dependent on chaotic atmospheric conditions, a considerable variability will also be found in sunlight treatment. However, a high degree of variability does not necessarily mean a lowering of phototherapeutic effect.

As in most medical applications, there exists no solution for the treatment of neonatal jaundice which guarantees a complete recovery for every case. All cases are individual, which is one of the reasons for the subjectivity detailed in the treatment guidelines [16, 90]. Both skin type and pigmentation of the infants vary substantially, and the optimal treatment for one infant might not be optimal for another. It may never be possible to create a treatment regime which will be optimal for all infants, even with clearer specifications of pigmentation. However, if a treatment regime for controlled exposure to sunlight to treat neonatal jaundice is going to be feasible, the adverse effects of the sunlight exposure need to be low enough so that the infants will not experience severe sunburn. Such sunburn would be painful and would increase the risk of developing skin cancer later in life.

5.5 Is sunlight a feasible treatment source of neonatal jaundice?

The first question is whether it is feasible to treat infants with neonatal jaundice with sunlight. The answer to this question is yes, with reservations. The calculations from section 5.4 show that the same radiant exposure delivered to the infants treated at St. Olavs Hospital may be found in sunlight, but that the exposure time must be lengthened considerably due to the limited amount of time with sunlight each day. The literature agrees with the calculations in that the treatment of neonatal jaundice by phototherapy is feasible and justified [109, 113, 115]. However, the calculated exposure times will most likely cause a substantial amount of adverse effects of painful erythema and sunburn, with increased risks of skin cancer later in life. The adverse effects decrease the feasibility of sunlight treatment considerably.

The second question is whether the existing guidelines for treatment of neonatal jaundice are sufficient for treatment of all skin types. The answer to this question is not necessarily. In all the guidelines investigated in this thesis, none mentions the differences of melanin content in infant skin. The discussion from section 5.3.1 indicates that there are large differences between the different skin types concerning the amount of fluence and penetration depth. However, this difference is based on melanin pigmentation which might be too high for infants, which in turn might cause lesser differences. For an optimal treatment of neonatal jaundice, where the infant is not irradiated longer than necessary and thus not exposed to more adverse effects than necessary, the pigmentation of the infant should be approximated before start of treatment.

The third question is whether treatment by sunlight is adequately efficient compared to conventional treatment. Slusher et al [113] has already indicated that this question may be answered affirmatively by showing that filtered sunlight phototherapy is non-inferior to the conventional phototherapy used. However, the exposure times used in this study were considerably less than the exposure times calculated in this thesis, in addition to the use of UV filters which decreased the adverse effects of erythema. For even shorter exposure times than calculated, the effects of erythema might be too large for sunlight treatment of an infant to be feasible without filtering. However, the required sunlight exposure times might decrease if the radiant exposure D_{bil} of conventional phototherapy was optimised. This decrease of exposure times may increase the efficiency of sunlight exposure. On the other hand, a limitation of the sunlight treatment of neonatal jaundice is that treatment may only be performed in sunlit hours. This limitation is not present with the conventional phototherapy, which is available throughout the night.

The fourth question is if sunlight treatment of neonatal jaundice is feasible in the investigated locations. For infants without any possibility of receiving conventional phototherapy, as may be the case in Dar es Salaam and Kathmandu, the calculations performed here might be included in further research for optimising a treatment plan using sunlight. Such a treatment plan might change according to environmental factors, such as day of year or geographical location. However, for infants with conventional phototherapy available, as in Østerås, the treatment with sunlight is not applicable or recommended due to the adverse risks of UV radiation.

If used correctly, a treatment plan for using sunlight for treatment of neonatal jaundice might save several thousands of infants which would otherwise have gone untreated. How-

ever, it is important that the solar treatment is as optimal as possible, and this optimisation requires further research.

5.6 Future research and development

There are several topics that need to be investigated before sunlight treatment of neonatal jaundice can be applied to infants. One of the most important fields is the optimal radiant exposure and exposure time for treating neonatal jaundice. As indicated by the disagreement of the calculations of required exposure time in Dar es Salaam and the observations of Slusher et al [113], the radiant exposure administered by conventional phototherapy might not be optimal. The other aspects of conventional phototherapy, for instance the spatial variability of the measured irradiance and the effects of reflective curtains, should also be research further with respect to applications for controlled sun exposure.

Fractional treatment has not been discussed in this thesis so far. However, Jährig et al observed that a fractional treatment with intermittent breaks of duration similar to the treatment period might be favoured when compared to continuous treatment, as cited by Roll and Christensen [58, 103]. The fractional treatment gives the infant a smaller total radiant exposure of radiation due to regular breaks, and will give the infant more time to bond with its parents. Tan [125] found in 1982 that the effect of the phototherapy treatment is greatest when the concentration of bilirubin in the skin is largest, which occurs when the infant has the highest degree of yellowing. This observation has later been substantiated by Hansen [42]. With an interruption in the phototherapy treatment, the isomerised bilirubin molecules closer to the skin surface will have time to diffuse back to the blood stream. Similarly, new unconjugated bilirubin molecules will diffuse from the blood to the skin and be able to benefit from the phototherapy. Another argument for the fractional treatment is that the tanning effect of the skin will be smaller, due to the pause in irradiation and melanin production. A lower degree of tanning will lessen the trade-off effect of the increased melanin and the decreased bilirubin on the skin, and keep the fluence rate and penetration depth as high as possible. Fractional treatment might be a natural part of using sunlight treatment as sunlight is variable through the day, and if the therapy is discontinued during the midday hours when the adverse effects are greatest.

However, before the treatment of neonatal jaundice can be optimally fractioned in light and dark periods, the kinetics of bilirubin in infant skin must be determined. This field is largely unknown, together with the resulting skin depth with the largest bilirubin concentration. A greater knowledge of the kinetics of bilirubin will also give information on the optimal areas of skin for isomerising bilirubin. The progress of yellowing for the jaundiced skin is often from the head to the torso and downwards [116], which indicates that the kinetics of bilirubin and skin may be different for different areas of skin.

A potential problem of using sunlight phototherapy as treatment for neonatal jaundice is the timing of the start of the treatment. Sunlight treatment of neonatal jaundice is only possible during sunlight hours, and if a severely jaundiced infant is diagnosed, the treatment must start at once [90]. One solution to this problem is lamps which may be used for night-time treatment of neonatal jaundice. Such a lamp was used in Nigeria by Slusher et al [113], and was required by 13% of the infants treated with filtered sunlight phototherapy. As a major challenge for treatment of neonatal jaundice in low-income

countries is a lack of electricity [91, 116], ordinary phototherapy lamps cannot be routinely used for this purpose. An alternative possibility is to create a new phototherapy lamp which is easier to maintain, and which may run on solar batteries that can be recharged during the day.

As mentioned in section 5.2.2, the ratio of beneficial to harmful irradiation increases for less transparent atmospheres [107]. Less transparent atmospheres include a greater degree of Mie scattering due to larger particles, which decreases the amount of adverse irradiation. This decrease would increase the safety of the solar exposure, while increasing the required exposure time. This increased exposure time should be calculated at a later time. A less transparent atmosphere would also increase the amount of diffuse irradiation compared to the direct irradiation. The effect of this increased amount of diffuse irradiation is not included in this thesis, and should be researched further.

Lastly, the importance of assessing correct skin types for infants is important. This issue was discussed in section 2.6.2, and is very important for the correct classification of the optimal treatment for infants of different ethnicities. As of today, the treatment of phototherapy is either general with the only differentiation whether the infant has additional risks or not due to ethnicity, or based on the skin type of the mother. This approach is not optimal, as infant skin differ from adult skin in several important aspects. More research on infant skin and its structure is needed before the optimal radiant exposure of phototherapy for treatment of neonatal jaundice may be accurately defined.

5.7 Limitations of the thesis

The scope of this thesis was defined in section 1.1. In this section, the limitations of this scope is briefly described. The main limitations are not discussing options for full-body shielding from the direct solar radiation, tilting of the infants towards the position of the sun, thermal effects of the solar exposure or other environmental aspects of the treatment with sunlight. These aspects are not included in the rest of the thesis because they deal with special cases and considerations. However, they are mentioned here as they might have substantial impact on the treatment of neonatal jaundice with sunlight exposure at a later time. The impact might be positive and make sunlight exposure safer and more efficient, or the impact might increase the adverse effects of the infant while exposed to the sunlight.

A way to decrease the adverse effects of the direct sunlight is to shield the infants from the most harmful irradiation. This harmful irradiation is mostly considered to by UV radiation and IR radiation. By using full-body shielding of infants when exposed to sunlight, some of the adverse effects of the incident irradiation might be removed. This shielding might either be performed by natural means, such as shade, or by artificial means. Vreman et al [135] states that an ideal sunlight phototherapy film might block UV radiation and IR radiation to protect the infant from adverse effects, transmit visible light in the appropriate wavelength range for treatment of neonatal jaundice and be visually transparent to facilitate visibility of the infants [135]. Such a film was used by Slusher et al [113–115] in their studies. Other shielding options might be materials which are more easily available, such as window-glass [109].

Natural means of shielding might also decrease the adverse effects of the sunlight. Such natural means might for instance include shade beneath trees or parasols. In shade,

the direct component of the sunlight is removed. As indicated in section 2.4.1, the ratio of beneficial to adverse effect of sunlight on neonatal jaundice increase with a decrease in the transparency of the atmosphere due to less UV irradiation. Such a decrease in transparency might be due to clouds or aerosols. When the transparency of the atmosphere is decreased, the amount of direct irradiation lessens while the amount of diffuse irradiation may increase. More research is required to determine the therapeutic effect of diffuse irradiation compared to direct irradiation when it comes to neonatal jaundice. If this research results in a beneficial effect of diffuse irradiation, the treatment of neonatal jaundice by solar exposure in areas of shade might be both safer and more efficient, as the amount of UV irradiation is lessened which decreases the risk of erythema.

As seen by figures 4.7 to 4.9, the amount of solar irradiation has a maximum value around noon and decreases towards zero as the sun approaches the horizon. This decrease in irradiation leads to a longer required exposure time for the infants. One measure that might have an effect on the decreased irradiance is tilting of the infants. This technique has been described by Gulin et al [39], and is used by Brun et al [17] to determine the amount of sunlight incident on patients which react strongly to sunlight exposure. In this research, the angle of the incoming solar irradiance is deemed important for the effect of the sunlight on the patients. This indicates that the angle of solar incidence for sunlight treatment of neonatal jaundice might be important.

An aspect that has not been mentioned in the thesis is the thermal effects on the infants of sunlight and sunlight exposure. As the sun emits radiation in the IR wavelength range, thermal effects of the sunlight should be accounted for when researching the adverse effect of sunlight exposure in infants. This thermal effect depends on the outdoor temperature, and whether the infants will be affected strongly by exposure to this temperature while displaying as much skin as possible. The thermal aspect was included by Slusher et al in their studies [113–115]. Hyperthermia, or body temperatures greatly above normal, were dealt with by placing the infants on wet towels or sheets to decrease their temperature. Hypothermia, or body temperatures greatly below normal, was dealt with by taking the infants inside or wrapping them in blankets until their temperature rose again. Hyperthermia appeared in 5% of the infants treated with filtered sunlight phototherapy, while hypothermia appeared in $< 1\%$ of the infants treated with filtered sunlight phototherapy [113].

Other environmental effects must also be taken into account when it comes to outdoors exposure of infants to assess the effect of the environmental factors on general health. One of these factors is the air quality, which was assessed in the Environmental Performance Index (EPI) [51]. The air quality measured in the EPI consist of exposure to fine particulate matter, nitrogen dioxide and household air quality, which might all lead to severe respiratory diseases and increase the mortality of the population. For Tanzania and Nepal, the locations of Dar es Salaam and Kathmandu, respectively, the air quality measured gives a score of 70.85 and 29.84 out of 100, respectively [51]. These values gives worldwide rankings of 132 and 177 out of a total 180 countries.

Air quality characterizes the hazard of breathing normally outside, and infants are especially vulnerable to respiratory diseases due to the immaturity of their lungs, immune system and brain [101]. Most findings from studies of connections between infant mortality and air pollution have shown that infants living in areas with high levels of particulate matter has a greater risk of mortality during the first year of life [101]. This mortality suggests that outdoors exposure to sunlight might have adverse effects on the general

health of the infant in areas with high air pollution, such as Dar es Salaam and Kathmandu. Further research is required to determine the trade-off between the potentially life-saving effect of sunlight treatment of neonatal jaundice and the adverse effects from environmental factors such as air quality.

Chapter 6

Conclusion

In this thesis, it has been investigated whether sunlight exposure might be feasible for treatment of neonatal jaundice in low-income countries.

The condition of neonatal jaundice has been described together with the incidence and potential consequences of the disease. Several guidelines for treatment of the condition has also been assessed.

The therapeutic irradiance of conventional phototherapy units at St. Olavs Hospital in Trondheim has been experimentally assessed. These results included spatial variance and local changes in environment. The treatment practices at St. Olavs Hospital was also compared to the Norwegian treatment guidelines. The solar irradiance at selected geographical locations were simulated using realistic atmospheric conditions from satellite overpass data. The impact of skin pigmentation and skin types on the outcome of phototherapy of neonatal jaundice were evaluated by Monte Carlo simulations of optical transport in skin.

The conventional phototherapy treatment performed at St. Olavs Hospital were compared to controlled sun exposures at the selected locations. The feasibility of controlled sun exposure as a treatment method for neonatal jaundice in low-income countries was discussed with basis in the assumed optimal treatment of conventional phototherapy.

The aim of this thesis was formulated as four questions, and these questions will now be answered.

1. Is it feasible to treat infants with neonatal jaundice with sunlight?

Yes, with reservations. The same radiant exposure received by infants at the neonatal ward at St. Olavs Hospital in Trondheim might be delivered from sun exposure. However, the exposure time for sunlight will be longer due to the shorter span of sunlight hours per day compared to the duration of conventional phototherapy. This longer exposure time might have great adverse effects of painful sunburn and increased risk of skin cancer. These adverse effects impact the feasibility of the sunlight treatment.

2. Are the existing treatment guidelines sufficient for all skin types?

Not necessarily. There are no mentions of skin type or ethnicities in the investigated guidelines. Simulations of infant skin indicate that there are large differences in delivered radiation for different amounts of constitutive melanin pigmentation at the assumed skin depth of bilirubin. However, the knowledge of the skin pigmentation of newborn are lacking, and if the pigmentation is less than assumed in this thesis the differences between skin types will decrease.

3. Is sunlight treatment adequately efficient compared to conventional treatment?
Perhaps. By comparing the calculations in this thesis to previous research, it is indicated that the radiant exposure received by conventional phototherapy at St. Olavs Hospital in Trondheim is higher than necessary as other studies show effect with lower exposures. By using controlled exposure to sunlight, the UV radiant exposure will be higher than for conventional phototherapy. If the optimal radiant exposure is lower than assumed however, and the infants might be treated with lower exposure times than calculated, the sunlight treatment might be as efficient as conventional treatment. However, sunlight therapy can only be administered in sunlight hours during the day.

4. Is sunlight therapy of neonatal jaundice feasible in the investigated locations?
For infants without access to conventional phototherapy treatment, as might be the case in Dar es Salaam and Kathmandu, the possibility of sunlight treatment might be life-saving and have a great impact. For infants with access to conventional phototherapy treatment, as in Østerås, the treatment plan might be optimised further. This optimisation might account for both skin type and pigmentation, and necessary radiant exposure for sufficient isomerising of bilirubin.

List of References

[1] Agati, G., Fusi, F., Donzelli, G. P., and Pratesi, R. (1993). Quantum yield and skin filtering effects on the formation rate of lumirubin. *Journal of Photochemistry and Photobiology, B: Biology*, 18:197–203.

[2] Alkholidi, A. G. and Altowij, K. S. (2014). *Contemporary Issues in Wireless Communications, Dr Mutamed Khatib (Ed.)*, chapter Free Space Optical Communications — Theory and Practices. Available from `http://www.intechopen.com/books/contemporary-issues-in-wireless-communications/free-space-optical-communications-theory-and-practices`.

[3] Allen, B. (2015). Atmospheric aerosols: What are they, and why are they so important? Downloaded from `https://www.nasa.gov/centers/langley/news/factsheets/Aerosols.html` at 13.11.2015.

[4] Andrews, D. G. (2010). *An Introduction to Atmospheric Physics*. Cambridge University Press, 2 edition.

[5] Arias, I. M., Johnson, L., and Wolfson, S. (1961). Biliary excretion of injected conjugated and unconjugated bilirubin by normal and gunn rats. *American Journal of Physiology*, 200(5):1091–1094.

[6] Arlettaz, R., Blumberg, A., Buetti, L., Fahnenstich, H., Mieth, D., and Roth-Kleiner, M. (2007). Assessment and treatment of jaundiced newborn infants 35 $^{0}/_{7}$ or more weeks of gestation. Downloaded from `http://www.neonet.ch/files/3014/2597/8492/2006_Bili-Empfehlungen_e_final.pdf` at 27.01.2016.

[7] Astner, S. and Anderson, R. R. (2004). Skin phototypes 2003. *Journal of Investigative Dermatology*, 122:xxx–xxxi.

[8] Barrington, K., Sankaran, K., and Canadian Paediatric Society Fetus and Newborn Committe (2007). Guidelines for detection, management and preprevent of hyperbilirubinemia in term and late preterm newborn infants. *Paediatrics & Child Health*, 12(Suppl B):1B–12B.

[9] Berberan-Santos, M. N. (1990). Beer's law revisited. *Journal of Chemical Education*, 67(9):757–759.

[10] Bernhard, G., Arola, A., Dahlback, A., Fioletov, V., Heikkilä, A., Johnsen, B., Koskela, T., Lakkala, K., Svendby, T., and Tamminen, J. (2015). Comparison of OMI UV observations with ground-based measurements at high northern latitudes. *Atmospheric Chemistry and Physics*, 15:7391–7412.

[11] Bhattarai, B. K., Kjeldstad, B., Thorseth, T. M., and Bagheri, A. (2007). Erythemal dose in Kathmandu, Nepal based on solar UV measurements from multichannel filter radiometer, its deviation from satellite and radiative transfer simulations. *Atmospheric Research*, 85(1):112–119.

[12] Bhutani, V. K. and THE COMMITTEE ON FETUS AND NEWBORN (2011). Phototherapy to prevent severe neonatal hyperbilirubinemi in the newborn infant 35 or more weeks of gestation. *Pediatrics*. doi:10.1542/peds.2011-1494.

[13] Bhutani, V. K., Zipursky, A., Blencowe, H., Khanna, R., Sgro, M., Ebbesen, F., Bell, J., Mori, R., Slusher, T. M., Fahmy, N., Paul, V. K., Du, L., Okolo, A. A., de Almeida, M.-F., Olusanya, B. O., Kumar, P., Cousens, S., and Lawn, J. E. (2013). Neonatal hyperbilirubinemia and rhesus disease of the newborn: incidence and impairment estimates for 2010 at regional and global levels. *Pediatric Research*, 74(s1):86–100.

[14] Biospherical Instruments Inc (2003). GUV-2511 ground based UV/PAR radiometer. Technical report, Biospherical Instruments Inc.

[15] Bohren, C. F. and Huffman, D. R. (1983). *Absorption and Scattering of Light by Small Particles*. John Wiley & Sons, Inc.

[16] Bratlid, D., Nakstad, B., and Hansen, T. W. N. (2011). National guidelines for treatment of jaundice in the newborn. *Acta Pædiatrica*, 100:499–505.

[17] Brun, A. (2015). Prediction of outdoor light intensity as a guidance in everyday life for patients with erythropoietic protoporphyria. In *31st Scientific and annual meeting of the Norwegian Society for Photobiology and Photomedicine (NOFFOF)*.

[18] Bruzell, E. M. (2003). *Phototherapy of newborns suffering from hyperbilirubinaemia - An experimental study*. PhD thesis, NTNU.

[19] Burgess, P. (2009). Variation in light intensity at different latitude and seasons, effects of cloud cover, and the amounts of direct and diffused light. In *Presentation to Continous Cover Forestry Group (CCFG) Scientific Meeting*. Downloaded from `http://www.ccfg.org.uk/conferences/downloads/P_Burgess.pdf` at 29.11.2015.

[20] Chandrasekhar, S. (1960). *Radiative Transfer*. Dover Publications.

[21] Christensen, T. (2000). "Non-Ionizing Radiation". Lecture notes Spring 2000 at the University of Oslo.

[22] Christensen, T., Amundsen, I., Kinn, G., and Kjeldstad, B. (1992). Phototherapy of newborns with hyperbilirubinemia in Norwegian hospitals. A study of phototherapy units and light conditions. Østerås: Norwegian Radiation Protection Authority. SIS report 1992:2(2).

[23] Christensen, T., Kinn, G., Granli, T., and Amundsen, I. (1994). Cells, bilirubin and light: formation of bilirubin photoproducts and cellular damage at defined wavelengths. *Acta Paediatrica*, 83:7–12.

[24] Christensen, T. and Nilsen, L. T. N. (2012). Guidelines for the use of optical radiation therapy in medical and cosmetic procedures. Veileder nr. 8. Østerås: Norwegian Radiation Protection Authority.

[25] Commission Internationale de L'Eclairage (1999). Erythema Reference Action Spectrum and Standard Erythema Dose, ISO 17166:1999/CIE S 007-1998. (Vienna: CIE).

[26] Cremer, R. J., Perryman, R. W., and Richard, D. H. (1958). Influence of light on the hyperbilirubinemia of infants. *Lancet*, 2:1094–1097.

[27] Devine, S. G., Harrison, S. L., and Buettner, P. G. (2008). Building capacity of maternity staff to discourage the use of sunlight therapy in the post-partum period and infancy. *Woman and Birth*, 21:107–111.

[28] Ebbesen, F., Agati, G., and Pratesi, R. (2003). Phototherapy with turquoise versus blue light. *ADC Fetal Neonatal*, 88:430–431.

[29] Eneh, A. U. and Ugwu, R. O. (2009). Perception of neonatal jaundice among women attending children out patient and immunization clinics of the UPTH Port Harcourt. *Nigerian Journal of Clinical Practice*, 12:187–191.

[30] Espy, P. (2014). FY3201 Atmospheric Physics. Lecture Notes Spring 2014 at NTNU.

[31] Ezeaka, C. V., Ugwu, R. O., Mukhtar-Yola, M., Ekure, E. N., and Olusanya, B. O. (2014). Pattern and predictors of maternal care-seeking practices for severe neonatal jaundice in Nigeria: a multi-centre survey. *BMC Health Services Research*, 14(192).

[32] Fitzpatrick, T. (1975). Soleil et peau. *Journal de Medecine Esthetique*, 2:33–34.

[33] Fitzpatrick, T. B. (1988). The validity and practicality of sun-reactive skin types I through VI. *Archives of Dermatology*, 124:849–871.

[34] Friebel, M. and Meinke, M. (2005). Determination of the complex refractive index of highly concentrated hemoglobin solutions using transmittance and reflectance measurements. *Journal of Biomedical Optics*, 10(6):064019.

[35] Gelsor, N., Stamnes, J. J., Øyvind Frette, and Hamre, B. (2016). Solar radiation energy on the Tibetan plateau. In *Norwegian Electro-Optics Meeting 2016*.

[36] Gesellschaft für Neonatologie und Pädiatrische Intensivmedizin (GNPI) (2015). Hyperbilirubinämie des neugeborenen – diagnostik und therapie. Downloaded from `http://www.awmf.org/uploads/tx_szleitlinien/024-007l_S2k_Hyperbilirubinaemie_Neugeborenen_Diagnostik_Therapie_2015-08.pdf` at 12.02.2016.

[37] Google (2015). Google maps. Downloaded from `maps.google.com` at 27.11.2015. All positions were individually searched for.

[38] Google (2016). Google maps. Downloaded from `maps.google.com` at 24.05.2016. All positions were individually searched for.

[39] Gulin, M., Vašak, M., and Baotić, M. (2013). Estimation of the global solar irradiance on tilted surfaces. In *17th International Conference on Electrical Drives and Power Electronics (EDPE 2013) (pp. 334-339).*

[40] Guruprasad, G., Chawla, D., Aggrawal, S., Narang, A., and Deorari, A. K. (2011). Management of neonatal hyperbilirubinemia. Downloaded from `http://www.technomedica.ru/site_files/docs/books/bilitest/Management%20of%20Neonatal%20Hyperbilirubinemia.pdf` at 12.02.2016.

[41] Hansen, F. V. (1993). Albedos. Report ARL-TR-57, Army Research Laboratory, U.S: Army Research Laboratory Battlefield Environment Directorate ATTN: AMSRL-BE-S White Sands Missile Range, NM 88002-5501.

[42] Hansen, T. W. R. (2005). Behandling av gulsott hos nyfødte. *Tidsskrift for Den Norske Legeforening*, 125:594–598.

[43] Harrison, S., Hutton, L., and Nowak, M. (2002). An investigation of professional advice advocating therapeutic sun exposure. *Australian and New Zealand Journal of Public Health*, 26(2):108–115.

[44] Harrison, S. L., Buettner, P. G., and MacLennan, R. (1999). Why do mothers still sun their infants? *Journal of Paediatrics and Child Health*, 35:296–299.

[45] Harrison, S. L., Devine, S. G., Saunders, V. L., Smith, A. D., Buettner, P. G., and Nowak, M. J. (2013). Changing the risky beliefs of post-partum women about therapeutic sun-exposure. *Woman and Birth*, 26:202–206.

[46] Haskell, R. C., Svaasand, L. O., Tsay, T.-T., Feng, T.-C., McAdams, M. S., and Tromberg, B. J. (1994). Boundary conditions for the diffusion equation in radiative transfer. *Journal of the Optical Society of America*, 11(10):2727–2741.

[47] Henyey, L. G. and Greenstein, J. L. (1941). Diffuse radiation in the galaxy. *Astrophysical Journal*, 93(213):70–83.

[48] Hertwich, E. (2015). The climate system - the physics of climate change. Lecture Notes Spring 2015 - TEP4220 Energy and Environmental Consequences.

[49] Honsberg, C. and Bowden, S. (2015). Motion of the sun. Downloaded from `http://www.pveducation.org/pvcdrom/properties-of-sunlight/motion-of-sun` at 07.12.2015.

[50] Horn, A. R., Kirsten, G. F., Kroon, S. M., Henning, P. A., Möller, G., Pieper, C., Adhikari, M., Cooper, P., Hoek, B., Delport, S., Nazo, M., and Mawela, B. (2006). Phototherapy and exchange transfusion for neonatal hyperbilirubinaemia. *South African Medical Journal*, 96(9):819–824.

[51] Hsu, A. et al (2016). 2016 Environmental Performance Index. New Haven, CT: Yale University. Available: `www.epi.yale.edu`.

[52] International Electrotechnical Commission (2009). Medical electrical equipment – Part 2-50: Particular requirements for the basic safety and essential performance of infant phototherapy equipment. Available from `https://webstore.iec.ch/publication/24701`.

[53] Iqbal, M. (1983). *An Introduction to Solar Radiation*. Academic Press.

[54] Jacques, S. (2010). Melanosome absorption coefficient. Downloaded from `http://omlc.org/spectra/melanin/mua.html` at 11.05.2016.

[55] Jagger, J. (1985). *Solar-UV actions on living cells*. Praeger Publishers.

[56] Jahan, S. et al (2016). Human development report 2015: Work for human development. Available from `http://hdr.undp.org/en/2015-report`.

[57] Jimbow, K., Quevedo Jr., W. C., Fitzpatrick, T. B., and Szabo, G. (1976). Some aspects of melanin biology: 1950–1975. *Journal of Investigative Dermatology*, 67(1):72–89.

[58] Jährig, D., Berck, A., Meisel, P., and Jährig, K. (1985). [calculation of the effect of phototherapy with reference to different irradiation variants. i. effect of therapy mode on the photoeffect]. *Kinderarztliche Praxis*, 53(4):171–175.

[59] Kaplan, M., Merlob, P., and Regev, R. (2008). Israel guidelines for the management of neonatal hyperbilirubinemia and prevention of kernicterus. *Journal of Perinatology*, 28:389–397.

[60] Kapoor, C. L. and Krishna Murti, C. R. (1973). Uptake and release of bilirubin by skin. *Biochemical Journal*, 136:35–43.

[61] Knudsen, A. and Brodersen, R. (1989). Skin colour and bilirubin in neonates. *Archives of Disease in Childhood*, 64:605–609.

[62] Krishnaswamy, A. and Baranoski, G. V. (2004). A biophysically-based spectral model of light interaction with human skin. *Computer Graphics Forum*, 23(3):331–340. DOI: 10.1111/j.1467-8659.2004.00764.x.

[63] Lamarsh, J. R. (1975). *Introduction to Nuclear Reactor Theory*. Addison-Wesley.

[64] Lamola, A. A. and Russo, M. (2014). Fluoresence excitation spectrum of bilirubin in blood: A model for the action spectrum for phototherapy of neonatal jaundice. *Photochemistry and Photobiology*, 90(2):294–296.

[65] Lilley, J. (2001). *Nuclear Physics - Principles and Applications*. John Wiley & Sons, Ltd.

[66] Lister, T., Wright, P. A., and Chappel, P. H. (2012). Optical properties of human skin. *Journal of Biomedical Optics*, 17(9):090901.

[67] Lucas, R. M., Norval, M., and Wright, C. Y. (2016). Solar ultraviolet radiation in Africa: a systematic review and critical evaluation of the health risks and use of photoprotection. *Photochemical & Photobiological Sciences*, 15(1):10–23.

[68] Lyngsnes Randeberg, L., Bruzell Roll, E., Norvang Nilsen, L. T., Christensen, T., and Svaasand, L. O. (2005). In vivo spectroscopy of jaundiced newborn skin reveals more than a bilirubin index. *Acta Pædiatrica*, 94(1):65–71.

[69] Mack, M. C., Tierney, N. K., Ruvolo Jr, E., Stamatas, G. N., Martin, K. M., and Kollias, N. (2010). Development of Solar UVR-Related Pigmentation Begins as Early as the First Summer of Life. *Journal of Investigative Dermatology*. Letter to the Editor.

[70] Maksic, I., Trollebø, A. K., and Bratlid, D. (2010). Hyperbilirubinemia in a cohort of infants in a normal newborn nursery (nnn). *Pediatric Research*, 68:482.

[71] Malaysia Health Technology Assessment Section (MaHTAS) (2015). Clinical practice guidelines: Management of neonatal jaundice. Downloaded from `http://www.acadmed.org.my/index.cfm?&menuid=67` at 12.02.2016.

[72] Matlab function written by Oddbjørn Grandum, based on Iqbal [53], p.X (2000). *solpos.m*. Østerås: Norwegian Radiation Protection Authority.

[73] Mayer, B. and Kylling, A. (2005). Technical note: The libradtran software package for radiative transfer calculations - description and examples of use. *Atmospheric Chemistry and Physics*, 2:1855–1877.

[74] Mayer, B., Kylling, A., Emde, C., Buras, R., Hamann, U., Gasteiger, J., and Richter, B. (2015). libradtran user's guide. Downloaded from `http://www.libradtran.org/doc/libradtran.pdf` at 30.08.2015.

[75] Ministry of Health (GNPD) Ghana (2010). Standard treatment guidelines. Downloaded from `http://apps.who.int/medicinedocs/documents/s18015en/s18015en.pdf` at 27.01.2016.

[76] Ministry of Medical Services and Ministry of Public Health and Sanitation (2009). Clinical guidelines for management and referral of common conditions at levels 2-3: Primary care. Downloaded from `http://chs.uonbi.ac.ke/sites/default/files/chs/chs/Clinical%20Guidelines%20Vol%20II%20Final.pdf` at 12.02.2016.

[77] Narendran, V., Pickens, W. L., Visscher, M. O., and Hoath, S. B. (2015). Neuroprotective core measure 6: Protecting skin - neuroprotective care in the newborn: Does skin protect the immature brain from hyperbilirubinemia? *Newborn & Infant Nursing Reviews*, 15:124–127.

[78] NASA Goddard space flight center (2016a). Aura atmospheric chemistry. Downloaded from `http://aura.gsfc.nasa.gov/about.html` at 25.04.2016.

[79] NASA Goddard space flight center (2016b). DATA/AURA/OMUVB. Downloaded from `http://avdc.gsfc.nasa.gov/index.php?site=2057856112&id=79` at 05.04.2016.

[80] National Institute for Health and Care Excellence (NICE) (2010). Jaundice in newborn babies under 28 days: Clinical guideline. Downloaded from `http://www.nice.org.uk/guidance/cg98/resources/`

jaundice-in-newborn-babies-under-28-days-975756073669at 12.02.2016.

[81] National Snow & Ice Data Center (2015). What is the arctic? Downloaded from https://nsidc.org/cryosphere/arctic-meteorology/arctic.html at 27.11.2015.

[82] Natus Newborn Care (2016). Jaundice management - neoBLUE® LED Phototherapy System. Downloaded from http://www.natus.com/index.cfm?page=products_1&crid=767 at 21.04.2016.

[83] Nave, C. R. (2010). Atomic spectra. Downloaded from http://hyperphysics.phy-astr.gsu.edu/hbase/quantum/atspect2.html at 21.05.2016.

[84] Nederlandse Vereniging voor Kindergeneeskunde (NVK) (2008). Richtlijn preventie, diagnostiek en behandeling van hyperbilirubinemie bij de pasgeborene, geboren na een zwangerschapsduur van meer dan 35 weken. Downloaded from http://www.nvk.nl/Portals/0/richtlijnen/hyperbili/richtlijnhyperbili.pdf at 12.02.2016.

[85] Neonatal ward, St. Olavs Hospital Trondheim (2015). Hyperbilirubinemi og lysbehandling. Nyfødt intensiv. Internal note on treatment of hyperbilirubinaemia.

[86] Newborn Services Clinical Guidelines (2012). Management of neonatal jaundice: Clinical guidelines. Downloaded from http://www.adhb.govt.nz/newborn/Guidelines/GI/Jaundice.htm at 27.01.2016.

[87] Nkhoma, E. T., Poole, C., Vannappagari, V., Hall, S. A., and Beutler, E. (2009). The global prevalence of glucose-6-phosphate dehydrogenase deficiency: A systematic review and meta-analysis. *Blood Cells, Molecules, and Diseases*, 42:267–278.

[88] Norman, M., Bruun, C. F., Karlsson, H., Sarman, I., Engberg, S., and Ewald, U. (2008). Neonatal hyperbilirubinemi. Downloaded from http://neoforeningen.se/dokument/vardprogram/hyperbili_2008.pdf at 12.02.2016.

[89] Norvang, L. T., Milner, T. E., Nelson, J. S. J. S., Berns, M. W., and Svaasand, L. O. (1997). Skin pigmentation characterized by visible reflectance measurements. *Lasers in Medical Science*, 12:99–112.

[90] Norwegian Pediatric Association (2006). Norsk veileder for behandling av gulsott hos nyfødte. Trondheim: St. Olavs Hospital.

[91] Olusanya, B. O., Imam, Z. O., Mabogunje, C. A., Emokpae, A. A., and Slusher, T. M. (2014a). Maternal satisfaction with a novel filtered-sunlight phototherapy for newborn jaundice in Southwest Nigeria. *BMC Pediatrics*, 14(180).

[92] Olusanya, B. O., Ogunlesi, T. A., Kumar, P., Boo, N.-Y., Iskander, I. F., de Almeida, M. F. B., Vaucher, Y. E., and Slusher, T. M. (2015). Management of late-preterm and term infants with hyperbilirubinaemia in resource-constrained settings. *BMC Pediatrics*, 15(39).

[93] Olusanya, B. O., Ogunlesi, T. A., and Slusher, T. M. (2014b). Why is kernicterus still a major cause of death and disability in low-income and middle-income countries? *Archives of Disease in Childhood*, 99:1117–1121.

[94] Paller, A. S., Hawk, J. L. M., Honig, P., Giam, Y. C., Hoath, S., Mack, M. C., and Stamatas, G. N. (2011). New insights about infant and toddler skin: Implications for sun protection. *Pediatrics*, 128(92):92–102.

[95] Pierluissi, J. H. and Peng, G.-S. (1985). New molecular transmission band models for LOWTRAN. *Optical Engineering*, 24(3):243541.

[96] Prahl, S. A., Keijzer, M., Jacques, S. L., and Welch, A. J. (1989). A Monte Carlo model of light propagation in tissue. *SPIE Institute Series*, IS 5:102–111.

[97] Queensland Maternity and Neonatal (2012). Queensland maternity and neonatal clinical guideline: Neonatal jaundice. Downloaded from `http://www.health.qld.gov.au/qcg/documents/g_jaundice.pdf` at 27.01.2016.

[98] Radium (2005). UV More than just light - Solutions in ultraviolet and infrared. Downloaded from `http://www.proflamps.com/datasheets/Radium.pdf` at 20.04.2016.

[99] Randeberg, L. L., Skallerud, B., Langlois, N. E., Haugen, O. A., and Svaasand, L. O. (2011). *Optical-Thermal Response of Laser-Irradiated Tissue*, chapter The Optics of Bruising, pages 825–858. Springer Netherlands.

[100] Ricchiazzi, P., Yang, S., Gautier, C., and Sowle, D. (1998). SBDART: A research and teaching software tool for plane-parallel radiative transfer in the earth's atmosphere. *Bulletin of the American Meteorological Society*, 79(10):2101–2114.

[101] Ritz, B. and Wilhelm, M. (2008). Air pollution impacts on infants and children. Southern California Environmental Report Card - Fall 2008, UCLA Institute of the Environment.

[102] Roll, E. B. (2005). Bilirubin-induced cell death during continous and intermittent phototherapy in the dark. *Acta Paediatrica*, 94:1437–1442.

[103] Roll, E. B. and Christensen, T. (1997). Phototherapy of hyperbilirubinemia in newborns; the need for a better treatment and follow-up. *Norwegian Journal of Epidemiology*, 7(1):93–98.

[104] Roll, E. B. and Christensen, T. (2005). Formation of photoproducts and cytotoxicity of bilirubin irradiated with turquoise and blue phototherapy light. *Acta Paediatrica*, 94:1448–1454.

[105] Romagnoli, C., Barone, G., Pratesi, S., Raimondi, F., Capasso, L., Zecca, E., and Dani, C. (2014). Italian guidelines for management and treatmens of hyperbilirubinaemia of newborn infants $\geq$ 35 weeks' gestation age. *Italian Journal of Pediatrics*, 40(11).

[106] Royal Meteorological Institute of Belgium (RMIB) (2015). Variability of the ozone layer. Downloaded from `http://ozone.meteo.be/meteo/view/en/1547952-Variability+of+the+ozone+layer.html` at 07.12.2015.

[107] Rønneberg, S., Randeberg, L. L., Nilsen, L. T. N., Goa, P. E., and Aune, A. (2015). Phototherapy with sunlight for treatment of neonatal jaundice in low-income countries. Project thesis, NTNU.

[108] Saidi, I. S., Jacques, S. L., and Tittel, F. K. (1995). Mie and Rayleigh modeling of visible-light scattering in neonatal skin. *Applied Optics*, 34(31):7410–7418.

[109] Salih, F. M. (2001). Can sunlight replace phototherapy units in the treatment of neonatal jaundice? an *in vitro* study. *Photodermatology, Photoimmunology and Photomedicine*, 17:272–277.

[110] Sarkar, R., Basu, S., Agrawal, R. K., and Gupta, P. (2010). Skin care for the newborn. *Indian Pediatrics*, 47:593–598.

[111] Schmalwieser, A. W., Wallisch, S., and Diffey, B. (2012). A library of action spectra for erythema and pigmentation. *Photochemical & Photobiological Sciences*, 11:251–268.

[112] Sklar, L. R., Almutawa, F., Lim, H. W., and Hamzavi, I. (2013). Effects of ultraviolet radiation, visible light, and infrared radiation on erythema and pigmentation: a review. *Photochemical & Photobiological Sciences*, 12(54):54–64.

[113] Slusher, T. M., Olusanya, B. O., Vreman, H. J., Brearley, A. M., Vaucher, Y. E., Lund, T. C., Wong, R. J., Emokpae, A. A., and Stevenson, D. K. (2015). A randomized trial of phototherapy with filtered sunlight in African neonates. *New England Journal of Medicine*, 373(12):1115–1124.

[114] Slusher, T. M., Olusanya, B. O., Vreman, H. J., Wong, R. J., Brearley, A. M., Vaucher, Y. E., and Stevenson, D. K. (2013). Treatment of neonatal jaundice with filtered sunlight in Nigerian neonates: study protocol of a non-inferiority, randomized controlled trial. *Trials*, 14(446).

[115] Slusher, T. M., Vreman, H. J., Olusanya, B. O., Wong, R. J., Brearley, A. M., Vaucher, Y. E., and Stevenson, D. K. (2014). Safety and efficacy of filtered sunlight in treatment of jaundice in African neonates. *Pediatrics*, 133(1568).

[116] Slusher, T. M., Zipursky, A., and Bhutani, V. K. (2011). Newborn need for affordable neonatal jaundice technologies. *Seminars in Perinatology*, 35:185–191.

[117] Solar Light (2016a). Data logging radiometer PMA2100. Datasheet, Solar LIght.

[118] Solar Light (2016b). Sensors - blue light safety detector PMA2121. Datasheet, Solar Light.

[119] Spott, T., Svaasand, L. O., Anderson, R. E., and Schmedling, P. F. (1997). Application of optical diffusion theory to transcutaneous bilirubinometry. *Proc. SPIE 3195, Laser-Tissue Interaction, Tissue Optics, and Laser Welding III*, pages 234–245.

[120] Spott, T. B. (1999). *Characterisation of layered tissue structures with diffusely propagating photon-density of wave*. PhD thesis, NTNU.

[121] Stokowsky, L. A. and Gracey, K. (2002). Newborn jaundice. *Advances in Neonatal Care*, 2(2):115–116.

[122] Svaasand, L. O., Fiskerstrand, E. J., Kopstad, G., Norvang, L. T., Svaasand, E. K., Nelson, J. S., and Berns, M. W. (1995a). Therapeutic response during pulsed laser treatment of port-wine stains: Dependence on vessel diameter and depth in dermis. *Lasers in Medical Science*, 10:235–243.

[123] Svaasand, L. O., Norvang, L. T., Fiskerstrand, E. J., Stopps, E. K. S., Berns, M. W., and Nelson, J. S. (1995b). Tissue parameters determining the visual appearance of normal skin and port-wine stains. *Lasers in Medical Science*, 10:55–65.

[124] Tan, K. L. (1975). Comparison of the effectiveness of single-direction and double-direction phototherapy for neonatal jaundice. *Pediatrics*, 56(4):550–553.

[125] Tan, K. L. (1982). The pattern of bilirubin response to phototherapy for neonatal hyperbilirubinaemia. *Pediatrics*, 16:670–674.

[126] The International Commision on Non-Ionizing Radiation Protection (2004). ICNIRP Guidelines on limits of exposure to ultraviolet radiation of wavelengths between 180 nm and 400 nm (incoherent optical radiation). *Health Physics*, 87(2):171–186.

[127] The International Commision on Non-Ionizing Radiation Protection (2010). ICNIRP Statement on protection of workers against ultraviolet radiation. *Health Physics*, 99(1):66–87.

[128] The International Commision on Non-Ionizing Radiation Protection (2013). ICNIRP Guidelines on limits of exposure to incoherent visible and infrared radiation. *Health Physics*, 105(1):74–96.

[129] The Norwegian Meteorological Institute and The Norwegian Broadcasting Corporation (2016). Weather statistics for Lhasa, Tibet (China). Downloaded from `http://www.yr.no/place/China/Tibet/Lhasa/statistics.html` at 05.06.2016.

[130] Thomas, G. E. and Stamnes, K. (1999). *Radiative Transer in the Atmosphere and Ocean*. Cambridge University Press.

[131] Timeanddate.com (2016). Time zone map. Downloaded from `http://www.timeanddate.com/time/map/` at 08.03.2016.

[132] Tønne, A., Meberg, A., and Hager, H. B. (2010). Endring i diagnostikk og behandling av hyperbilirubinemi hos nyfødte. *Tidskrift for Den norske legeforening*, 130:18–20.

[133] van Gemert, M. J., Jacques, S. L., Sterenborg, H. J., and Star, W. M. (1989). Skin optics. *IEEE Transactions on Biomedical Engineering*, 36(12):1146–1154.

[134] Vecchi, C., Donzelli, G. P., Miglorini, M. G., Sbrana, G., and Pratesi, R. (1982). New light in phototherapy. *Lancet*, 2(8294):390.

[135] Vreman, H. J., Slusher, T. M., Wong, R. J., Schultz, S., Olusanya, B. O., and Stevenson, D. K. (2013). Evaluation of window-tinting films for sunlight phototherapy. *Journal of Tropical Pediatrics*, 59(6):496–501.

[136] Wang, L. and Jacques, S. L. (2016). (MCML) Monte Carlo for Multi-Layered media. Downloaded from `http://omlc.org/software/mc/` at 28.04.2016.

[137] Wang, L., Jacques, S. L., and Zheng, L. (1995). MCML - Monte Carlo modeling og light transport in multi-layered tissues. *Computer Methods and Programs in Biomedicine*, 47:131–146.

[138] Wang, L., Jacques, S. L., and Zheng, L. (1997). CONV - convolution for response to a finite diameter photon beam incident on multi-layered tissues. *Computer Methods and Programs in Biomedicine*, 54:141–150.

[139] Wang, L. and Wu, H.-I. (2007). *Biomedical Optics - Principles and Imaging*. John Wiley & Sons, Inc.

[140] Webb, A. R., Slaper, H., Koepke, P., and Schmalwieser, A. W. (2011). Know your standard: Clarifying the CIE-Erythema Action Spectrum. *Photochemistry and Photobiology*, 87:483–486.

[141] Wikipedia (2016). Length of a degree of latitude. Downloaded from `https://en.wikipedia.org/wiki/Latitude#Length_of_a_degree_of_latitude` at 25.05.2016.

[142] World Health Organization (WHO) (2013). Pocket book of hospital care for children: guidelines for the management of common childhood illnesses. Downloaded from `http://apps.who.int/iris/bitstream/10665/81170/1/9789241548373_eng.pdf` at 27.01.16.

[143] Özkan, H., Ören, H., Duman, N., and Duman, M. (2003). Dermal bilirubin kinetics during phototherapy in neonates. *Acta Paediatrica*, 92:577–581.

List of Figures

List of Tables

Appendix A

Acronyms and abbreviations

AAP = American Academy of Pediatrics
BCC = Basal cell carcinoma
CIE = Commission Internationale de l'Éclairage
CM = Cutaneous melanoma
CMF = Cloud modification factor
EPI = Environmental Performance Index
ET = Exchange blood transfusion
G6PD = Glucose-6-phosphate dehydrogenase
GM = Gestational maturity
ICNIRP = International Commission on Non-Ionizing Radiation Protection
IEC = International Electrotechnical Commission
IR = Infrared
ISO = International Organization for Standardisation
MCML = Monte Carlo for Multi-Layered media
MED = Minimal erythemal dose
NASA = National Aeronautics and Space Administration
NTNU = Norwegian University of Science and Technology
RTE = Radiative transport equation
SCC = Squamous cell carcinoma
SED = Standard erythemal dose
TcB = Transcutaneous bilirubinometry
TOMS = Total ozone mapping spectroradiometer
TsB = Total serum bilirubin
UV = Ultraviolet
WHO = World Health Organization
WRC = World Radiation Calibration centre

Appendix B

Derivation of the general radiative transport equation

The full RTE is given by [139, p.88]

$$\frac{\partial L(\vec{r},\hat{s},t)/c}{\partial t} = -\hat{s}\cdot\nabla L(\vec{r},\hat{s},t) - \mu_t L(\vec{r},\hat{s},t) + \mu_s \int_{4\pi} L(\vec{r},\hat{s},t)P(\hat{s}'\cdot\hat{s})\,d\Omega' + S(\vec{r},\hat{s},t), \tag{B.1}$$

where $L(\vec{r},\hat{s},t)$ denotes the spatial and temporal dependent radiance. Equation (B.1) expresses the general RTE, and it is this general form that is derived in this section. Equation (B.1) is often called the Boltzmann equation [139, p.88].

There are several ways to derive the RTE. The approach given here [139] uses the principle of conservation of energy. This approach neglects the coherence, polarization and non-linearity of the radiation. The optical properties included are refractive index n, absorption coefficient μ_a, scattering coefficient μ_s and scattering anisotropy g. All optical properties are assumed to be space variant and time-invariant. Only elastic scattering is considered.

The derivation centers around a stationary differential cylindrical volume element as shown in figure B.1. The RTE is found by considering all possible contributions to the energy change in this cylindrical volume element within the specified solid angle $d\Omega$. The contributions are divergence, extinction, scattering and source, and all these contributions are taken into account when assessing the conservation of energy. The principle of conservation of energy gives that

$$dP = -dP_{\text{div}} - dP_{\text{ext}} + dP_{\text{sca}} + dP_{\text{src}}, \tag{B.2}$$

where each contribution is denoted as dP. Each contribution will be calculated separately before insertion in equation (B.2) to get equation (B.1).

Divergence

The divergence of a local photon beam is non-zero if the beam is not collimated. Energy diverging out of the volume element in question is given by

$$dP_{\text{div}} = \frac{\partial L(\vec{r},\hat{s},t)}{\partial s}\,ds\,dA\,d\Omega = \frac{\partial L(\vec{r},\hat{s},t)}{\partial s}\,d\Omega\,dV, \tag{B.3}$$

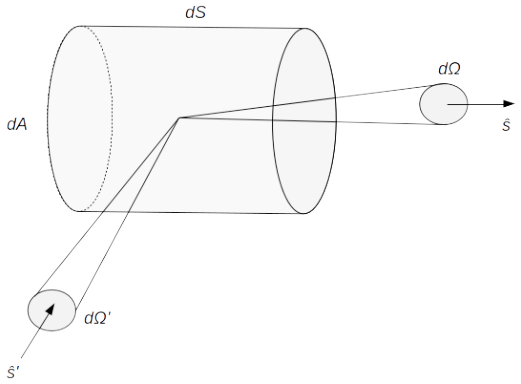

Figure B.1: Schematic of a stationary differential cylindrical volume element. dS is the differential length element along the propagation direction $\hat{s}$, dA is the differential area element perpendicular to $\hat{s}$, $d\Omega$ is the differential solid angle element around $\hat{s}$ and $d\Omega'$ is the differential solid angle element around $\hat{s}'$.

which in divergence form becomes

$$dP_{\text{div}} = \hat{s} \cdot \nabla L(\vec{r}, \hat{s}, t)\, d\Omega\, dV. \tag{B.4}$$

The divergence contribution is positive for actual divergence and negative for actual convergence. The contribution is due to local non-interactive beam propagation and can exist in a non-scattering medium. However, scattering elsewhere may affect the local divergence.

Extinction

Extinction denotes energy loss per unit time in the volume element within the solid angle. This energy loss is due to absorption and scattering, and is given by

$$dP_{\text{ext}} = (\mu_t ds)[L(\vec{r}, \hat{s}, t)\, dA\, d\Omega]. \tag{B.5}$$

Here, $\mu_t ds$ represents the probability of extinction by either absorption or scattering in ds, and μ_t is the extinction coefficient as defined in equation (2.8).

Scattering

The scattering contribution includes energy incident on the volume element from any direction $\hat{s}'$ and scattered into $d\Omega$ around direction $\hat{s}$ per unit time. This contribution is given by

$$dP_{\text{sca}} = (N_s\, dV) \left[\int_{4\pi} L(\vec{r}, \hat{s}, t) P(\hat{s}', \hat{s}) \sigma_s\, d\Omega' \right] d\Omega, \tag{B.6}$$

where N_s is the number density of scatterers and σ_s is the scattering cross section, which means that $N_s dV$ is the number of scatterers in the volume element. Inside the integral, $L(\vec{r}, \hat{s}, t)\sigma_s\, d\Omega'$ denotes the energy intercepted by a single scatterer within solid angle $d\Omega'$ per unit angle. $P(\hat{s}', \hat{s})$ is the phase function.

According to the theory of the phase function, $P(\hat{s}', \hat{s})$ is only dependent on the angle between the scattered and incident directions, which gives $P(\hat{s}' \cdot \hat{s})$. The scattering

anisotropy can then be expressed as

$$g = \int_{4\pi} (\hat{s}' \cdot \hat{s}) P(\hat{s}' \cdot \hat{s})\, d\Omega. \tag{B.7}$$

By using the fact that the scattering coefficient is given by $\mu_s = N_s \sigma_s$ together with the angular dependence of the phase function, equation (B.6) can be rewritten as

$$dP_{\text{sca}} = (\mu_s dV) \left[\int_{4\pi} L(\vec{r}, \hat{s}, t) P(\hat{s}' \cdot \hat{s})\, d\Omega' \right] d\Omega. \tag{B.8}$$

This equation is the scattering contribution.

Source

The source contribution account for energy produced within the volume element within the solid angle element per unit time. This contribution is given as

$$dP_{\text{src}} = S(\vec{r}, \hat{s}, t)\, dV\, d\Omega, \tag{B.9}$$

where S has unit of W/(m^3 sr).

Conservation of energy

The total change of the energy in the volume element within the solid angle element per unit time is given by

$$dP = \frac{\partial L(\vec{r}, \hat{s}, t)/c}{\partial t}\, dV\, d\Omega. \tag{B.10}$$

Here, $L(\vec{r}, \hat{s}, t)/c$ represents the propagating energy per unit volume per unit solid angle. The rate of change from equation (B.2) is a result of the energy balance from the four contributions listed previously, with two negative and two positive.

The principle of conservation of energy is given in equation (B.2). To get the RTE from equation (B.1), equations (B.4), (B.5), (B.8), (B.9) and (B.10) is substituted into equation (B.2). This substitution gives

$$\begin{aligned} \frac{\partial L(\vec{r}, \hat{s}, t)/c}{\partial t}\, dV\, d\Omega = &- \hat{s} \cdot \nabla L(\vec{r}, \hat{s}, t)\, d\Omega\, dV - (\mu_t ds)[L(\vec{r}, \hat{s}, t)\, dA\, d\Omega] \\ &+ (\mu_s dV) \left[\int_{4\pi} L(\vec{r}, \hat{s}, t) P(\hat{s}' \cdot \hat{s})\, d\Omega' \right] d\Omega + S(\vec{r}, \hat{s}, t)\, dV\, d\Omega, \end{aligned}$$

and dividing by $dV\, d\Omega$ gives

$$\begin{aligned} \frac{\partial L(\vec{r}, \hat{s}, t)/c}{\partial t} = &- \hat{s} \cdot \nabla L(\vec{r}, \hat{s}, t) - \mu_t L(\vec{r}, \hat{s}, t) \\ &+ \mu_s \int_{4\pi} L(\vec{r}, \hat{s}, t) P(\hat{s}' \cdot \hat{s})\, d\Omega' + S(\vec{r}, \hat{s}, t). \end{aligned}$$

This expression is equivalent to the full RTE in equation (B.1).

A special case of the RTE equation is for time-independent responses. For this case, the transport of energy is in a steady-state, and the same amount of energy is received

and emitted by the volume element. As the energy in the volume element is constant as a function of time, the left-hand side of the RTE becomes zero so that

$$\frac{\partial L(\vec{r}, \hat{s}, t)/c}{\partial t} = 0. \tag{B.11}$$

To reach such a time-independent state requires the use of a time-invariant light source. The sun may be approximated as such a radiation source.

Appendix C

Details of the MCML program

The MCML program is a method of numerical simulation of multi-layered tissue, as explained in section 2.5.4. In this appendix, the details of the MCML program are presented based on Prahl et al [96]. A flowchart describing the process of the program can be seen in figure 2.10.

Photon movement and stepsize

The photon is either launched with an initial direction downwards into the tissue, or chosen randomly from all possible directions in the downward hemisphere. The latter is for simulation of diffuse irradiation. The propagating distance is chosen as a variable stepsize given by

$$\Delta s = \frac{-\ln \xi}{\mu_t}, \tag{C.1}$$

where ξ is a random variable uniformly distributed between 0 and 1. The probability density function of Δs from equation (C.1) will follow Beer's law from equation (2.6). The photon is moved in the three-dimensional space by using Cartesian coordinates, so that

$$\begin{aligned} x' &= x + \alpha_x \Delta s, \\ y' &= y + \alpha_y \Delta s, \\ z' &= z + \alpha_z \Delta s, \end{aligned} \tag{C.2}$$

where the new coordinates (x', y', z') is found by travelling a distance Δs in the direction $(\alpha_x, \alpha_y, \alpha_z)$ from start position (x, y, z). Here, $(\alpha_x, \alpha_y, \alpha_z)$ denotes the direction cosines, and is the cosine of the angle that the photon's direction makes with each axis.

Internal reflection, absorption, scattering and termination

When the photon encounters a boundary with a different index of refraction n, as for instance when entering another layer in the simulation or exiting the material during Δs, there is a possibility of internal reflection. The probability that a given photon will encounter internal reflection is determined by the Fresnel reflection coefficient from equation (2.34). If a random number ξ between 0 and 1 is found, and ξ is such that $\xi < R(\theta_i)$, then the photon is internally reflected. Otherwise, the photon exits the tissue.

The absorption of the MCML program is treated as a continuous process where a fraction of the photon is absorbed during each propagation. This continuous treatment

ensures that the correct absorption probability is related. The assigned weight of a photon is important when determining if the photon is fully absorbed or not. This weight is assigned to the photon as it enters the tissue, and for each propagation step, a fraction of the photon is absorbed and the rest is scattered. The fraction of absorption is given by

$$\frac{\mu_a}{\mu_a + \mu_s} = 1 - \frac{\mu_s}{\mu_a + \mu_s} = 1 - a,$$

where a denotes the single particle albedo which is the scattering coefficient divided by the extinction coefficient. The new photon weight ω' after scattering is thus given by $\omega' = a\omega$. The albedo mentioned here is analogous to the definition of the atmospheric albedo described in section 2.4.1.

The scattering of a photon is described by the azimuthal and longitudinal angles, ϕ and θ respectively, which are in turn described by a normalized phase function. The phase function normally has no azimuthal dependence, which means that ϕ is uniformly distributed over the interval $[0, 2\pi]$. As such, the azimuthal angle can be written as $\phi = 2\pi\xi$, where ξ is a random number between 0 and 1. Scattering in tissue is often described with the Henyey-Greenstein phase function of equation (2.17), which gives the longitudinal angle of

$$\cos\theta = \frac{1}{2g}\left(1 + g^2 - \left[\frac{1 - g^2}{1 - g + 2g\xi}\right]^2\right). \tag{C.3}$$

If the distribution is isotropic and $g = 0$, the longitudinal angle becomes $\cos\theta = 2\xi - 1$. The scattering angles in all direction can be computed further by formulas given by Prahl et al in [96], which details this derivation further.

For the photon packet to be terminated, the first check is whether the weight is below a certain minimum weight. A technique called roulette is used to terminate a photon without absorbing or discarding the remaining weight, as such actions would skew the absorption profile or violate the conservation of energy. The roulette gives a photon beneath the weight limit a specific probability of surviving, or else its weight is reduced to zero.

Calculating fluence rate

The fluence rate Φ may be simulated for any irradiation profile by letting the launched photons be spatially distributed following the irradiation profile. However, this spatial distribution greatly increases the number of photons needed to minimize the statistical error, and thus the simulation time. Fortunately, it turns out that the fluence rate which results from the photons launched at a single point corresponds to the Green's function of the medium, given by G. The fluence rate for an arbitrary irradiation profile may thus be obtained by convolving the Green's function profile with the irradiation source function S, which gives that

$$\Phi(x, y, z) = G(x, y, z) * S(x, y) = \int_{-\infty}^{+\infty}\int_{-\infty}^{+\infty} G(x', y', z)S(x - x', y - y')\,dx'\,dy'. \tag{C.4}$$

Here, $\Phi(x, y, z)$ is the fluence rate at point (x, y, z), and the convolution is independent of z because the irradiation source profile is not a function of depth.

The fluence F can be calculated from the fluence rate by using the definitions in section 2.1.

Appendix D

Overview of national guidelines for treatment of neonatal jaundice

There are several different guidelines for treatment of neonatal jaundice. These guidelines are often connected to nationality. In this appendix, the national guidelines which have been included in this thesis are listed in table D.1. This table contains a total of 18 different national guidelines. For help in finding different national guidelines, the appendices created by Olusanya et al [92] and Bratlid et al [16] were used.

Table D.2 state whether the different guidelines mention the spectrum or irradiance of the phototherapy, and whether sunlight exposure is mentioned.

Country	**URL**
Australia [97]	http://www.health.qld.gov.au/...
Canada [8]	http://www.cps.ca/...
Germany [36]	http://www.awmf.org/...
Ghana [75]	http://apps.who.int/...
India [40]	http://www.technomedica.ru/...
Israel [59]	http://www.nature.com/...
Italy [105]	http://www.ijponline.net/...
Kenya [76]	http://chs.uonbi.ac.ke/...
Malaysia [71]	http://www.acadmed.org.my/...
The Netherlands [84]	http://www.nvk.nl/...
New Zealand [86]	http://www.adhb.govt.nz/...
Norway [16]	http://onlinelibrary.wiley.com/...
South Africa [50]	http://www.paeds.co.za/...
Sweden [88]	http://neoforeningen.se/...
Switzerland [6]	http://www.neonet.ch/...
United Kingdom [80]	http://www.nice.org.uk/...
USA [12]	http://pediatrics.aappublications.org/...
World Health Organization (WHO) [142]	http://apps.who.int/...

Table D.1: Different national standards for treatment of neonatal jaundice together with source reference and the URL where they can be found. The full URL is stored as hyperlink.

Country	**Irradiance**	**Wavelength range**	**Sunlight (Yes/No)**
Australia	*Conventional*: $8 - 10$μW/cm^2/nm, *Intensive*: ≥ 30 μW/cm^2/nm	*Conventional*: $430-490$ nm, *Intensive*: $460 - 490$ nm	No
Canada	> 30 μW/cm²/nm	Blue-green spectrum	–
Germany[a]	30 μW/cm²/nm	$430 - 490$ nm	–
Ghana	–	–	Yes
India	–	–	–
Israel	–	–	–
Italy	> 35 μW/cm²/nm	–	–
Kenya	–	–	–
Malaysia	*Conventional*: ≥ 15 μW/cm^2/nm, *Intensive*: ≥ 30 μW/cm^2/nm	$400 - 500$ nm	No
The Netherlands[a]	30 μW/cm²/nm	$430 - 490$ nm	–
New Zealand[b]	$5 - 10$mcw/nm/cm^2	–	–
Norway	≥ 20 μW/cm²/nm	–	–
South Africa	≥ 30 μW/cm²/nm	$430 - 490$ nm	–
Sweden	–	450 nm	–
Switzerland	–	–	–
United Kingdom	–	–	No
USA	≥ 30 μW/cm²/nm	$460 - 490$ nm	–
WHO	–	–	–

Table D.2: A summary of the views of the different guidelines on level of irradiance, wavelength range, and whether sunlight is recommended as treatment or not. Guidelines where a topic is not mentioned is denoted by –.
a: The summary of standards from Germany and the Netherlands are not complete due to the fact that these standards only existed in the native language and not English.
b: The standard from New Zealand operates with the unit of mcw/nm/cm^2*, which may or may not be equivalent to* μW/cm²/nm*.*

Appendix E

Dates and days of year

libRadtran-simulations corrects for the solar orbit by including the the number of day in one year. This appendix contains tables showing the corresponding dates and day of the year for reference. The tables are displayed in table E.1 and E.2, for the first and second halves of the year. The tables are based on a year with 365 days, such as 2015.

1	Jan 01	32	Feb 01	60	Mar 01	91	Apr 01	121	May 01	152	Jun 01
2	Jan 02	33	Feb 02	61	Mar 02	92	Apr 02	122	May 02	153	Jun 02
3	Jan 03	34	Feb 03	62	Mar 03	93	Apr 03	123	May 03	154	Jun 03
4	Jan 04	35	Feb 04	63	Mar 04	94	Apr 04	124	May 04	155	Jun 04
5	Jan 05	36	Feb 05	64	Mar 05	95	Apr 05	125	May 05	156	Jun 05
6	Jan 06	37	Feb 06	65	Mar 06	96	Apr 06	126	May 06	157	Jun 06
7	Jan 07	38	Feb 07	66	Mar 07	97	Apr 07	127	May 07	158	Jun 07
8	Jan 08	39	Feb 08	67	Mar 08	98	Apr 08	128	May 08	159	Jun 08
9	Jan 09	40	Feb 09	68	Mar 09	99	Apr 09	129	May 09	160	Jun 09
10	Jan 10	41	Feb 10	69	Mar 10	100	Apr 10	130	May 10	161	Jun 10
11	Jan 11	42	Feb 11	70	Mar 11	101	Apr 11	131	May 11	162	Jun 11
12	Jan 12	43	Feb 12	71	Mar 12	102	Apr 12	132	May 12	163	Jun 12
13	Jan 13	44	Feb 13	72	Mar 13	103	Apr 13	133	May 13	164	Jun 13
14	Jan 14	45	Feb 14	73	Mar 14	104	Apr 14	134	May 14	165	Jun 14
15	Jan 15	46	Feb 15	74	Mar 15	105	Apr 15	135	May 15	166	Jun 15
16	Jan 16	47	Feb 16	75	Mar 16	106	Apr 16	136	May 16	167	Jun 16
17	Jan 17	48	Feb 17	76	Mar 17	107	Apr 17	137	May 17	168	Jun 17
18	Jan 18	49	Feb 18	77	Mar 18	108	Apr 18	138	May 18	169	Jun 18
19	Jan 19	50	Feb 19	78	Mar 19	109	Apr 19	139	May 19	170	Jun 19
20	Jan 20	51	Feb 20	79	Mar 20	110	Apr 20	140	May 20	171	Jun 20
21	Jan 21	52	Feb 21	80	Mar 21	111	Apr 21	141	May 21	172	Jun 21
22	Jan 22	53	Feb 22	81	Mar 22	112	Apr 22	142	May 22	173	Jun 22
23	Jan 23	54	Feb 23	82	Mar 23	113	Apr 23	143	May 23	174	Jun 23
24	Jan 24	55	Feb 24	83	Mar 24	114	Apr 24	144	May 24	175	Jun 24
25	Jan 25	56	Feb 25	84	Mar 25	115	Apr 25	145	May 25	176	Jun 25
26	Jan 26	57	Feb 26	85	Mar 26	116	Apr 26	146	May 26	177	Jun 26
27	Jan 27	58	Feb 27	86	Mar 27	117	Apr 27	147	May 27	178	Jun 27
28	Jan 28	59	Feb 28	87	Mar 28	118	Apr 28	148	May 28	179	Jun 28
29	Jan 29			88	Mar 29	119	Apr 29	149	May 29	180	Jun 29
30	Jan 30			89	Mar 30	120	Apr 30	150	May 30	181	Jun 30
31	Jan 31			90	Mar 31			151	May 31		

Table E.1: Overview of the first 181 *days of each year, with corresponding date in month and day. Based on non leap years.*

182	Jul 01	213	Aug 01	244	Sep 01	274	Oct 01	305	Nov 01	335	Dec 01
183	Jul 02	214	Aug 02	245	Sep 02	275	Oct 02	306	Nov 02	336	Dec 02
184	Jul 03	215	Aug 03	246	Sep 03	276	Oct 03	307	Nov 03	337	Dec 03
185	Jul 04	216	Aug 04	247	Sep 04	277	Oct 04	308	Nov 04	338	Dec 04
186	Jul 05	217	Aug 05	248	Sep 05	278	Oct 05	309	Nov 05	339	Dec 05
187	Jul 06	218	Aug 06	249	Sep 06	279	Oct 06	310	Nov 06	340	Dec 06
188	Jul 07	219	Aug 07	250	Sep 07	280	Oct 07	311	Nov 07	341	Dec 07
189	Jul 08	220	Aug 08	251	Sep 08	281	Oct 08	312	Nov 08	342	Dec 08
190	Jul 09	221	Aug 09	252	Sep 09	282	Oct 09	313	Nov 09	343	Dec 09
191	Jul 10	222	Aug 10	253	Sep 10	283	Oct 10	314	Nov 10	344	Dec 10
192	Jul 11	223	Aug 11	254	Sep 11	284	Oct 11	315	Nov 11	345	Dec 11
193	Jul 12	224	Aug 12	255	Sep 12	285	Oct 12	316	Nov 12	346	Dec 12
194	Jul 13	225	Aug 13	256	Sep 13	286	Oct 13	317	Nov 13	347	Dec 13
195	Jul 14	226	Aug 14	257	Sep 14	287	Oct 14	318	Nov 14	348	Dec 14
196	Jul 15	227	Aug 15	258	Sep 15	288	Oct 15	319	Nov 15	349	Dec 15
197	Jul 16	228	Aug 16	259	Sep 16	289	Oct 16	320	Nov 16	350	Dec 16
198	Jul 17	229	Aug 17	260	Sep 17	290	Oct 17	321	Nov 17	351	Dec 17
199	Jul 18	230	Aug 18	261	Sep 18	291	Oct 18	322	Nov 18	352	Dec 18
200	Jul 19	231	Aug 19	262	Sep 19	292	Oct 19	323	Nov 19	353	Dec 19
201	Jul 20	232	Aug 20	263	Sep 20	293	Oct 20	324	Nov 20	354	Dec 20
202	Jul 21	233	Aug 21	264	Sep 21	294	Oct 21	325	Nov 21	355	Dec 21
203	Jul 22	234	Aug 22	265	Sep 22	295	Oct 22	326	Nov 22	356	Dec 22
204	Jul 23	235	Aug 23	266	Sep 23	296	Oct 23	327	Nov 23	357	Dec 23
205	Jul 24	236	Aug 24	267	Sep 24	297	Oct 24	328	Nov 24	358	Dec 24
206	Jul 25	237	Aug 25	268	Sep 25	298	Oct 25	329	Nov 25	359	Dec 25
207	Jul 26	238	Aug 26	269	Sep 26	299	Oct 26	330	Nov 26	360	Dec 26
208	Jul 27	239	Aug 27	270	Sep 27	300	Oct 27	331	Nov 27	361	Dec 27
209	Jul 28	240	Aug 28	271	Sep 28	301	Oct 28	332	Nov 28	362	Dec 28
210	Jul 29	241	Aug 29	272	Sep 29	302	Oct 29	333	Nov 29	363	Dec 29
211	Jul 30	242	Aug 30	273	Sep 30	303	Oct 30	334	Nov 30	364	Dec 30
212	Jul 31	243	Aug 31			304	Oct 31			365	Dec 31

Table E.2: Overview of the second 184 *days of each year, with corresponding date in month and day. Based on non leap years.*

Appendix F

Results from measurement of spectrum and irradiance in phototherapy units

F.1 Calibrations

The radiometer with the probe corresponding to the blue light hazard spectral weighting was calibrated by using a calibration source with a set-up as described in figure 3.5. The spectrum of this calibration source can be seen in figure F.1. The correction factor between the bilirubin action spectrum [64] and the blue light hazard spectral weighting function, $B(\lambda)$ [128], denoted by C_{corr} from equation (3.2), was then found by weighting the spectrum from the overhead phototherapy unit with both spectra. This weighting is shown in figure F.2.

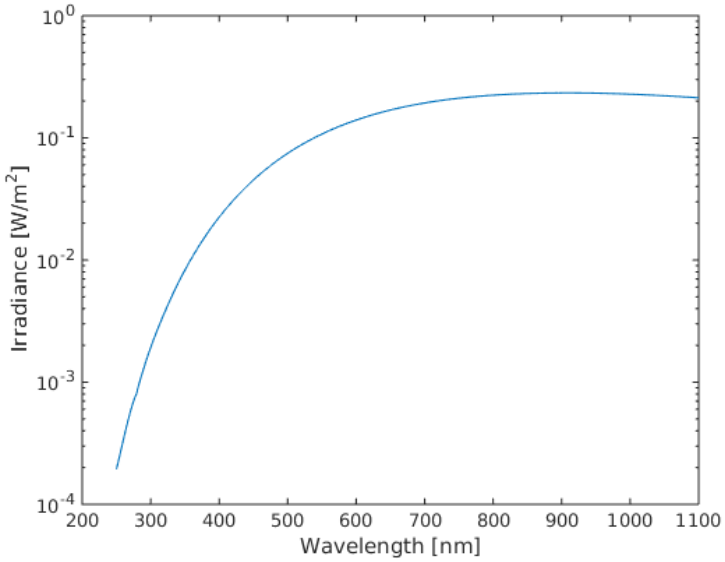

Figure F.1: The spectrum of the calibration radiation source used for calibrating the radiometer together with the blue light hazard probe. Note the logarithmic scale on the second axis.

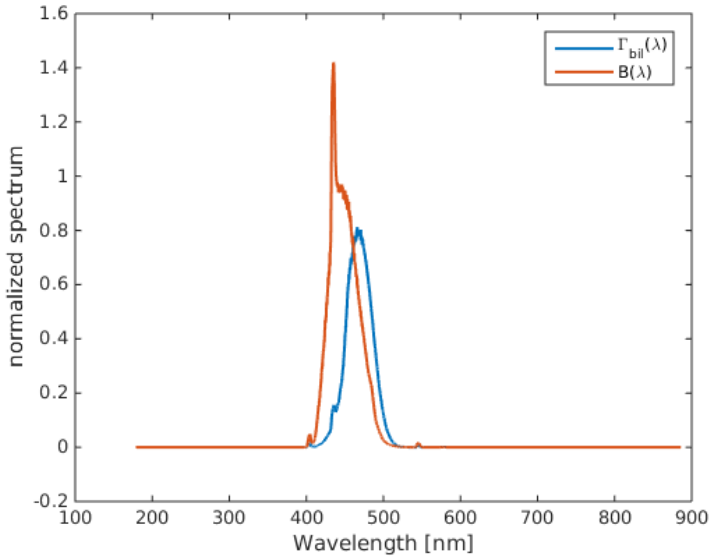

Figure F.2: The results of weighting the spectrum of the overhead phototherapy unit with both the bilirubin action spectrum $\Gamma_{bil}(\lambda)$ and the blue light hazard spectral weighting function $B(\lambda)$.

F.2 Spectra

The spectra of the phototherapy units at St. Olavs Hospital were measured both separately and together. The overhead unit had three different settings that determined which of the fluorescent lamps were switched on, and a comparison of the spectra for the different settings can be seen in figure F.3. The spectrum of the overhead unit together with the spectrum of the BiliBed mattress, which irradiates the infant from underneath, can be seen in figure F.4. Figures F.3 and F.4 show that the fluorescent lamps in both units are of the same type, as the spectra are identical in shape.

F.3 Irradiances

The irradiance of both types of phototherapy unit were measured both with and without reflective curtains. In the case of the overhead unit, the irradiance was also measured for four different distances between the infant and the unit. Selected results for the recommended use of the units are shown in section 4.1, while values from all measurement series are detailed here. The full dataset of all measurement series together with surface plots of all the measurement series and comparative plots are included in the digital appendix.

In table F.1, the maximum and minimum values of all the measurement series are shown. In table F.2, the average values of all measurement series for the overhead phototherapy unit are shown. The averages for the BiliBed phototherapy unit are shown in table F.3. The averages are calculated according to section 3.1.4.

All values in this appendix are in units of μW/cm^2. The UVA probe measured the irradiances in units of mW/cm^2, which is seen in the high uncertainty of the values of table F.1.

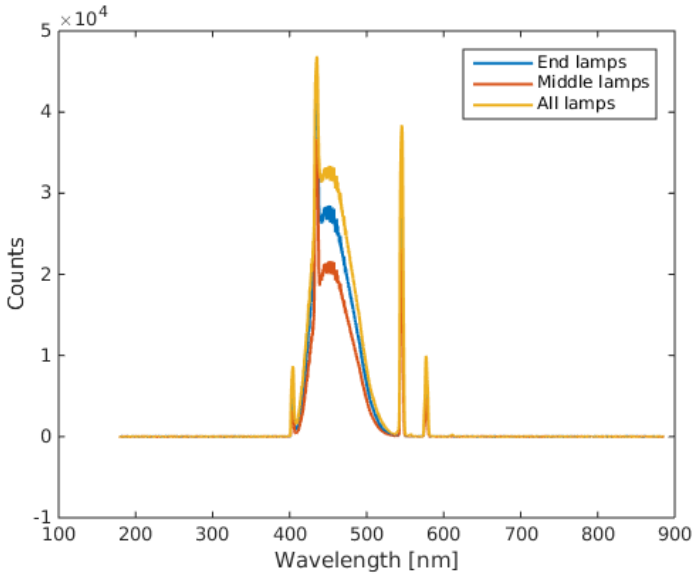

Figure F.3: Spectra of the overhead phototherapy unit when set on three different settings. The settings determine which of the fluorescent lamps are switched on, either all, the ones in the middle or the ones at the end.

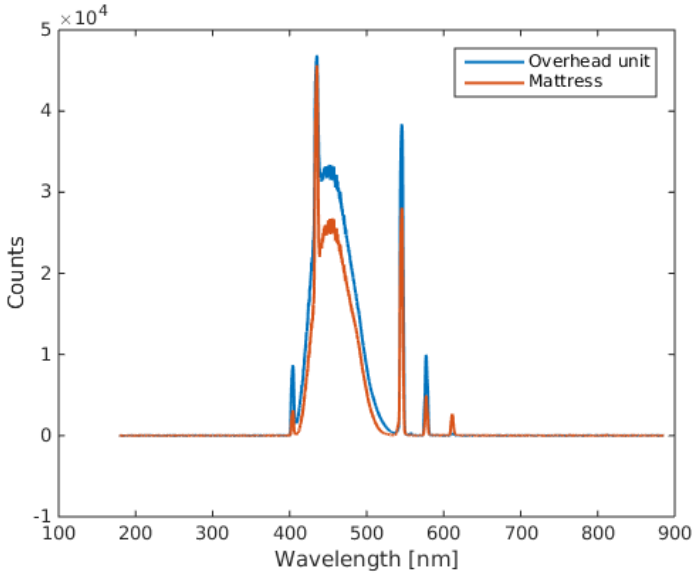

Figure F.4: Spectrum of the overhead phototherapy unit compared with the spectrum of the BiliBed mattress, which irradiates the infant from underneath.

Measurement info			Max	Min
Unit	Description	Distance [cm]	[μW/cm^2]	[μW/cm^2]
Overhead	Blue probe, with curtains	20	1738.7	197.0
Overhead	Blue probe without curtains	20	1661.1	106.8
Overhead	UVA probe with curtains	20	21	1
Overhead	UVA probe without curtains	20	20	1
Overhead	Blue probe, with curtains	25	1565.4	276.8
Overhead	Blue probe without curtains	25	1259.0	155.8
Overhead	UVA probe with curtains	25	15	2
Overhead	UVA probe without curtains	25	15	1
Overhead	Blue probe, with curtains	30	1369.9	365.0
Overhead	Blue probe without curtains	30	1003.1	198.3
Overhead	UVA probe with curtains	30	18	0
Overhead	UVA probe without curtains	30	14	1
Overhead	Blue probe, with curtains	35	1121.9	414.8
Overhead	Blue probe without curtains	35	737.9	225.1
Overhead	UVA probe with curtains	35	9	2
Overhead	UVA probe without curtains	35	10	3
BiliBed	Blue probe, with curtains	–	1603.0	50.0
BiliBed	Blue probe, without curtains	–	1633.5	79.3

Table F.1: Maximum and minimum measured irradiance for the different measurement series of both phototherapy units. The distance is the effective distance between the lamp and the infant undergoing treatment. The blue probe is weighted with bilirubin through the correction factor C_{tot} from equation (3.3)*. The UVA values has not been weighted.*

Measurement info		Total average	Average, area under lamp
Description	Distance [cm]	[µW/cm^2]	[µW/cm^2]
Blue probe, with curtains	20	1079.9	960.5
Blue probe without curtains	20	951.2	864.2
UVA probe with curtains	20	10.9	9.9
UVA probe without curtains	20	11.7	10.1
Blue probe, with curtains	25	1034.3	876.3
Blue probe without curtains	25	777.6	673.8
UVA probe with curtains	25	9.4	8.1
UVA probe without curtains	25	8.7	7.7
Blue probe, with curtains	30	971.9	791.3
Blue probe without curtains	30	685.0	569.6
UVA probe with curtains	30	8.6	7.6
UVA probe without curtains	30	8.2	6.9
Blue probe, with curtains	35	850.4	662.5
Blue probe without curtains	35	545.4	432.4
UVA probe with curtains	35	7.1	5.7
UVA probe without curtains	35	6.0	4.9

Table F.2: All average irradiance measurements from the different measurement series of the overhead lamp. The distance is the corresponding distance between the lamp and the infant undergoing treatment. The blue probe is weighted with bilirubin through the correction factor C_{tot} from equation (3.3)*. The UVA values has not been weighted.*

Measurement info		Total average	Average, area over lamp
Description	Distance [cm]	[µW/cm^2]	[µW/cm^2]
Blue probe, with curtains	–	665.2	1012.8
Blue probe, without curtains	–	732.1	1145.0

Table F.3: Average irradiance measurements from the BiliBed mattress. The only distance measured was at the level of the mattress where the infant lies. The blue probe is weighted with bilirubin through C_{tot} from equation (3.3)*. There was no significant irradiance measured with the UVA probe.*

Appendix G

All atmospheric simulations of conditions in chosen locations

The selected locations are shown in table 3.1. In this appendix, the satellite data used to simulate real conditions throughout 2015 are displayed, followed by all simulations of both clear and cloudy conditions for all three locations.

G.1 Overview of satellite data

Satellite data was taken from [79], and only values for 2015 were used in this thesis. The information used to approximate real conditions were the levels of ozone in the atmosphere, the albedo measured on the surface, and the level of cloud optical depth in the atmosphere. The variations of these variables can be seen in figures G.1 to G.4. The variations in ozone level is illustrated in figure G.1, the variations in albedo is illustrated in figure G.2 and the variations in cloud optical depth is shown in figures G.3 and G.4, first as a function of day of year and then as a probability function. The variations in accuracy of the satellite overpass data in terms of latitude and longitude are shown in figure G.5.

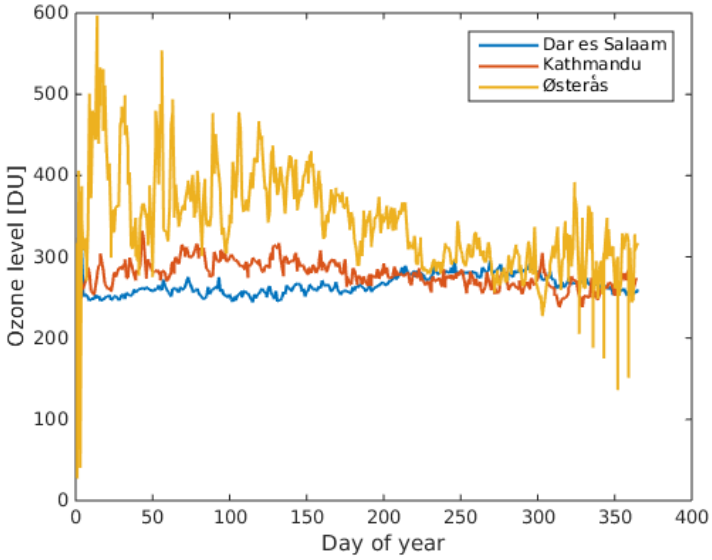

Figure G.1: Illustration of the level of ozone in the atmosphere throughout 2015 for all three locations [79].

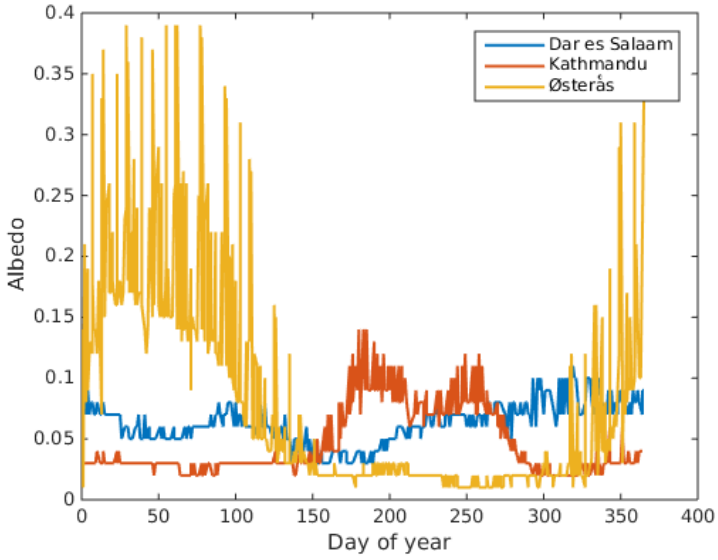

Figure G.2: Illustration of the surface albedo as captured by satellite overpass throughout 2015 for all three locations [79].

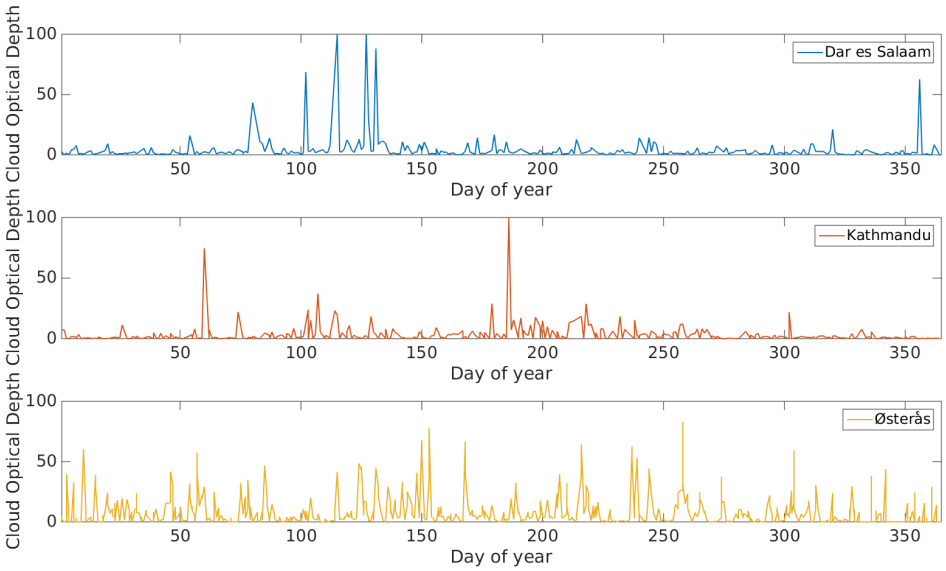

Figure G.3: Illustration of the cloud optical depth in the atmosphere throughout 2015 for all three locations [79].

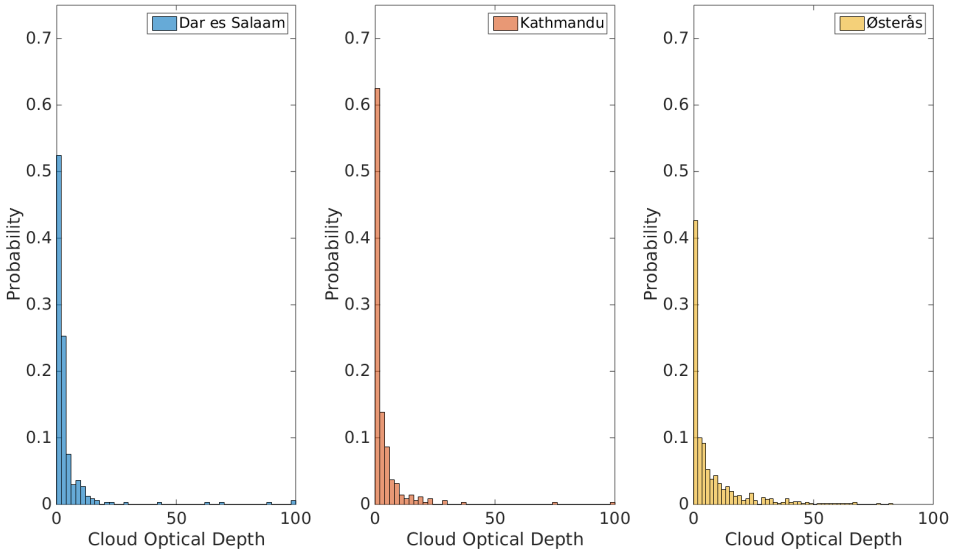

Figure G.4: Probability of getting a certain cloud optical depth for a given day in 2015 for all three locations [79].

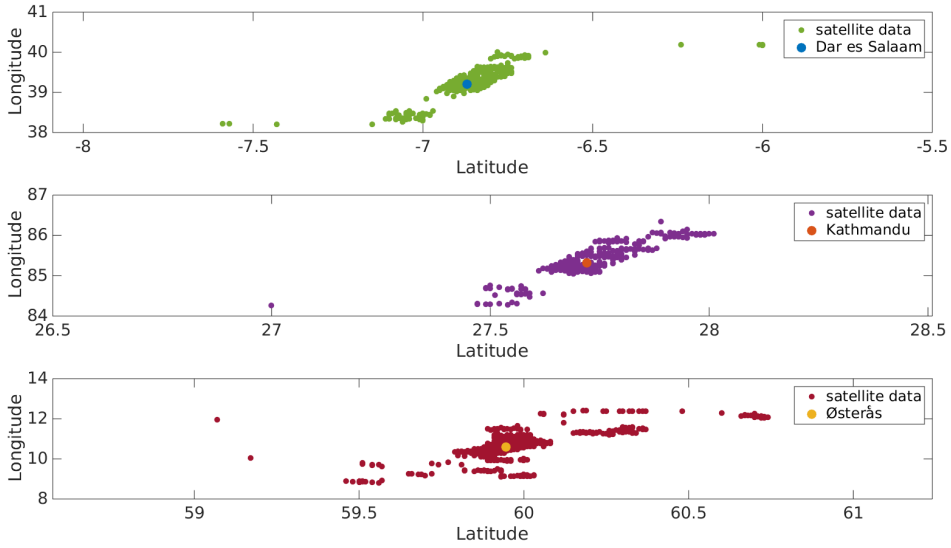

Figure G.5: Depiction of the accuracy of the satellite data with respect to the latitude and longitude of the geographical locations. The fixed position used with the simulations is shown by large bullet points, and the different satellite data are shown with scatter points and marked with the label of satellite data. Notice the negative latitude for Dar es Salaam.

G.2 Results from simulations

All simulation results for the three locations can be found in this section. All three locations were simulated with atmospheric variables from the satellite overpass data, and for clear conditions where the cloud optical depth were set to 0 while ozone layer and albedo remained unchanged compared to the satellite data. The clear conditions were simulated for comparative reasons.

The simulated irradiances can be seen in figures G.6 to G.17. These irradiances have been scaled with weightings of the bilirubin action spectrum or the erythema action spectra. The amount of data points from the satellite overpass data has been specifies as n.

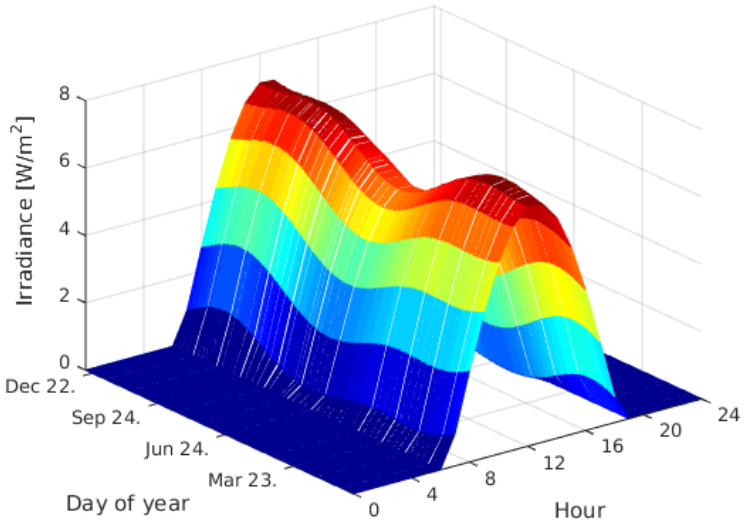

Figure G.6: Incoming bilirubin weighted solar irradiance in Dar es Salaam throughout 2015, without cloud cover. Number of sets of data points is $n = 331$.

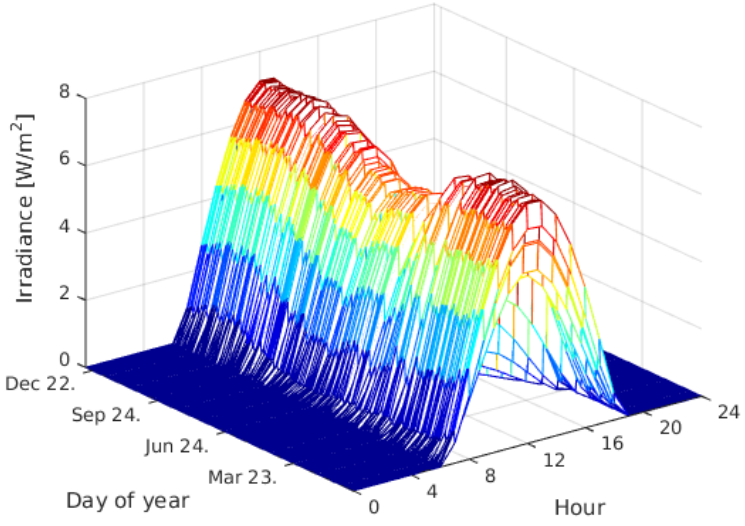

Figure G.7: Incoming bilirubin weighted solar irradiance in Dar es Salaam throughout 2015, including cloudy weather. Number of sets of data points is $n = 331$.

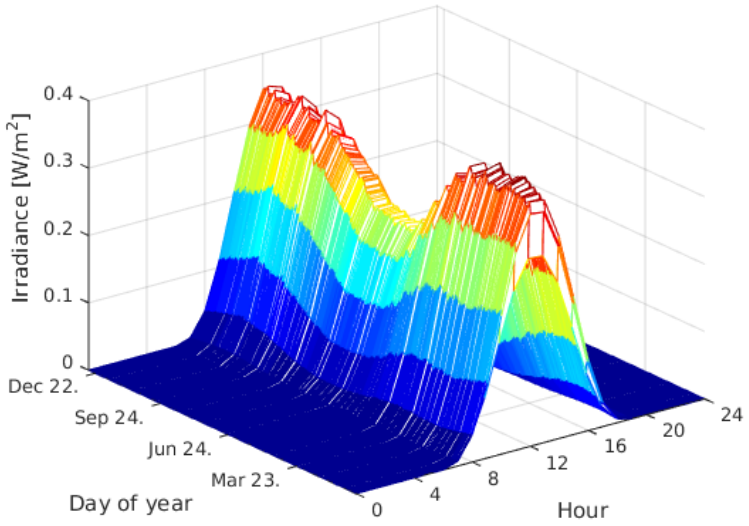

Figure G.8: Incoming erythema weighted solar irradiance in Dar es Salaam throughout 2015, without cloud cover. Number of sets of data points is $n = 331$.

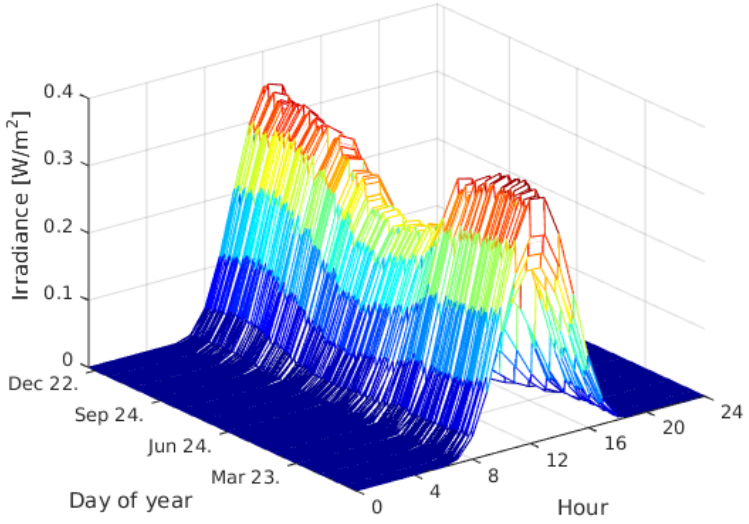

Figure G.9: Incoming erythema weighted solar irradiance in Dar es Salaam throughout 2015, including cloudy weather. Number of sets of data points is $n = 331$.

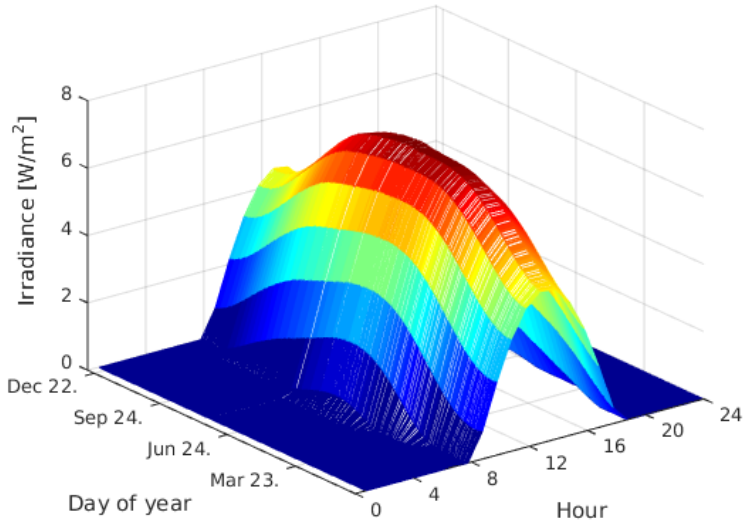

Figure G.10: Incoming bilirubin weighted solar irradiance in Kathmandu throughout 2015, without cloud cover. Number of sets of data points is $n = 347$.

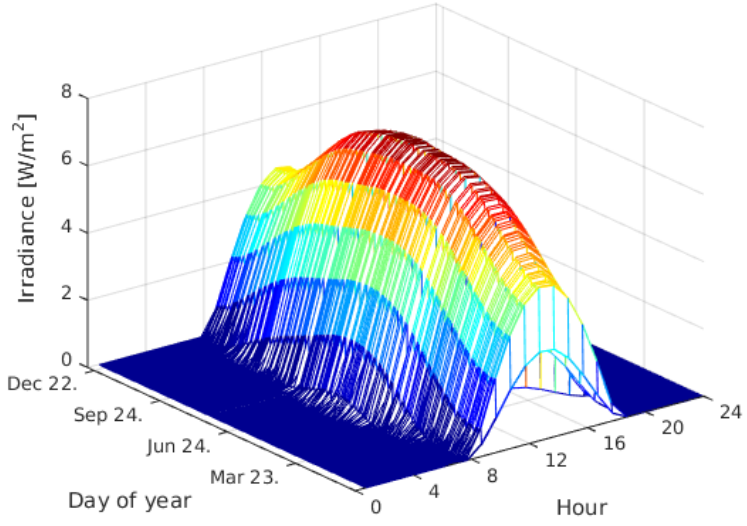

Figure G.11: Incoming bilirubin weighted solar irradiance in Kathmandu throughout 2015, including cloudy weather. Number of sets of data points is $n = 347$.

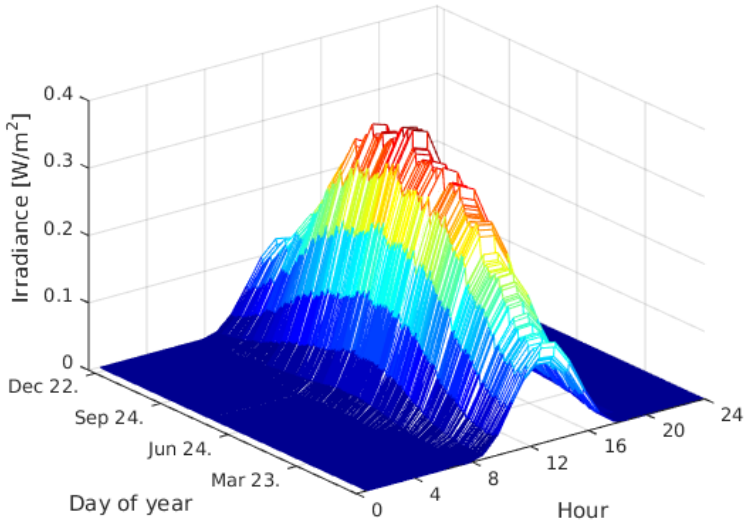

Figure G.12: Incoming erythema weighted solar irradiance in Kathmandu throughout 2015, without cloud cover. Number of sets of data points is $n = 347$.

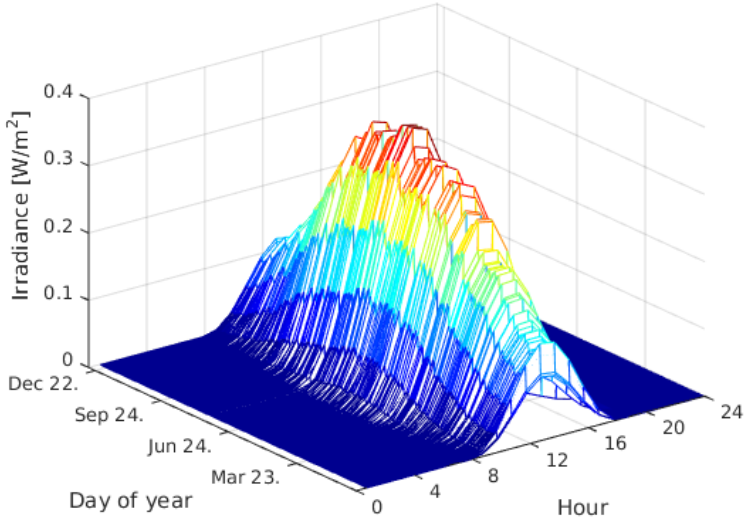

Figure G.13: Incoming erythema weighted solar irradiance in Kathmandu throughout 2015, including cloudy weather. Number of sets of data points is $n = 347$.

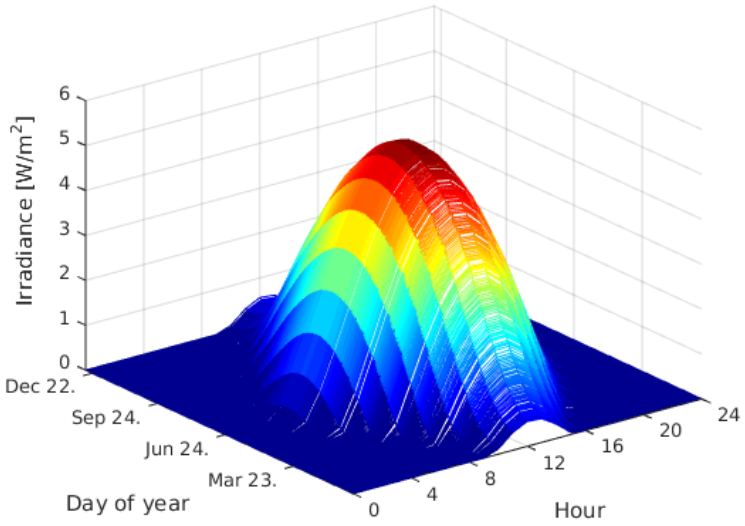

Figure G.14: Incoming bilirubin weighted solar irradiance at Østerås throughout 2015, without cloud cover. Number of sets of data points is $n = 661$.

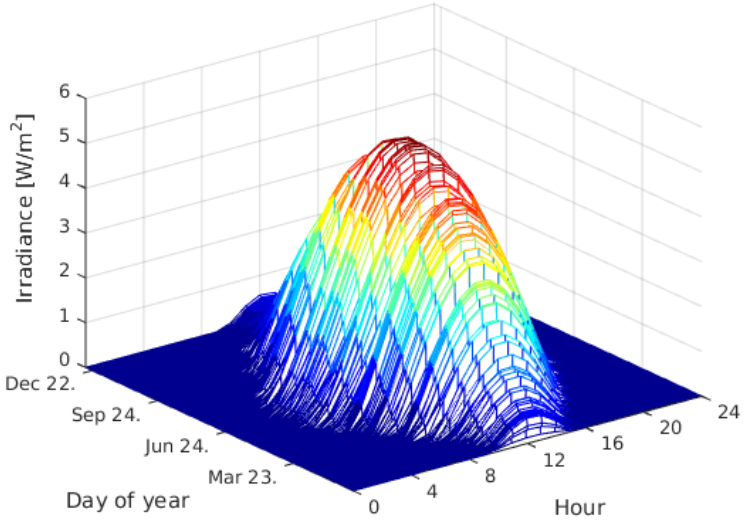

Figure G.15: Incoming bilirubin weighted solar irradiance at Østerås throughout 2015, including cloudy weather. Number of sets of data points is $n = 661$.

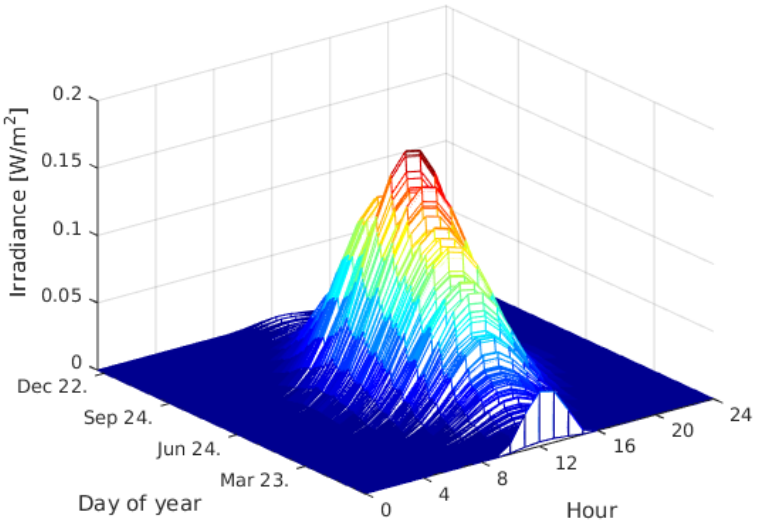

Figure G.16: Incoming erythema weighted solar irradiance at Østerås throughout 2015, without cloud cover. Number of sets of data points is $n = 661$.

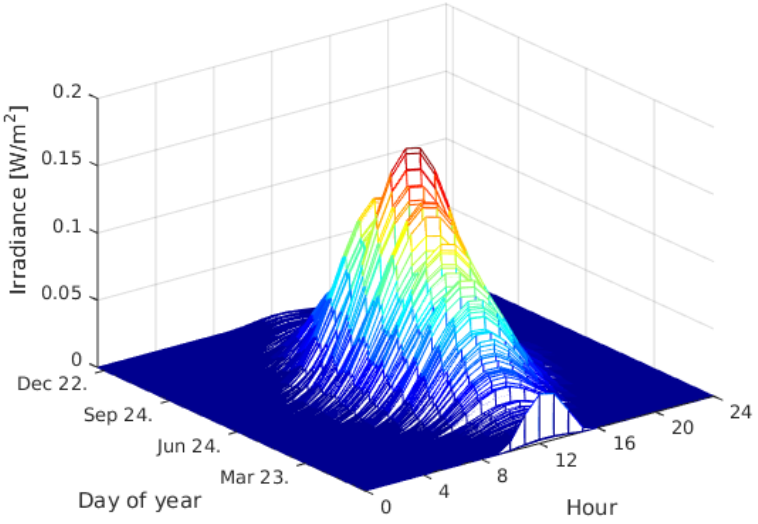

Figure G.17: Incoming erythema weighted solar irradiance at Østerås throughout 2015, including cloudy weather. Number of sets of data points is $n = 661$.

G.3 Overview of cloud modification factors

The CMF changes as the relationship between the incoming irradiation for actual conditions and the clear conditions. In figure G.18, the CMFs for Dar es Salaam throughout 2015 can be seen. The same can be seen for Kathmandu and Østerås in figures G.19 and G.20, respectively. The CMF has only been calculated for incoming irradiances larger than zero.

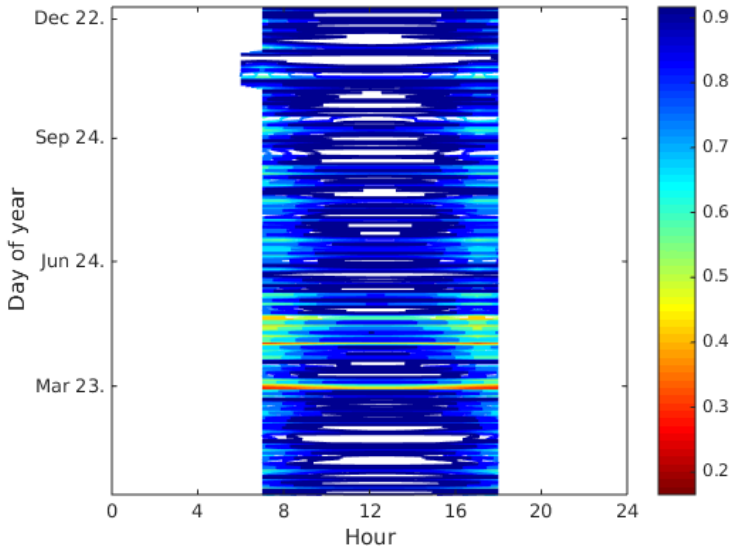

Figure G.18: CMF for Dar es Salaam throughout 2015 as a function of day of year and hour of day.

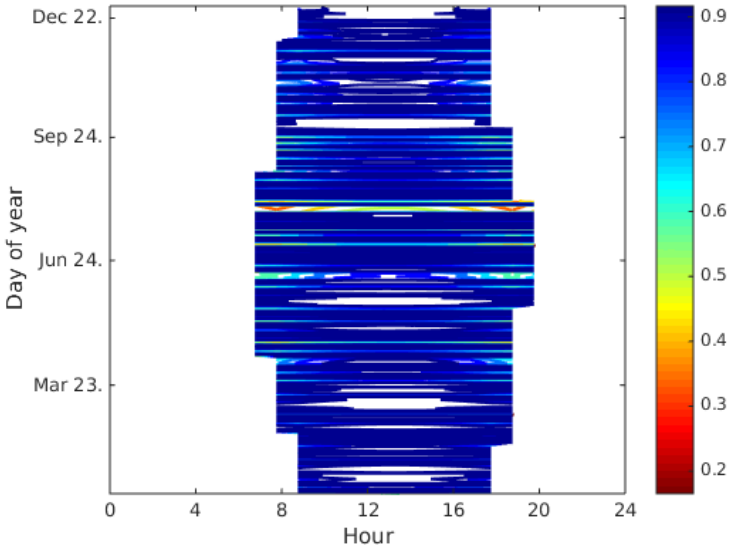

Figure G.19: CMF for Kathmandu throughout 2015 as a function of day of year and hour of day.

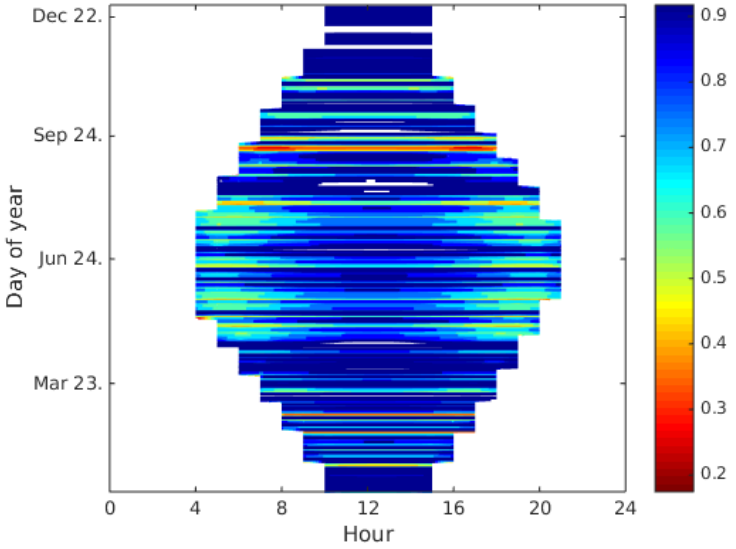

Figure G.20: CMF for Østerås throughout 2015 as a function of day of year and hour of day.

Appendix H

Optical parameters for skin simulations

The optical parameters used in the MCML simulation of infant skin of GM 40 weeks are presented graphically in this appendix. In figure H.1, the absorption coefficient μ_a for the epidermis may be seen as a function of wavelength for different skin types. As all bilirubin in jaundiced skin is distributed in the dermis, this absorption coefficient is the same for healthy skin and the skin of an infant diagnosed with neonatal jaundice. In figure H.2, the absorption coefficient μ_a for the dermis as a function of wavelength can be seen for both normal and jaundiced skin. As all melanin is distributed in the epidermis, the absorption coefficient in the dermis is independent of skin type.

Both the scattering coefficient μ_s and the scattering anisotropy g is independent of both bilirubin content, skin type and skin layer for infant skin, given a GM of 40 weeks. The scattering coefficient is displayed in figure H.3 as a function of wavelength, and the scattering anisotropy is displayed in figure H.4.

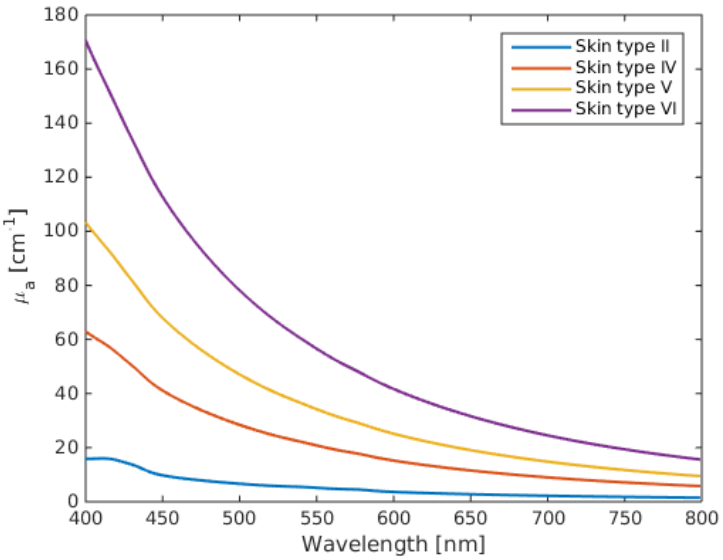

Figure H.1: The absorption coefficients μ_a for the epidermis of infant skin with GM 40 *weeks as a function of wavelength for skin types II, IV, V and VI.*

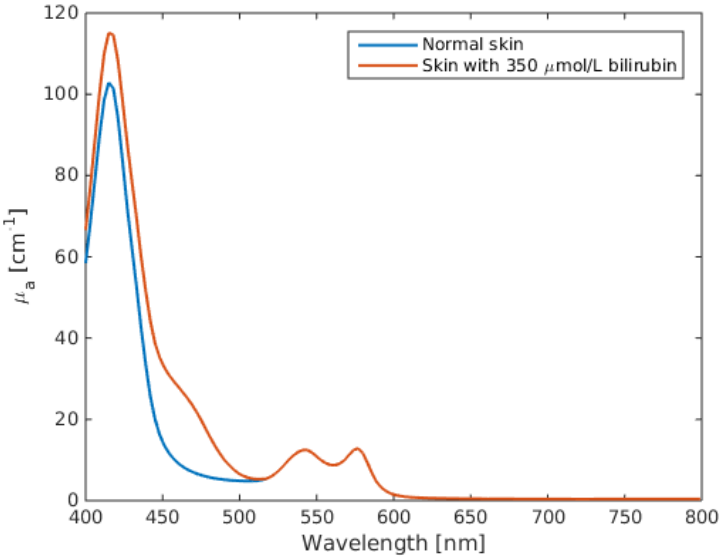

Figure H.2: The absorption coefficients μ_a for the dermis of infant skin with GM 40 *weeks as a function of wavelength, both for normal skin and for jaundiced skin with* $350\,\mu$mol/L *bilirubin.*

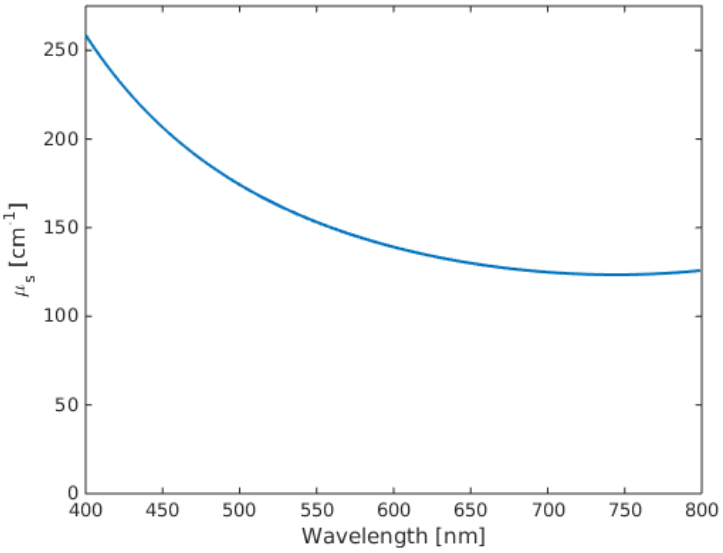

Figure H.3: Scattering coefficient μ_s for infant skin with GM of 40 weeks as a function of wavelength.

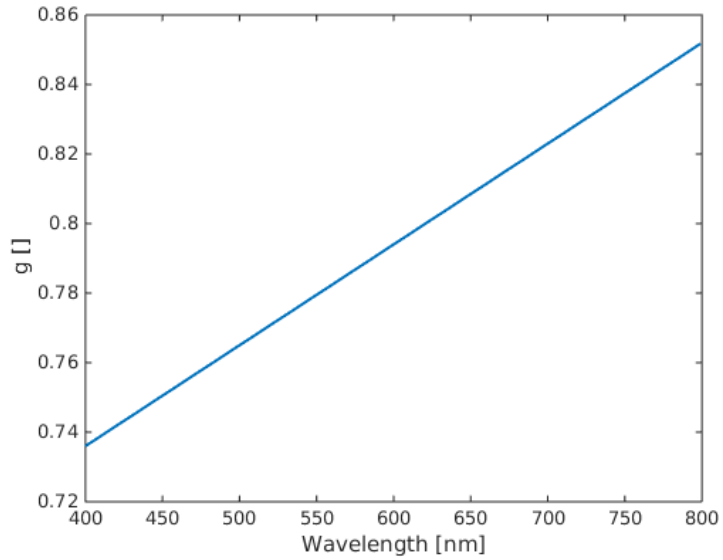

Figure H.4: Scattering anisotropy g for infant skin with GM of 40 weeks as a function of wavelength.

Appendix I

Comparison between spectrum of overhead phototherapy unit and solar spectrum

A way to compare a conventional phototherapy unit with sunlight is to compare their delivered spectra. These spectra can be given either in terms of counts of a spectrometer or in spectral irradiance. In section 3.1.6 the spectrum of the overhead phototherapy unit has been converted to spectral irradiance. This converted spectrum may be directly compared to the solar irradiance given by *libRadtran*. Such comparisons can be seen in figures I.1, I.2, I.3 and I.4. In these figures, the phototherapy spectrum has been plotted together with the spectra found in Dar es Salaam, Kathmandu and Østerås for cloudless conditions at times of both 08 and 12, for the 22^{nd} of March, the 24^{th} of June, the 22^{nd} of September and the 21^{nd} of December, respectively. The figures contain both clean spectra, and spectra weighted with the bilirubin action spectrum.

As can be seen from all figures, the solar spectra varies according to the phototherapy spectrum depending on the time of day, day of year and geographical location. However, the spectra are always directly comparable, with a difference of less than one order of magnitude.

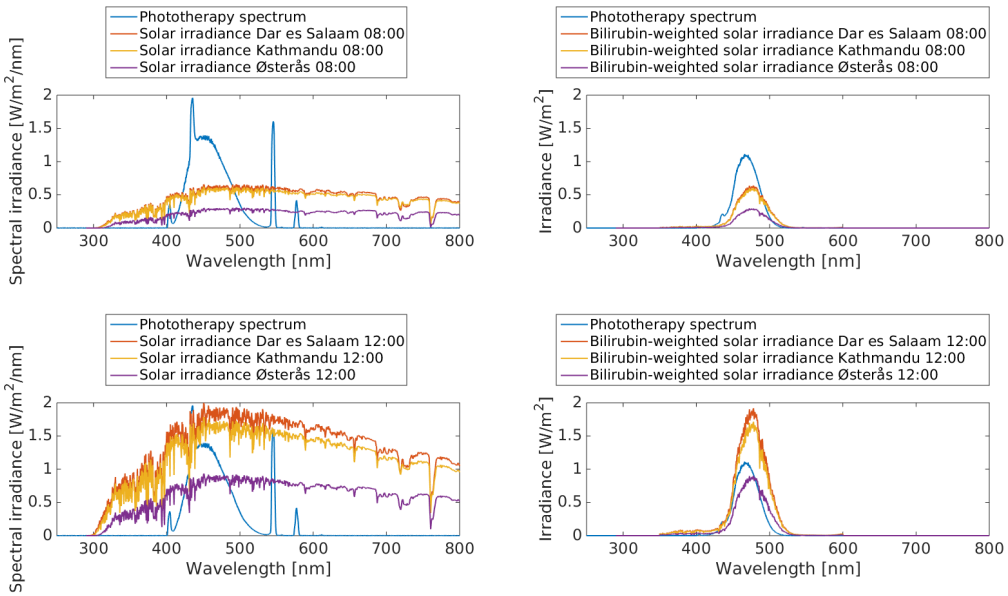

Figure I.1: A comparison of the spectrum of a conventional phototherapy overhead unit in spectral irradiance and the solar spectrum for Dar es Salaam, Kathmandu and Østerås for time of day 08:00 (top) and 12:00 (bottom). The original spectra are to the left, and bilirubin weighted spectra is found to the right. The spectra correspond to day number 80*, which is the* 21^{nd} *of March.*

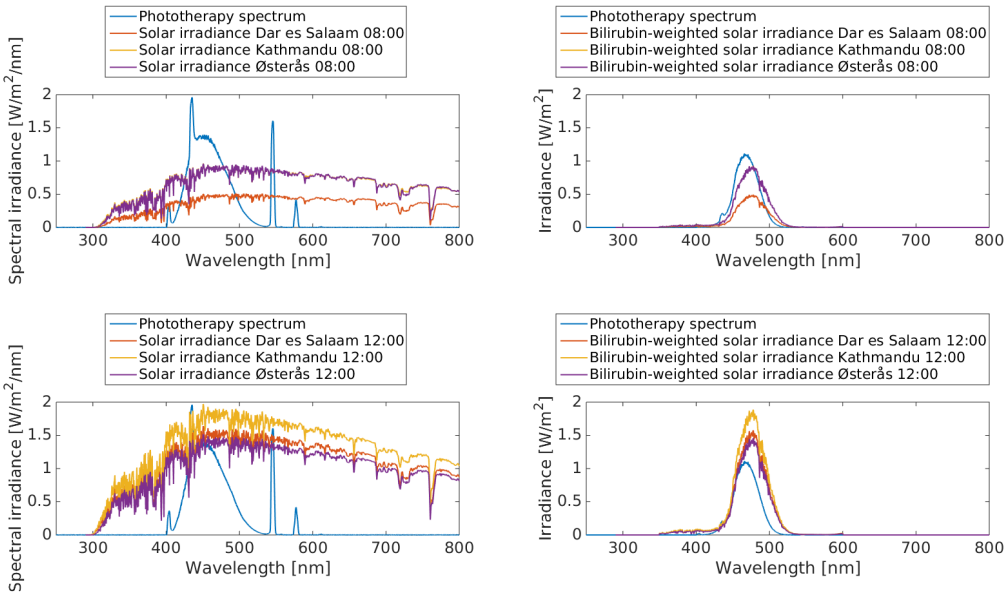

Figure I.2: A comparison of the spectrum of a conventional phototherapy overhead unit in spectral irradiance and the solar spectrum for Dar es Salaam, Kathmandu and Østerås for time of day 08:00 (top) and 12:00 (bottom). The original spectra are to the left, and bilirubin weighted spectra is found to the right. The spectra correspond to day number 175*, which is the* 24^{th} *of June. The results at Østerås equals the results in Kathmandu for 08:00.*

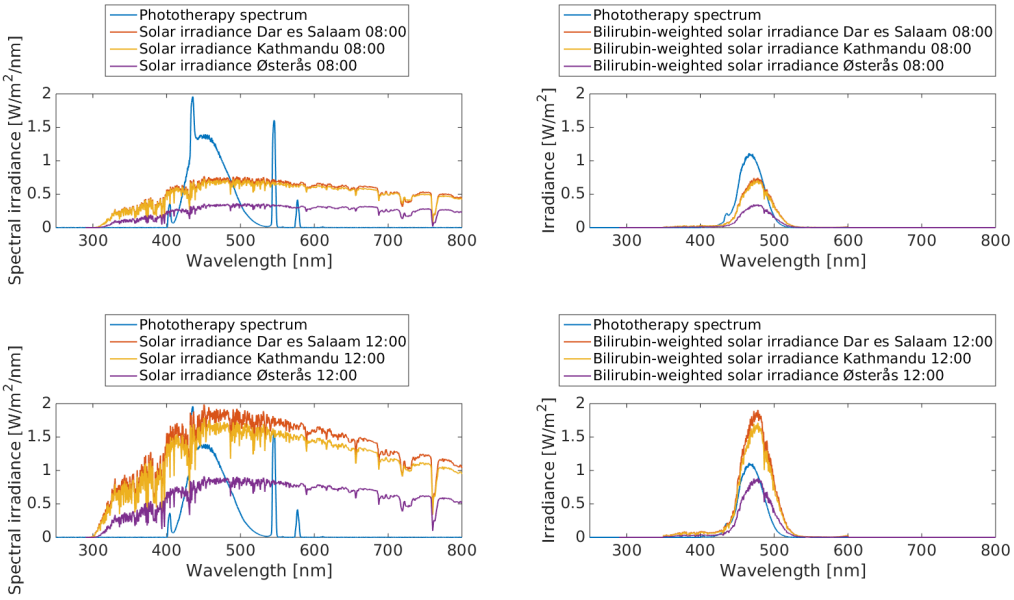

Figure I.3: A comparison of the spectrum of a conventional phototherapy overhead unit in spectral irradiance and the solar spectrum for Dar es Salaam, Kathmandu and Østerås for time of day 08:00 (top) and 12:00 (bottom). The original spectra are to the left, and bilirubin weighted spectra is found to the right. The spectra correspond to day number 265*, which is the* 22nd *of September.*

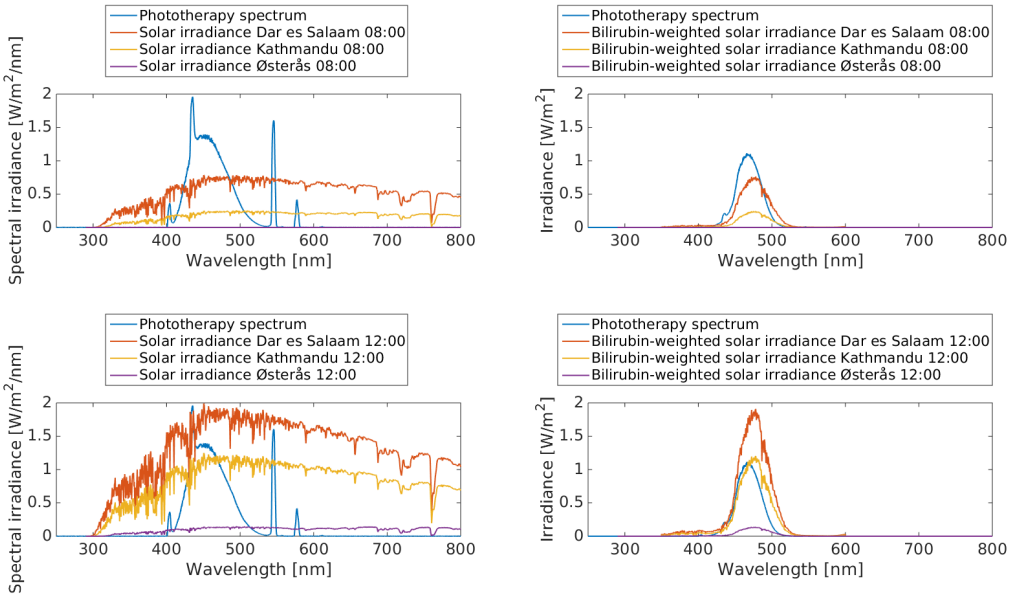

Figure I.4: A comparison of the spectrum of a conventional phototherapy overhead unit in spectral irradiance and the solar spectrum for Dar es Salaam, Kathmandu and Østerås for time of day 08:00 (top) and 12:00 (bottom). The original spectra are to the left, and bilirubin weighted spectra is found to the right. The spectra correspond to day number 80*, which is the* 22nd *of December. At 08:00, the sun has not risen at Østerås.*